Ανασκόπηση της Μεταδιδακτορικής Έρευνας
του
Εμμανουήλ Θ. Μιχαηλίδη

Θέμα: Δορυφορικά και Στρατοσφαιρικά Συστήματα Ευρυζωνικών Επικοινωνιών Επόμενης Γενιάς

Επιστημονική Εξειδίκευση: Τηλεπικοινωνίες

Επιστημονικός Κλάδος: Φυσικές Επιστήμες

Επιστημονικός Τομέας: Φυσικές Επιστήμες και Επιστήμες Μηχανικού

Επιβλέπων Καθηγητής: Αθανάσιος Κανάτας, Καθηγητής Πανεπιστημίου Πειραιώς

Abstract

As the aerospace systems are expected to be an essential part of the Fifth-Generation (5G) communication infrastructure, the post-doctoral research provides a convenient framework and guidelines for the analysis, test, and design of 5G aerospace-based systems. The core of this research deals with advanced techniques and methods that intend to increase the data rate, extend the radio coverage, and improve the link reliability.

Since the 5G vision will bring new unique network and service capabilities towards the evolution of Internet of Things (IoT), the report of this research initially justifies why the aerospace communications is a key technology that will bring the IoT vision closer to reality and underlines the potential IoT applications.

In this report, Multi-User (MU) Multiple-Input Multiple-Output (MIMO) relay-based satellite and stratospheric systems are also studied. To model the satellite and terrestrial channel, the Loo and Rician statistical distributions are utilized, respectively. Numerical results are provided in terms of the bit-error rate and the channel capacity and the linear Zero-Forcing (ZF) and Minimum Mean Square Error (MMSE) signal detection techniques are employed. Moreover, a MU-MIMO aerial relay aided system with orthogonal Space-Time Block Coding (OSTBC) transmission and rate-adaptive modulation is presented and a novel three-dimensional (3-D) geometry-based optimization method for the location of an aerial relay is proposed. Expressions for the outage probability and the spectral efficiency are presented. The results highlight the impact of the relay position, power allocation, fading severity, and number of antennas on the overall system performance.

Moreover, this report presents a triple-hop mixed Radio-Frequency/Free-Space-Optical/Radio-Frequency (RF/FSO/RF) communication system, which intends to support wireless long-range links between two terrestrial stations via multiple stratospheric relays. It is considered that these terrestrial stations communicate with the relays over Single-Input Single-Output (SISO) or MIMO RF links, whereas

the relays communicate with each other over an FSO link. The RF channels experience Rician fading due to the Line-of-Sight (LoS) and Non-Line-of-Sight (NLoS) signal components. Besides, the optical channel is affected by atmospheric attenuation, atmospheric turbulence, and pointing errors. Mathematical expressions for the outage probability are derived, considering the beam wander effect. The results demonstrate the theoretical derivations.

Finally, this report proposes a novel theoretical non-stationary 3-D model for wideband massive MIMO stratospheric channels. This model considers nearfield effects instead of farfield effects, since the dimension of massive MIMO antenna arrays cannot be ignored. To model the non-stationary properties of clusters, a birth-death process is presented corresponding to cluster appearance and disappearance on both the array and time axes. The statistical properties of the proposed model are investigated in terms of the space-time correlation function (STCF) and the Doppler power spectral density (PSD). The numerical results demonstrate the theoretical derivations.

Keywords: Atmospheric turbulence, birth-death process, Free-Space-Optical (FSO) communications, High-altitude platforms (HAPs), Internet of things (IoT), massive Multiple-Input Multiple-Output (MIMO) systems, Multi-User (MU) systems, non-stationarity, relays, satellite networks, Unmanned Aerial Vehicles (UAVs).

TABLE OF CONTENTS

1

Introduction

1.1 Introduction to Aerospace Communications

Nowadays, fourth generation (4G) communication systems have enabled access to advanced services, such as video communications, multimedia, and high-speed internet access. Besides, the fifth generation (5G) vision represents a significant upgrade of mobile broadband communications, but it will also bring new unique network and service capabilities towards the evolution of Internet of Things (IoT) [1], [2]. The 5G systems will incorporate a large variety of emerging services and applications that deviate from the conventional development steps of cellular networking. A key objective in the development of these systems is the seamless integration of wireless terrestrial and aerospace infrastructures over heterogeneous networks [3]-[5].

Terrestrial links are widely used to provide services in areas with complex propagation conditions, while satellite links are usually used to provide high-speed connections, where terrestrial infrastructure is not available. Satellites refer to Spaceborne vehicles in Low Earth Orbit (LEO), Medium Earth Orbit (MEO), Geostationary Earth Orbit (GEO), Highly Elliptical Orbit (HEO), as well as CubeSats [6]. Beyond satellites, the non-terrestrial networks (NTN) refer to networks or segments of networks using airborne vehicles or High-, Medium-, and Low-Altitude Platforms (HAPs/MAPs/LAPs) for transmission operating at altitude typically between 8 and 50 km above the ground [7]-[10]. Two major HAP structures are considered in the literature, the circling aircrafts and the lighter-than-air, quasi-stationary, and solar-powered airships. The aircrafts fly in a roughly circular tight path, are powered by fuel engine propulsion, and can be either unmanned with continuous flight duration in the order of months or manned with average

flight duration of some hours due to the fuel constraints and human factors. Besides, the airships use very large semi-rigid or non-rigid helium-filled containers and electric motors and propellers for station-keeping and are capable of staying in the air for around five years. MAPs and LAPs fly at lower altitudes, in the troposphere, and intend to accomplish various missions, such as photographic reconnaissance, low-altitude urban traffic surveillance, emergency communications in post-disaster situations or unexpected events, earth observation, and agricultural purposes. Among them, the Unmanned Aerial Vehicles (UAVs) are a type of small fueled unmanned aircrafts employed for short time periods (up to 40 hours) at modest altitudes and allow for a rapid relay-based deployment of a multi-hop communication backbone in challenging applications, such as public safety, search and rescue missions, crowd surveillance, and disaster area monitoring. The UAVs include Remotely Piloted Vehicles (RPVs), drones, robot planes, and pilotless aircrafts and can vary in size from small toys that fit in the palm of a human hand to large military aircraft, e.g., the General Atomics MQ-9 Reaper (commonly termed Predator). Recently, a great interest has risen by academia and industry towards the use of aerial platforms as base stations, movable relays or autonomous communicating nodes [11]. The 3rd Generation Partnership Project (3GPP) suggested the use of aerial vehicles for the Long-Term Evolution (LTE) [12], whereas the notion of nomadic relay was proposed by the IEEE 802.16s Relay Task Group [13].

This chapter provides an overview of the aerospace communication infrastructure and presents advanced wireless technologies that intend to enrich the capabilities of aerospace communications. The rest of the chapter is organized as follows. Section 1.2 describes the characteristics of aerospace communications and emphasizes their advantages and challenges. Section 1.3 introduces the multiple-input multiple-output (MIMO) technology and highlights potential wireless technologies for 5G communications. Section 1.4 summarizes the contributions of this report of the post-doctoral research. Finally, Section 1.5 provides an outline of the report.

1.2 Characteristics of Aerospace Communications

The satellite communications have the potential to maintain the wireless link connectivity in scenarios with terrestrial network constraints, i.e., remote nodes, highly mobile nodes, and highly dispersed nodes over a wide geographical area. Although the satellite networks have a huge initial cost, they are capable of bringing communications to sparsely populated or underdeveloped areas, and still maintain exclusive status in traditional maritime and aeronautical markets from the wide area perspective due to their unique coverage features. The spaceborne networks can support services for navigation, Earth observation, emergency rescue, and communication/relaying, strongly enhance the terrestrial backhaul networks, and provide extensive as well as uninterrupted radio coverage to stationary, portable, and mobile receivers at frequencies ranging from 100 MHz to 100 GHz, as well as at optical frequencies. GEO satellites are available from a large number of suppliers and can enable multicast/broadcast and trucking of video and other data across a large coverage area or a central site, with further terrestrial distribution to local cell sites. LEO satellite constellations require less on-the-ground power and smaller antennas due to the significantly lower orbit altitude (normally lower than 2000 km) and smaller propagation losses. Since most ground terminals are small-sized and energy-constrained, the aforementioned benefits of LEO satellites are substantial. The capabilities of satellite networks in terms of the latency are in part due to the use of Adaptive Coding and Modulation (ACM) techniques as foreseen in the Digital Video Broadcasting – Satellite – Second Generation (DVB-S2) standard, which retains outbound throughput even during heavy weather conditions. To further improve the performance of satellite systems, algorithms based on cognitive radio principles can be applied that enable dynamic spectrum access and agile waveform adaptation (from carrier aggregation to unlicensed spectrum sharing). The CubeSats will also play an important role in providing extended, low-cost radio coverage. Contrary to LEO satellites whose construction and deployment cost can reach several tens of millions of USD, the cost of CubeSats can be reduced to less than 1M USD. In addition, the form factor

of CubeSats, typically 10x10x10 cm3 allows for the integration of accurate Attitude Determination and Control Systems (ADCS) and efficient, deployable solar panels, which in turn increases the range of potential applications.

HAPs, MAPs, and LAPs preserve some of the best characteristics of terrestrial and satellite communication systems, while avoiding many of their drawbacks. The airborne networks are capable of providing ubiquitous and cost-effective LoS wireless access over large coverage areas at high elevation angles, while they attain network flexibility and adaptability due to their rapid deployment and movement on demand [7], [10]. In comparison to terrestrial cellular technologies, these platforms require considerably less communications infrastructure and they can serve potentially large coverage areas. When compared to satellite communication systems, they provide lower propagation delays (a critical issue for voice communications over satellite) and less free-space loss, as well as easy maintenance and upgrading of the payload during the lifetime of the platform. In addition, the cost for the development of satellite systems is much greater and it may be economically more efficient to cover a large area with many aerial platforms rather than with many terrestrial base stations or with a satellite system. The solar-powered aerial platforms are also non-pollutant and environmentally friendly. Since the links of terrestrial systems are often blocked, the aerial platforms, especially HAPs and drones, have great potential to attain a higher chance of LoS communication with the ground users and thus enhance the coverage and connectivity. The UAVs can also easily move, have a flexible deployment, and can provide rapid, on-demand communications. Industries may use drones to undertake daily land surveys, feed this data into software to ensure that the operations are on schedule, and send alerts, as soon as an unexpected event occurs. It is expected that future 5G and IoT systems will include UAVs as autonomous communicating nodes for providing low latency and highly reliable connections between sensors and data collection points in cities, across suburban areas, and over rural terrains [14]. Drones can carry all range of sensors gathering massive amounts of valuable data [9].

Nevertheless, the airborne networks have still not attained maturity and there may be several challenges and influencing factors in the utilization of both the spaceborne and airborne infrastructures for 5G and IoT applications. Compared to terrestrial wireless networks, aerospace communication networks have many distinctive features, such as high dynamic network topologies and weakly connected communication links. Many standards, protocols, technologies, and design methodologies used in terrestrial wireless networks are not directly applicable to aerospace communication networks. Therefore, new techniques for aerospace communication networks need to be developed. More specifically, the successful deployment and long-term operation of the aerospace systems necessitates the development of wireless standards for low-power aerospace IoT, careful design and implementation of the onboard antennas, radio channel characterization and modeling, resource management, and coordination and inter-operability between different types of wireless systems. Since effective and reliable communications is a prerequisite for critical IoT applications, the choice of appropriate satellites and aerial platforms heavily depends on the size, altitude, and mobility issues, the autonomy level, and the specific application needs. In addition, the aerial platforms may be displaced in any direction at a varying speed due to the winds or pressure variations of the troposphere and the stratosphere. Thus, the use of stabilization systems is of fundamental importance. Regulations related to the operation of satellites and aerial platforms may restrict how they can be used for IoT scenarios. Energy-efficient design of airborne systems is also required to extend flight duration. Finally, the security and the privacy threats introduced due to the vulnerability of the transmission medium are obviously another serious challenge when applying the aerospace communications to IoT. For instance, GEO satellites are relatively static to the ground, and hence it can be easily located and blanket jammed by enemies. To protect against eavesdroppers, the use of strong cryptographic/authentication protocols and physical layer security techniques [15] may be beneficial. Table 1.1 provides a perspective on the available terrestrial and aerospace communication technologies.

Table 1.1

Comparison of Long-Range Terrestrial and Non-Terrestrial Communication
Technologies

	TERRESTRIAL NETWORKS		NON-TERRESTRIAL NETWORKS				
			SPACEBORNE			AIRBORNE	
	CELLULAR	LPWAN	GEO	MEO	LEO	HAP	UAV
Altitude (km)	-	-	35,786	3,000	<3,000	17-22	<15
Mobility	Static	Static	Static to Earth	Medium	Fast	Quasi-stationary	Varying speeds
Round-Trip Time (ms)	Lowest	Lowest	500	<100	<100	Low	Low
Throughput	Medium to High	Low	Low to High	Low to High	Low to High	Low to High	Low to High
Radio Coverage	Urban & Suburban	Urban	Global	Global	Global	Global	Global
Propagation Loss	Least	Least	Highest	High	Medium	Low	Low
Network Complexity	Complex	Complex	Simple	Medium	Complex	Medium	Medium
Cost	Medium	Medium to Low	High	High	High	Medium	Medium

1.3 Next-Generation Aerospace Communications

The growing demand for greater bandwidth, higher data rates, improved quality
of service (QoS) and ubiquitous access have prompted the development of next-
generation wireless communications systems, which can by far surpass the
capabilities of existing systems and attempt to bring broadband applications to
new experience scenarios. In order to reach the challenging objectives of 5G
wireless networks, the researchers have envisioned novel PHY concepts. In recent
years, the MIMO technology has emerged as the most promising technology in
these measures due to its powerful performance-enhancing capabilities [16]. The
MIMO systems can be defined intuitively by considering that multiple antennas are
used at both the transmitting and the receiving end. The core idea behind MIMO is
the use of space-time processing in which time (the natural dimension of digital

communication signals) is complemented with the spatial dimension inherent in the use of multiple spatially distributed antennas. Then, the signals sampled in the spatial domain at both ends are combined is such a way that they either create effective multiple parallel spatial data pipes (therefore increasing the data rate), and/or add diversity to improve the quality, i.e., the bit-error-rate (BER) of the communication link. This can in turn significantly improve spectral efficiency and enduringly preserve the QoS for the range of services offered.

Nevertheless, the performance gain of applying the MIMO technology to aerospace communication systems has only recently begun to be investigated by academia and space agencies. In an effort to remain competitive with terrestrial systems, satellite communication operators and agencies are trying to follow the progress in terrestrial MIMO technology and profit from the significant research achievements in the area of multi-antenna techniques. In particular, a great interest has gained due to the standardization activities on the finalized DVB – Satellite to Handheld (DVB-SH) standard [17], and the prospective DVB – Next Generation Handheld (DVB-NGH) [18] standard. MIMO encompasses a plethora of techniques including broad categories such as single-user (SU), multi-user (MU) and distributed/virtual MIMO. However, there exist many special characteristics in aerospace communications that should be considered in order to apply particular MIMO techniques. Compared to terrestrial systems, these particular characteristics are service coverage, link geometry, propagation delay, channel impairments, interference scenarios and physical layer interface. Additionally, we can distinguish between different satellite systems variants depending on the orbit, the user mobility (fixed vs. mobile terminals), the operating frequency bands (UHF, L, S, C, X, Ku, Ka, V bands), group size of intended users (broadcast, multicast, unicast), multiplexing scheme (single carrier time division multiplexing (TDM) vs. multicarrier orthogonal frequency division multiplexing (OFDM)), and type of application (delay tolerant vs. delay intolerant).

To effectively enhance the link reliability, extend the network range, and increase the data throughput, both cooperative diversity and MIMO techniques

should be combined for air-to-ground systems [19], [20]. The former preserves the end-to-end (E2E) communication between ground users located in geographically remote areas via an intermediate relay, while the latter provides spatial multiplexing and diversity gain. Various types of relays are used in wireless networks and the two main classes are amplify-and-forward (AF) and decode-and-forward (DF) based on the processing of relays on the signal. In AF relaying, the relay receives the source's signal and performs amplification in the analog domain, as well as phase steering before forwarding the signal to the destination. In DF relaying, the relay receives the source's signal, decodes it, and reencodes it prior to transmission toward the destination. Depending on the ability of a relay to perform or not concurrent reception and transmission, the relays are characterized as full-duplex (FD) or half-duplex (HD).

With the rapid growth of the number of connected devices, 5G communication systems will be deployed in dense-user environments. Hence, shifting from SU to MU networks, typical paradigms of which are the IEEE 802.16j [21] and IEEE 802.11ax [22] networks, is indispensable [23]. More recently, scenarios of relaying in multi-source (MS) multi-destination (MD) networks have been investigated [24]. In these schemes, multiple source/destination (SD) pairs simultaneously communicate with the help of relays, in order to substantially improve the achievable data rate in shared-spectrum multiple access systems. A representative example of this configuration is the interference relay channel (IRC) [25], where a relay assists two independent SD pairs. One of the challenges in MU-MIMO systems is the complexity of the scheduling procedure associated with the selection of a group of users that will be served simultaneously. In conventional wireless MU networks, highly reliable data transmission is not guaranteed between the access point and the mobile users that are located in geographically remote areas. To overcome this problem, a relay can be introduced to ensure effective communication between the two ends.

Data rates in the multigigabit regime can be achieved using Free-Space-Optical (FSO) inter-satellite, inter-platform, satellite-to-ground, and platform-to-ground

connections [26]. An integrated satellite-HAP-terrestrial system would also contribute to the success of IoT applications, in scenarios where the direct links from the satellite to the ground are poor due to weather conditions. Then, a satellite may communicate with multiple HAPs acting as relays using FSO links and each HAP may connect nodes on the ground using RF links. In FSO systems, the data is transmitted at high data rates in the multigigabit regime using collimated highly directed laser beams with compact equipment and low power consumption. The FSO technology ensures privacy with low probability of interception, immunity to electromagnetic interference, and exemption from spectrum regulatory restrictions. The stratosphere stands for a propagation medium well suited for FSO connections. Hopefully, the inter-HAP crosslink is above attenuating clouds, fog or significant aerosols. Hence, inter-HAP distances of up to 900 km are possible with 100% availability [27]. Nevertheless, stratospheric FSO links may experience substantial fluctuations in both the intensity and the phase of the received signal due to variations of the Index of Refraction Turbulence (IRT) along the propagation path resulting by the inhomogeneities in temperature and pressure fluctuations, especially for link distances of 1 km and above [28]. The impact of turbulence in FSO systems can be significantly reduced by using multiple lasers at the transmitter and multiple photo-detectors at the receiver and forming MIMO-FSO systems [29]. Moreover, beam pointing error effects are highly pronounced on the performance of a stratospheric network, which involves large distances and possible displacement of the platforms due to the winds or pressure variations of the stratosphere [30]. In addition, both mechanical vibrations and electronic noise may cause the received spots from the laser beams to wander on the detector planes. Hence, acquisition, pointing, and tracking errors should also be mitigated to achieve high directivity of the transmitted beam.

To satisfy the increasing demand for higher data rates, the massive MIMO technology has been also proposed as a key enabler for the 5G wireless communication systems. Massive MIMO is a large-scale MU-MIMO, where hundreds of antennas are placed at a base station, simultaneously serving many

tens of terminals in the same time-frequency resource [31]. The very large number of antennas offers many benefits that include the great spatial focusing of energy into very small regions of space allowing for selectivity in transmitting and receiving data streams to/from the users, which in turn leads to greater throughput, increased energy efficiency, and effective power control.

1.4 Research Contribution

It is well known that before the introduction of a new technology into a communications system, a large number of theoretical and experimental investigations have to be made. This report investigates the application of the aforementioned advanced wireless communication techniques to aerospace systems for 5G and IoT applications. More specifically, this report studies MU, relay-based, and massive MIMO techniques. Part of this report of the post-doctoral research resulted in publications in International Journals and International Conference Proceedings (including two Best Paper Awards) as follows:

International Journals

[1] **E. T. Michailidis**, N. Nomikos, P. S. Bithas, D. Vouyioukas, and A. G. Kanatas, "Optimal 3-D Aerial Relay Placement for Multi-User MIMO Communications," *IEEE Transactions on Aerospace and Electronic Systems*, accepted for publication.

International Conference Proceedings

[1] **E. T. Michailidis**, N. Nomikos, P. Bithas, D. Vouyioukas, and Athanasios G. Kanatas, "Outage Probability of Triple-Hop Mixed RF/FSO/RF Stratospheric Communication Systems," in *Proc. 10th International Conference on Advances in Satellite and Space Communications (SPACOMM) 2018*, Athens, Greece, 22-26 Apr. 2018. **Best Paper Award**

[2] **E. T. Michailidis**, N. Nomikos, P. Bithas, D. Vouyioukas, and Athanasios G. Kanatas, "Optimal Relay Location and Opportunistic User-Scheduling for Stratospheric Communications," in *Proc. 10th International Conference on Advances in Satellite and Space Communications (SPACOMM) 2018*, Athens, Greece, 22-26 Apr. 2018. **Best Paper Award**

[3]   **E. T. Michailidis**, S. M. Potirakis, and Athanasios G. Kanatas, "Realizing Challenging Internet of Things Applications via Aerospace Infrastructures," in *Proc. 10th International Conference on Advances in Satellite and Space Communications (SPACOMM) 2018*, Athens, Greece, 22-26 Apr. 2018.

1.5. Report Outline

The remainder of this report is organized as follows. Chapter 2 focus on the aerospace-based IoT, describes the benefits of the aerospace infrastructure, and underlines potential applications. Chapter 3 investigates the performance of MU-MIMO relay-based satellite and aerial platform aided communication systems. In Chapter 4, a mixed RF/FSO/RF multi-relay airborne communication system is studied, whereas Chapter 5 proposes a geometry-based model for massive MIMO stratospheric channels. Finally, conclusions are drawn in Section 6.

REFERENCES

[1]   M. R. Palattella et al., "Internet of Things in the 5G Era: Enablers, Architecture, and Business Models," *IEEE J. on Sel. Areas in Commun.*, vol. 34, no. 3, pp. 510-527, Mar. 2016.

[2]   A. Akpakwu, B. J. Silva, G. P. Hancke, and A. M. Abu-Mahfouz, "A Survey on 5G Networks for the Internet of Things: Communication Technologies and Challenges," *IEEE Access*, Dec. 2017.

[3]   B. Evans, M. Werner, E. Lutz, M. Bousquet, G. E. Corazza, G. Maral, and R. Rumeau, "Integration of satellite and terrestrial systems in future multimedia communications," *IEEE Wireless Commun.*, vol. 12, no. 5, pp. 72-80, Oct. 2005.

[4]   B. Paillassa, B. Escrig, R. Dhaou, M.-L. Boucheret, and C. Bes, "Improving satellite services with cooperative communications," *Int. J. Satellite Commun. Netw.*, vol. 29, no. 6, pp. 479–500, Nov./Dec. 2011.

[5]   B. G. Evans, "The role of satellites in 5G," in *Proc. 7th Advanced Satellite Multimedia Systems Conference and the 13th Signal Processing for Space Communications Workshop (ASMS/SPSC)*, Livorno, Italy, pp. 197-202, 2014.

[6]   V. Almonacid and L. Franck, "Extending the coverage of the internet of things with low-cost nanosatellite networks", *Acta Astronautica*, Vol. 138, pp. 95-101, 2017.

[7]   A. Mohammed, A. Mehmood, F. Pavlidou, and M.Mohorcic, "The role of high-altitude platforms (HAPs) in the global wireless connectivity," *Proc. IEEE*, vol. 99, no. 11, pp. 1939-1953, Nov. 2011.

[8]   J. M. Sullivan, "Evolution or revolution? the rise of UAVs," *IEEE Technology and Society Magazine*, vol. 25, no. 3, pp. 43-49, Fall 2006.

[9]   S. A. R. Naqvi, S. A. Hassan, H. Pervaiz, and Q. Ni, "Drone-Aided Communication as a Key Enabler for 5G and Resilient Public Safety Networks," *IEEE Commun. Magazine*, vol. 56, no. 1, pp. 36-42, Jan. 2018.

[10] A. Aragón-Zavala, J. L. Cuevas-Ruíz, and J. A. Delgado-Penín, *High Altitude Platforms for Wireless Communications*, 1st ed. New York: Wiley, Dec. 2008.

[11] Y. Zeng, R. Zhang, and T. J. Lim, "Wireless communications with unmanned aerial vehicles: opportunities and challenges," *IEEE Commun. Mag.*, vol. 54, no. 5, pp. 36-42, May 2016.

[12] "3GPP: study on enhanced support for aerial vehicles," [Online] Available: https://lnkd.in/gR5fpdf.

[13] W. Choi, T. S. Shon, H. H. Choi and Y. Lee, "Designing a Novel Unlicensed Nomadic Access Relay Station in IEEE 802.16-Based Wireless Access Networks," in *Proc. IEEE Vehicular Technology Conference (VTC)*, pp. 2961-2965, Apr. 2007.

[14] H. Menouar, I. Guvenc, K. Akkaya, A. S. Uluagac, A. Kadri, and A. Tuncer, "UAV-Enabled Intelligent Transportation Systems for the Smart City: Applications and Challenges," *IEEE Commun. Magazine*, vol. 55, no. 3, pp. 22-28, Mar. 2017.

[15] G. Zheng, P.-D. Arapoglou, and B. Ottersten, "Physical Layer Security in Multibeam Satellite Systems," *IEEE Transactions on Wireless Communications*, vol. 11, no. 2, pp. 852-863, February 2012.

[16] E. Biglieri, R. Calderbank, A. Constantinides, A. Goldsmith, A. Paulraj, and H. Vincent Poor, *MIMO Wireless Communications*, Cambridge, UK: Cambridge University Press, 2007.

[17] A. Bolea Alamanac, P. Burzigotti, R. De Gaudenzi, G. Liva, H. Nghia Pham, and S. Scalise, "In-Depth Analysis of the Satellite Component of DVB-SH: Scenarios, System Dimensioning, Simulations and Field Trial Results," *International Journal of Satellite Communications and Networking*, 27, 4-5, Jul.-Oct.2009, pp. 215-240.

[18] M. Sanghul, K. Woo-Suk D. Vargas, D. Gozalvez Serrano, M. D. Nisar, and V. Pauli, "Enhanced spatial multi plexing for rate-2 MIMO of DVB-NGH system," in *Proc. 19th International Conference on Telecommunications (ICT) 2012*, Jounieh, Lebanon, 23-25 April 2012, pp. 1-5.

[19] E. T. Michailidis, P. Theofilakos, and A. G. Kanatas, "Three-Dimensional Modeling and Simulation of MIMO Mobile-to-Mobile via Stratospheric Relay Fading Channels," *IEEE Transactions on Vehicular Technology*, vol. 62, no. 5, pp. 2014-2030, Jun. 2013.

[20] L. Sboui, H. Ghazzai, Z. Rezki and M. S. Alouini, "Achievable Rates of UAV-Relayed Cooperative Cognitive Radio MIMO Systems," *IEEE Access*, vol. 5, pp. 5190-5204, 2017.

[21] V. Genc, S. Murphy, Y. Yu and J. Murphy, "IEEE 802.16J relay-based wireless access networks: an overview," *IEEE Wireless Communications*, vol. 15, no. 5, pp. 56-63, Oct. 2008.

[22] M. S. Afaqui, E. Garcia-Villegas and E. Lopez-Aguilera, "IEEE 802.11ax: Challenges and Requirements for Future High Efficiency WiFi," *IEEE Wireless Communications*, vol. 24, no. 3, pp. 130-137, Jun. 2017.

[23] S. Gong, C. Xing, N. Yang, Y. C. Wu and Z. Fei, "Energy Efficient Transmission in Multi-User MIMO Relay Channels With Perfect and Imperfect Channel State Information," *IEEE Transactions on Wireless Communications*, vol. 16, no. 6, pp. 3885-3898, Jun. 2017.

[24] H. Xiao, Z. Zhang and A. T. Chronopoulos, "Performance Analysis of Multi-Source Multi-Destination Cooperative Vehicular Networks With the Hybrid Decode-Amplify-Forward Cooperative Relaying Protocol," *IEEE Transactions on Intelligent Transportation Systems*. (early access)

[25] Y. Tian and A. Yener, "The Gaussian Interference Relay Channel: Improved Achievable Rates and Sum Rate Upperbounds Using a Potent Relay," *IEEE Transactions on Information Theory*, vol. 57, no. 5, pp. 2865-2879, May 2011.

[26] H. Kaushal and G. Kaddoum, "Optical Communication in Space: Challenges and Mitigation Techniques," *IEEE Comm. Surv. & Tutorials*, vol. 19, no. 1, pp. 57-96, Firstquarter 2017.

[27] D. Giggenbach, R. Purvinskis, M. Werner, and M. Holzbock, "Stratospheric Optical Inter-Platform Links for High Altitude Platforms," in *Proc. 20th AIAA ICSSC*, Montreal, pp. 1-11, May 2002.

[28] L. Andrews, R. L. Philips, and C. Y. Hopen, *Laser Beam Scintillation With Applications*. SPIE Press, 2001.

[29] E. Bayaki, R. Schober and R. K. Mallik, "Performance analysis of MIMO free-space optical systems in gamma-gamma fading," *IEEE Transactions on Communications*, vol. 57, no. 11, pp. 3415-3424, Nov. 2009.

[30] M. Sharma, D. Chadha, and V. Chandra, "High-altitude platform for free-space optical communication: Performance evaluation and reliability analysis," *J. Opt. Commun. Netw*., vol. 8, no. 8, pp. 600-609, Aug. 2016.

[31] L. Lu, G. Y. Li, A. L. Swindlehurst, A. Ashikhmin and R. Zhang, "An Overview of Massive MIMO: Benefits and Challenges," *IEEE Journal of Selected Topics in Signal Processing*, vol. 8, no. 5, pp. 742-758, Oct. 2014.

2

Challenging Internet of Things Applications and Aerospace Communications

2.1   Introduction

The IoT is an information network that encompasses a large family of smart and critical applications and transparently deploys a massive number of small, low-cost and low-power interconnected physical objects, generally referred to as Machine-Type Devices (MTDs), which interact and cooperate without human intervention, in order to reach common goals. More specifically, the IoT comprises sensors and actuators interacting with data processing, wired and short- and long-range wireless communication technologies, ground-based processing, and humans. The applications of IoT cover a broad spectrum of use cases and each one has its own set of challenges. One driving application scenario is to form a network of geographically distributed factories with flexible adaptation of production capabilities and sharing of resources and assets to improve order fulfillment.

Nevertheless, some special IoT applications would require coverage in rugged and remote locations, e.g., desert, valley, ocean, and forest, beyond the radio coverage of conventional cellular networks. In such situations, there exist commercial and engineering difficulties of exclusively constructing and exploit terrestrial networks. Therefore, an alternative reliable wide-area communications technology is needed for this use case [1] and the NTNs constitute the only approach to achieve global IoT service covering, as a supplement and extension to the terrestrial IoT networks. The applicability of these networks extends across a diverse range of industries, e.g., energy production, power distribution, water management, as well as applications for smart transportation, environment,

health, and agriculture. From a communications engineering standpoint, the heterogeneity of the aforementioned technologies translates into highly different service requirements in terms of data traffic, end-to-end communication delay, reliability, etc. Cloud and fog computing and networking can facilitate the seamless integration of different heterogeneous networks, whereas Software-Defined Radios (SDR) and Software-Defined Networking (SDN) could bring flexibility and support the cost-efficient deployment and runtime of customized networks [2].

Motivated by these observations, this chapter aims at shedding light on the aerospace-based IoT and describe its special characteristics and the benefits provided by the aerospace infrastructures. Emphasis is given on the integration of the aerospace infrastructure into the industrial domain. In particular, this chapter focuses on the indispensability of the wireless technologies within factory halls and beyond and provides an overview of existing aerospace communication technologies, while addresses the unique challenges that arise when implementing critical IoT applications.

The rest of the chapter is organized as follows. Section 2.2 describes why the wireless technologies have been incorporated in industrial environments, underlines the key design requirements of critical IoT applications, and emphasizes the role of the aerospace communications. Section 2.3 outlines the potential critical applications of aerospace-based IoT.

2.2   Integration of Wireless Connectivity into the Industrial Domain

As the consumer-focused IoT is exponentially expanding around the world, its strong potential in critical applications in the industrial sector, for which the term Industrial IoT (IIoT) is typically used, becomes more explicit [3]-[5]. The IIoT, a sub-segment of the IoT, is the latest catalyst to process automation and was originated by General Electric. By integrating ultra-low power sensors interacting with data processing, Micro-Controller Units (MCUs), advanced network and communication

technologies, and powerful cloud-based analytics, IIoT intends to enable Cyber-Physical Systems (CPSs) and focuses on measuring production and operational factors, distributing data to business systems and humans within an organization, and improving business processes and profitability [5]. Applying IIoT and CPSs to the industrial domain brings closer the physical machines and the digital world and facilitates the autonomous prediction of failures, the triggering of the maintenance processes, the provision of advanced analytics and self-organized logistics to respond to the changes in the production. It also allows for the definition of the Industry 4.0 concept, where 4.0 alludes to a fourth industrial revolution enabled by advanced intelligent networking technologies [6], [7]. The first attempt to create an industrial network of "things" was about 40 years ago and is known as the Computer-Integrated Manufacturing (CIM) [8]. In 2014, the Industrial Internet Consortium, a non-profit partnership of industry, government, and academia, was created aiming at the development and evolution of the intelligent industrial automation.

The realization of the IIoT heavily depends on the adoption of advanced information, network, and communication technologies by traditional industries. The convergence between industrial networks and traditional networks, is also known as IT/OT convergence, where the Operational Technology (OT) refers to highly reliable and secure industrial networks and products, e.g., Programmable Logic Controllers (PLCs) and Remote Terminal Units (RTUs), and Information Technology (IT) refers to the Internet and the end-to-end flow control [9]. Similar to the IoT, the notion of IIoT is built upon the premise that a globally accessible communication infrastructure is available to a plethora of devices involved in the industrial processes. IIoT can be seen as an expansion of Supervisory Control And Data Acquisition (SCADA) networks and other global asset tracking applications, remote control, automated fabrication, collaborative robots, etc. The mission of a SCADA network is typically to report the status of equipment or track mobile assets, essentially acting as store and forward communications.

Nevertheless, system designers should consider a number of factors regarding the connectivity of the devices. Critical IIoT applications require higher availability, reliability and safety as well as lower latency to guarantee the end-user experience, as failure to such applications would result to severe consequences. As the number of distributed devices continuously increases, the network latency challenge becomes more severe in IIoT systems. The ISA-SP100 working group defines six different application classes (from Class 0 to Class 5) for industrial automation, involving sensors, actuators, and controllers depending on the required Quality-of-Service (QoS) [10], where Class 0 has the most stringent requirements regarding latency and reliability. Typical target values lie in the area of a few milliseconds for latency.

Although the majority of the devices in an industrial environment can be interconnected through homegrown wired technologies, e.g., Fieldbus technology [11], the most progressive manufacturers have started to integrate wireless Internet Protocol (IP)-enabled solutions for industrial sensing and control systems. The introduction of short- and long-range wireless communication technologies for locally and remotely connected production entities, respectively, introduces high flexibility, improves the security, and significantly reduces the operational cost for deployment and maintenance while drives new revenue through IIoT-based solutions. For localized IIoT applications, a short-range network based on wireless industrial standards, such as WirelessHART and ISA100.11a, is the most appropriate, allowing the use of unlicensed spectrum and maximizing battery life, while meeting networking needs [12]. Other wireless standards and protocols providing limited range and low-power consumption, such as Wireless Fidelity (Wi-Fi) HaLow based on IEEE 802.11ah, IPv6 over Low-Power Wireless Personal Area Networks (6LoWPAN), ZigBee, Bluetooth Low Energy (BLE), and Near Field Communication (NFC) may suffice depending on the application requirements. Besides, exploiting current and future conventional cellular networks and Low-Power Wide Area Network (LPWAN) 3rd Generation Partnership Project (3GPP) standards, e.g., Extended Coverage-Global System for Mobile Communications for

the IoT (EC-GSM-IoT), Narrowband-IoT (NB-IoT), and Long-Term Evolution for Machines (LTE-M), as well as non-3GPP standards [13], e.g., Long Range (LoRa) and SigFox, could address the needs for long-range communication of IIoT applications in the near term. Currently, the terrestrial wireless networks can only cover around 20% of territory in China and the U.S [14]. To effectively extend IIoT connectivity into remote and industrialized areas for asset monitoring, data aggregation and network backhaul applications, the use of aerospace networks is indispensable. Fig. 2.1 depicts the main requirements for the critical IIoT applications.
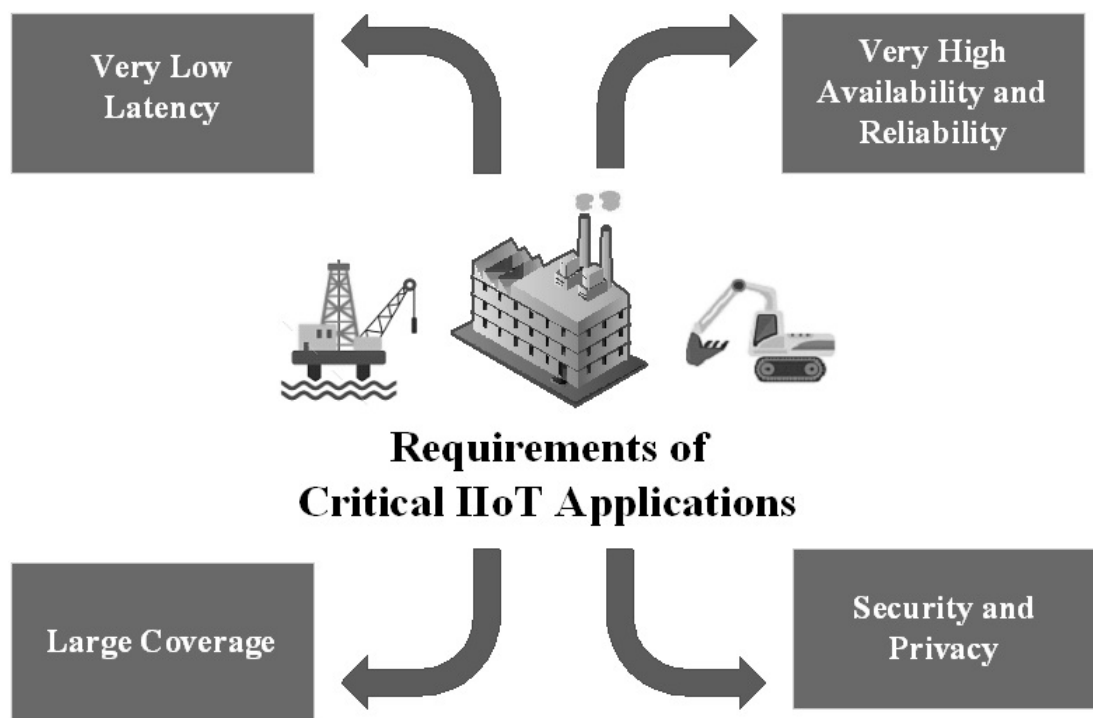
Fig. 2.1: Key design requirements of critical IIoT applications.

2.2.1 The Role of the Aerospace Communications

To ensure that IoT deployments will be succeed, connectivity must be constant enough to collect and transmit data between multiple devices. Effective connectivity is also necessary for the safety of the personnel in remote locations or

where safety or environmental hazards might be an issue, by ensuring availability during difficult times or emergencies. As previously mentioned, the IoT can exploit both 3GPP cellular-based and non-3GPP license-free terrestrial infrastructure. The former allows for large-scale device deployments aided by the mobile network operators and supports widely adopted wireless standards. However, a huge number of base stations is indispensable for global radio coverage. In addition, the terrestrial communication infrastructure is sensitive to natural disasters, e.g., earthquakes and floods. Thus, the IoT connectivity can be further enhanced and the services can be highly reliable and resilient by leveraging the aerospace infrastructure. Both satellites and aerial platforms are capable of simultaneously interconnecting a massive number of devices, while ensuring effectual management of data-intensive applications, redundant connections at critical sites, low latency, and enhanced capacity. In addition, the aerospace networks stand for an ideal fit for SCADA, since they are capable of delivering connectivity to locations that span thousands of miles in some of the world's most challenging environments.

Looking at evolving satellite technology development with respect to IoT, Inmarsat, the leading provider of global mobile satellite communications services, and other service providers predominantly use the L-band (1-2 GHz), which supports extremely low data rate IoT applications. As IoT takes hold over the next few years the network traffic will be significantly increased. Moreover, big data volumes generated from multiple sensors must be aggregated for predictive and prescriptive analytics, as well as real-time applications, such as surveillance and monitoring using Closed Circuit Television (CCTV). Hence, a higher bandwidth technology, notably Ka- and Ku-bands, will enable a broader range of satellite IoT applications. High Throughput Satellites (HTS), e.g., ViaSat-1 and EchoStar XVII, operating at Ka-band provide more than 100 Gbps of throughput. Although the majority of IoT applications may not need this kind of throughput, the related advantage of Ka/HTS is the significant decrease in the transmission cost-per-bit. With the exploitation of the Ku-band, service providers can leverage the large

number of open Ku-band satellites, which traditionally offer lower spectrum cost than L-band. Although using Ka- and Ku-bands seems beneficial, rain substantially affects signal propagation in mm-wave frequencies and a strong, dominant LoS signal is required for sufficient coverage due to the severe attenuation of the NLoS links. The realization of IoT and Machine-to-Machine (M2M) communications can be further reinforced due to the investments in new ground segment technologies, such as small, electronically steerable, and/or phased-array satellite transceivers, as well as the cost-effective CubeSat platforms based on micro-, nano-, and pico-satellites, operating as access points. According to Northern Sky Research (NSR), the M2M and IoT over satellite market will total more than 5.3 million terminals by 2024, whereas the Europe, Middle East and Africa (EMEA) market is projected to reach more than US$495 million in revenue by 2024.

In the context of satellite-based IoT applications, Inmarsat was the first to join the LoRa Alliance as its first satellite member and combine a low-power low-data-rate Long Range Wide Area Network (LoRaWAN) on the ground with a satellite mesh in the sky. For Inmarsat, the LoRa interest comes from the fact that in locations with terrestrial network constraints, users will look to satellite technology to provide the necessary IP backhaul to transfer data from LPWAN devices to applications on cloud platforms. Actility, an industry leader in LPWAN, has recently become part of Inmarsat's Certified Applications Provider Programme (CAPP). Aided by this partnership, a global L-band satellite connectivity platform can be effectually combined with the Actility's ThingPark IoT management platform. Hence, an integrated solution for IoT can be delivered and third-party companies can develop applications and solutions that are compatible with Inmarsat's satellite communications network. It is also expected that future 5G and IoT systems will include UAVs as autonomous communicating nodes for providing low latency and highly reliable connections between sensors and data collection points in cities, across suburban areas, and over rural terrains [15]. Drones can carry all range of sensors gathering massive amounts of valuable data [16]. Recently, Microsoft has deployed balloons in the stratosphere loaded with sensors and cameras and

connected to the Azure IoT platform, in order to send the telemetry to the field gateway through the Constrained Application Protocol (CoAP) [17].

More specifically, the satellite communications have the potential to promote the Internet of Remote Things (IoRT) [18] in scenarios with terrestrial network constraints, i.e., remote nodes, highly mobile nodes, and highly dispersed nodes over a wide geographical area. A typical example of IoRT is the Global Sensor Network (GSN) for remote environment observation, where massively connected IoT sensor networks are connected via LEO satellites [19]. Satellites have also a major role in assisting IoT systems to meet sub - 1 ms latency requirements by delivering commonly accessed content to mobile base stations and multi-casting content to caches located at individual cells, even in places without fiber. Although GEO satellites latency of 250 ms (500 ms round-trip time – RTT) is acceptable for many IIoT applications and is comparable with the RTT of a long terrestrial link (100-200 ms), MEO and LEO satellite constellations allow for lower latency in case of voice and video transmission (less than 100 ms RTT). HTS can also provide efficient backhauling of aggregated IoT traffic from multiple sites and transfer data from LPWANs devices to applications on cloud platforms. Nevertheless, the successful deployment and long-term operation of the aerospace systems necessitates the development of wireless standards for low-power aerospace IoT. Regulations related to the operation of satellites and aerial platforms may restrict how they can be used for IoT scenarios. Energy-efficient design of airborne systems is also required to extend flight duration. Finally, the security and the privacy threats introduced due to the vulnerability of the transmission medium are obviously another serious challenge when applying the aerospace communications to IoT. For instance, GEO satellites are relatively static to the ground, and hence it can be easily located and blanket jammed by enemies. To protect against eavesdroppers, the use of strong cryptographic/authentication protocols and physical layer security techniques [20] may be beneficial. Fig. 2.2 demonstrates a hybrid communication network consisting of terrestrial and aerospace infrastructures for IoT applications.
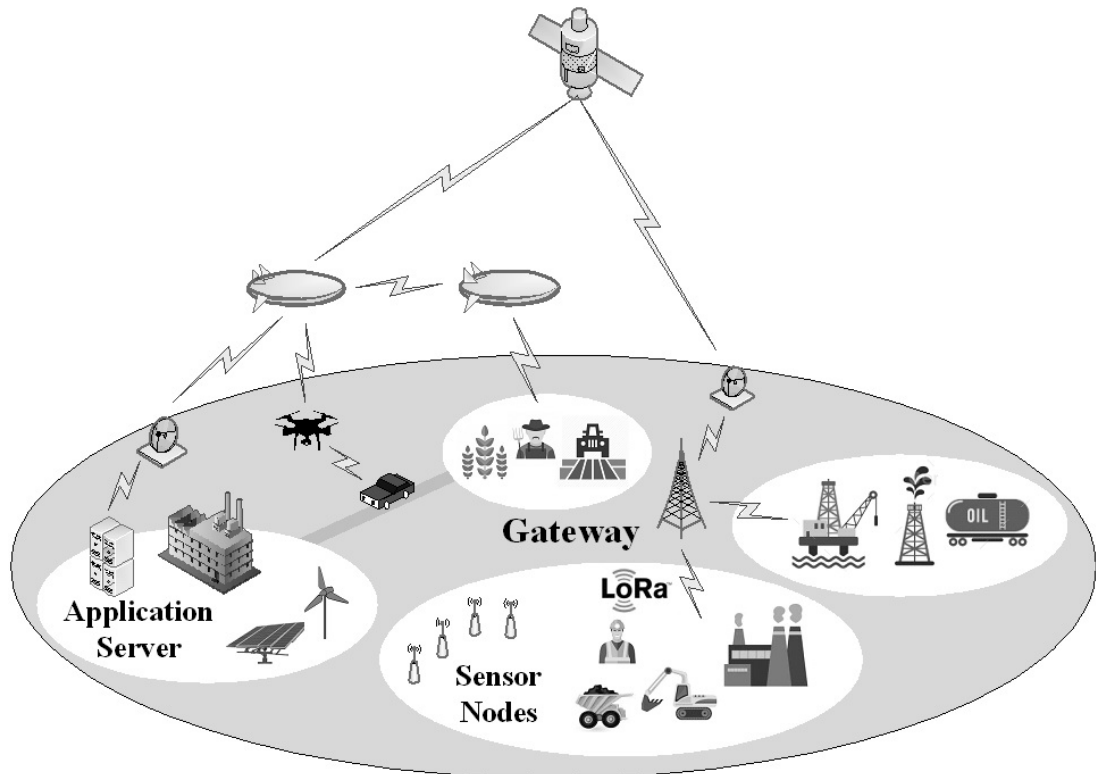
Fig. 2.2: A simple representation of a hybrid spaceborne-airborne-terrestrial communication network for IoT applications.

2.3   Potential Internet of Things Applications

As the IoT comprises a wide variety of applications, the challenging ones that will be benefited by the aerospace infrastructures require very high reliability and availability in terms of wireless connectivity. Although the average volume of data transported to and from devices may not be large, wide instantaneous bandwidths are useful in being able to meet latency requirements. The aerospace-based IIoT applications can be categorized into two groups; the delay-tolerant applications related with monitoring and forecasting and the delay-sensitive applications regarding enhanced supervisory control and data acquisition. Applications for aerospace-based IIoT tend to be those involving remote locations or extending over large land or sea areas, such as energy and smart grid, oil and gas pipeline integrity, and tracking of mining trucks. Applications regarding disaster and crisis

management in industrial environments are also worth mentioning. Despite the link with factories, manufacturing, and heavy industries, the term IIoT is also used to describe several IoT applications outside of the consumer IoT in a context of facility management, such as agriculture, transport systems, and healthcare. Typical examples of critical IIoT applications are the following:

Energy Applications: The aerospace infrastructure can efficiently handle a variety of electric grid automation and metering applications and support the integration and efficient use of all the energy resources and the electric grid infrastructure, using smart sensors, smart meters, and smart control [21]. As oil and gas production sites often operate in adverse environments and demanding conditions, there exists a wide range of applications in oil and gas that the aerospace infrastructure can effectively enable. These include monitoring and transmitting sensor data concerning drilling control, wellhead production, pipeline monitoring, distribution logistics and asset security. The measured operational parameters are transmitted to a control room, where a SCADA system adjusts set-points and provides control settings. The IIoT offers the foundation for a smarter grid for renewables that adapts to changing weather conditions and maximizes output. By combining different components in energy systems with sophisticated sensors, companies can collect important data remotely and therefore gain real-time essential insights into the overall operational condition of their projects, e.g., solar panels and wind turbines, depending on the environmental conditions, and ensure that the systems work at the maximum possible efficiency. By employing remote installations of UAVs, the human inspection of the facilities will be avoided.

Mining Applications: The IIoT can increase the productivity of the mining sector providing the building blocks for a smarter mine from the initial survey to the material extraction [3]. By deploying connected smart sensors in a network that can be adjusted to environmental conditions in real-time, IIoT makes it possible to automatically pick up data from previously elusive locations and for this data to be communicated rapidly to other devices. Drones allow for mineral exploration to be

conducted more quickly, whereas the autonomous drills, excavators and hauling trucks ensure the most efficient extraction. Besides, on-site health and safety for workers can be monitored and hence the injuries can be fewer.

Disaster and Crisis Management Applications: As the natural disaster or large-scale unexpected events easily make the terrestrial network overloaded or totally destroyed, hybrid spaceborne-airborne-terrestrial networks have the ability to provide more effective services compared to traditional infrastructures during emergency situations in industries. Aerospace networks can offer rapid deployment and wide coverage and successfully support applications such as video surveillance, structural monitoring and protection of critical infrastructure [22]. These include dams, bridges and other important structures, as well as security and access controls related to border control, flood warning, earthquake detection, early warning for possible fire disasters, weather and environmental monitoring, coastline and pipeline surveillance, trafficability of maritime routes, e.g., icebergs, and synthetic aperture radar applications. The Ka- and Ku-band satellite networks can efficiently support structural monitoring and protection of critical infrastructure and provide security and access controls, whereas the emergence of LAPs indicates a stable and reliable direction for the development of emergency network via circular flight tracks and continuous observation of regional hotspots and hazard areas.

Agriculture and Farming Applications: To efficient manage the water resources and irrigation systems, monitoring the weather, the air quality, the hydration levels, the water levels in reservoirs and soil moisture at the roots of plants, and detect acidity, nutrient, and water content, multiple sensor nodes may be deployed at different points across farming land and large remote plantations. A LoRaWAN gateway can provide the connectivity to the multiple sensors and send the data through a satellite or an aerial platform to a central cloud platform that will analyze this data and guide the farming activity. This optimizes water usage and irrigation schedules for precision agriculture, ensures consistent soil-water content for all

plants, enables smarter resource management in an area and reduces the amount of land required for production. Hence, farmers can make better decisions about the planting and harvesting of crops. Using the aerospace technology and the IIoT, the farming operations can also be monitored all the way from harvest to delivery [23]. Moreover, a reliable, long-range solution for tracking livestock and monitoring their location, health and safety is also viable by using tracking devices on each one of the animals.

Transportation Applications: The aerospace communications can improve the safety and management of transportation infrastructure and realize the Internet of Vehicles (IoV) [24]. Specifically, an expanded adoption of networking vehicles, sensors and controls can be achieved that will enable the smarter use of road and rail transportation by supporting applications such as, signage, signaling and routing, alerts for road and weather conditions, level crossing protection, and train control systems. The Global Positioning System (GPS) though satellites can determine the positioning of each vehicle, whereas HAPs represent a feasible solution for data acquisition in IoV, especially in rural areas. Besides, monitoring of vehicular traffics through drones with embedded cameras or sensors is also viable. By taking advantage of the aerospace infrastructure, the operation of commercial autonomous shipping can be enabled along with future commercial marine vessels, cargo logistics, and smart ports [25].

Medical Applications: As the Healthcare IIoT (HealthIIoT) will have a remarkable influence across the IIoT-driven healthcare industry [26], the aerospace networks combined with information and cloud technologies will support welfare and HealthIIoT applications and will be used for providing low-cost and timely healthcare in remote and inaccessible areas. These technologies have a profound effect on the quality, safety, and efficiency of healthcare. The patients and the aging society can be served by satellite based telemonitoring, medical diagnosis and care from their homes through IoT-powered In-Home Healthcare (IHH) services, whereas interaction though videoconferencing between medical

personnel and patients at home can be obtained. Moreover, using biomedical sensors, collection and transmission of medical data is feasible. However, the medical information should be protected from unauthorized access, which may result in the posting of personal information in the public domain. Hence, data protection in the form of watermarking and authentication is very important in a HealthIIoT system. Aerospace communications can also be used for monitoring endemics/epidemics at any area, while high bandwidth links can accommodate real-time medical imaging and remote robotic surgery [27].

REFERENCES

[1] H. S. Dhillon, H. Huang, and H. Viswanathan, "Wide-area Wireless Communication Challenges for the Internet of Things," *IEEE Commun. Magazine*, vol. 55, no. 2, pp. 168-174, Feb. 2017.

[2] N. Zhang, S. Zhang, P. Yang, O. Alhussein, W. Zhuang, and X. S. Shen, "Software Defined Space-Air-Ground Integrated Vehicular Networks: Challenges and Solutions," *IEEE Commun. Magaz.*, vol. 55, no. 7, pp. 101-109, 2017.

[3] L. D. Xu, W. He, and S. Li, "Internet of Things in Industries: A Survey," *IEEE Trans. on Industrial Informatics*, vol. 10, no. 4, pp. 2233-2243, Nov. 2014.

[4] J. Q. Li, F. R. Yu, G. Deng, C. Luo, Z. Ming, and Q. Yan, "Industrial Internet: A Survey on the Enabling Technologies, Applications, and Challenges," *IEEE Communications Surveys & Tutorials*, vol. 19, no. 3, pp. 1504-1526, thirdquarter 2017.

[5] S. Jeschke, C. Brecher, H. Song, and D. B. Rawat, *Industrial Internet of Things, Cybermanufacturing Systems*, Springer Series in Wireless Technology, 2017.

[6] M. Wollschlaeger, T. Sauter, and J. Jasperneite, "The Future of Industrial Communication: Automation Networks in the Era of the Internet of Things and Industry 4.0," *IEEE Industrial Electronics Magazine*, vol. 11, no. 1, pp. 17-27, Mar. 2017.

[7] A. Ustundag and E. Cevikcan, *Industry 4.0: Managing The Digital Transformation*, Springer Series in Advanced Manufacturing, 2018.

[8] A.-W. Scheer, *CIM. Computer Integrated Manufacturing*, Springer-Verlag Berlin Heidelberg, 1991.

[9] D. Dujovne, T. Watteyne, X. Vilajosana, and P. Thubert, "6TiSCH: deterministic IP-enabled industrial internet (of things)," *IEEE Commun. Magazine*, vol. 52, no. 12, pp. 36-41, Dec. 2014.

[10] ISA (2011) Wireless systems for industrial automation: process control and related applications.

[11] Nitaigour P. Mahalik, *Fieldbus Technology, Industrial Network Standards for Real-Time Distributed Control*, Springer-Verlag Berlin Heidelberg, 2003.

[12] S. Petersen and S. Carlsen, "WirelessHART Versus ISA100.11a: The Format War Hits the Factory Floor," *IEEE Industrial Electronics Magazine*, vol. 5, no. 4, pp. 23-34, Dec. 2011.

[13] K. Mekki, E. Bajic, F. Chaxel, and F. Meyer, A comparative study of LPWAN technologies for large-scale IoT deployment, *ICT Express*, 2018.

[14] Coverage Maps. Accessed: May 11, 2017. [Online]. Available: https://opensignal.com/networks

[15] H. Menouar, I. Guvenc, K. Akkaya, A. S. Uluagac, A. Kadri, and A. Tuncer, "UAV-Enabled Intelligent Transportation Systems for the Smart City: Applications and Challenges," *IEEE Commun. Magazine*, vol. 55, no. 3, pp. 22-28, Mar. 2017.

[16] S. A. R. Naqvi, S. A. Hassan, H. Pervaiz, and Q. Ni, "Drone-Aided Communication as a Key Enabler for 5G and Resilient Public Safety Networks," *IEEE Commun. Magazine*, vol. 56, no. 1, pp. 36-42, Jan. 2018.

[17] Pegasus II: Real-time Internet of Things experiment from the edge of space, 2016. [Online]. Available from: https://www.microsoft.com/en-us/research/blog/participate-in-pegasus-ii-real-time-internet-of-things-experiment-from-the-edge-of-space [retrieved: March, 2018].

[18] M. De Sanctis, E. Cianca, G. Araniti, I. Bisio and R. Prasad, "Satellite Communications Supporting Internet of Remote Things," *IEEE Internet of Things Journal*, vol. 3, no. 1, pp. 113-123, Feb. 2016.

[19] Z. Qu, G. Zhang, H. Cao and J. Xie, "LEO Satellite Constellation for Internet of Things," *IEEE Access*, vol. 5, pp. 18391-18401, 2017.

[20] G. Zheng, P.-D. Arapoglou, and B. Ottersten, "Physical Layer Security in Multibeam Satellite Systems," *IEEE Transactions on Wireless Communications*, vol. 11, no. 2, pp. 852-863, February 2012.

[21] K. Sohraby, D. Minoli, B. Occhiogrosso, and W. Wang, "A Review of Wireless and Satellite-Based M2M/IoT Services in Support of Smart Grids," *Mobile Netw Appl*, 2017. https://doi.org/10.1007/s11036-017-0955-1

[22] Y. Wang, Y. Xu, Y. Zhang, and P. Zhang, "Hybrid satellite-aerial-terrestrial networks in emergency scenarios: a survey," *China Communications*, vol. 14, no. 7, pp. 1-13, July 2017.

[23] M. Bacco, E. Ferro, and A. Gotta, "UAVs in WSNs for agricultural applications: An analysis of the two-ray radio propagation model," *IEEE SENSORS 2014 Proceedings*, Valencia, pp. 130-133, 2014.

[24] W. Xu et al., "Internet of vehicles in big data era," *IEEE/CAA Journal of Automatica Sinica*, vol. 5, no. 1, pp. 19-35, Jan. 2018.

[25] M. Höyhtyä, T. Ojanperä, J. Mäkelä, S. Ruponen, and P. Järvensivu, "Integrated 5G Satellite-*Terrestrial Systems: Use Cases for Road Safety and Autonomous Ships,"* in *Proc. 23rd Ka and Broadband Communications Conference 2017*, Trieste, Italy, Oct. 2017.

[26] M. S. Hossain and G. Muhammad, "Cloud-assisted Industrial Internet of Things (IIoT) – Enabled framework for health monitoring," *Computer Networks*, vol. 101, pp. 192-202, Jun. 2016.

[27] S. Srivastava, M. Pant, A. Abraham, and N. Agrawal, "The Technological Growth in eHealth Services," *Computational and Mathematical Methods in Medicine*, vol. 2015, Article ID 894171, 2015. doi:10.1155/2015/894171

3

Multi-User Single-Relay Aerospace Communications

3.1   Introduction

In this chapter, MU-MIMO aerospace systems are studied. In particular, this chapter adopts MIMO processing in MU relay networks and investigates the performance of a downlink multi-beam MIMO satellite communication system, where a terrestrial relay facilitates the communication process. The satellite radio channel is modeled using the Loo distribution, while the widely adopted Rician distribution is used in order to model the terrestrial channel. Since the receiver often observes a linear superposition of separately transmitted information that cannot be easily separated, this chapter utilizes the linear zero-forcing (ZF) [1] and the minimum mean square error (MMSE) [2] signal detection techniques, which are characterized by computational simplicity compared to non-linear techniques, and compares their performance in terms of the bit-error-rate (BER).

One of the major challenges of designing relay-based systems is to determine the proper placement of the relay, in order to achieve optimal or near-optimal performance. Several studies on the optimal horizontal and/or vertical placement and trajectory of aerial platforms have been previously conducted [3]-[19], especially for single-antenna systems based on UAVs. Part of the existing studies focused on the efficient deployment of aerial platforms as fixed/mobile base stations and aimed at maximizing the radio coverage [3]-[6]. Some of the previous works on the optimal position of aerial platforms assumed strong LoS signals [7]-[9], an assumption which may overestimate the channel gains in urban

environments due to possible fading effects, while others (e.g., [10]) investigated the influence of fading. A UAV-based MU system was also presented in [11] and intended to provide connectivity to a group of uniformly distributed ground users along a straight line. A similar alignment of the nodes was also assumed in [12]. The results in [11] were extended in [13], where multiple randomly dispersed users were considered. In [14]-[16], the optimal placement of aerial platforms as relays was studied regarding the relay-to-ground distance, while the elevation angle, the altitude, and the trajectory of relays were optimized in [17], [18], and [19], respectively. The results in [18] revealed that the optimization procedure of point-to-point systems significantly differs from the corresponding relay-based ones. To the best of the authors' knowledge, no previous work has ever optimized the position of relays in MS MD MIMO systems either in terrestrial or air-to-ground scenarios. Motivated by the aforementioned observations, this chapter also investigates the use of an aerial platform acting as a relay station between multiple SD pairs. Specifically, an MS MD MIMO relay system with orthogonal space-time block coding (OSTBC) transmission and rate-adaptive modulation is considered, which intends to provide both MU and spatial diversity gain, as well as low encoding/decoding complexity. Although MU MIMO point-to-point, SU MIMO relay-based, and MU MIMO relay-based systems with OSTBC were previously studied in [20], [21], and [22], respectively, an MS MD MIMO-OSTBC relay system has not been studied heretofore. Since a single relay may be incapable of simultaneously serving multiple SD pairs, the design of appropriate user scheduling schemes is required [23]. In this chapter, opportunistic scheduling is adopted and one SD pair with the best channel conditions is scheduled for transmission in a time-slot [24]. Expressions for the probability density function (PDF) and cumulative distribution function (CDF) of the E2E signal-to-noise ratio (SNR) are derived, which enable the establishment of a mathematical analysis of the performance in terms of the outage probability and the average spectral efficiency. Contrary to [11], [12] which assumed an unrealistic one-dimensional (1-D) uniform distribution of the users and/or the relay along a straight line, the main

contribution of this chapter is the development of two-dimensional (2-D) and three-dimensional (3-D) geometry-based optimization schemes for the relay placement. Analytical formulas are derived that can be used to estimate the optimal position of the relay with respect to a minimum outage probability. The optimization of the relay location and the power allocation are also jointly handled.

The rest of the paper is organized as follows. Section 3.2 presents a MIMO multi-relay satellite system, statistically models the satellite and terrestrial radio channels, focuses on signal detection techniques, and provides results. Section 3.3 describes the system and channel models of a MS MD MIMO aerial relay aided system, presents its geometrical characteristics, underlines the user-scheduling, derives expressions for the outage probability and spectral efficiency, demonstrates optimal system design recommendations, and provides results.

3.2 Multi-User MIMO Relay-Based Satellite Communications

This section considers an uplink multi-beam MIMO satellite system, where an AF terrestrial relay is assigned to assist the sources, i.e., the terrestrial stations, in forwarding their information to the destination, i.e., the satellite. It is assumed that the direct link between the source and the destination is obstructed due to high attenuation. The sources, the intermediate relay node, and the destination are equipped with $N_{S,i}$, N_R, and N_D antennas, respectively, where $i = 1,…,N_u$ and N_u is the total number of users. More specifically, the waves emitted from the source antennas travel over paths with different lengths and impinge the relay's antennas. Then, the relay node amplifies and forwards the received signal to the destination. Note that the users are far apart to interfere each other. The links between the sources and the relay represent the terrestrial links, while the link between the relay and the destination can be modeled as a satellite link. Fig. 3.1 demonstrates the system model, whereas Fig. 3.2 depicts the communication scenario. For simplicity, a system with two users-sources is plotted.
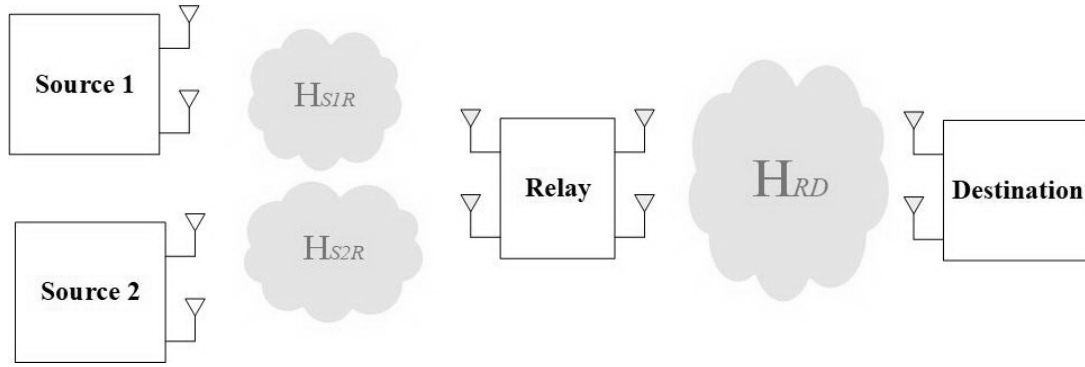
Fig. 3.1: A MU-MIMO relay-based satellite channel.
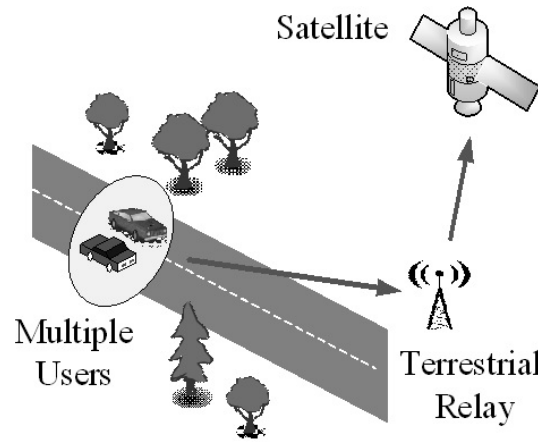
Fig. 3.2: Simple representation of a MU relay-based satellite system.

First, the MIMO subsystem for the communication link between the sources and the relay is considered. For this subsystem, the received signal at the relay from the i-th source is given by

$$\mathbf{y}_{R,i} = \mathbf{H}_{SR,i}\mathbf{x}_i + \mathbf{n}_{R,i},$$

(3.1)

where the matrix $\mathbf{H}_{SR,i}$ describes the MIMO channel between the ith user and the relay, $\mathbf{x}_i$ is the input data vector satisfying $\mathbf{R}_{x_i} = \mathsf{E}\left[\mathbf{x}_i\mathbf{x}_i^H\right]$, where $\mathsf{E}[\cdot]$ is the statistical

expectation operator, $(\cdot)^H$ denotes the complex conjugate (Hermitian) transpose operator, and $\mathbf{n}_{R_i}$ is the noise vector with additive white Gaussian noise (AWGN) at the relay's branches, whose variance is $\sigma_{SR,i}^2$, the autocorrelation matrix is $\sigma_{SR,i}^2 \mathbf{I}_{SR,i}$, and the covariance matrix is $\mathbf{R}_{nR,i} = \mathrm{E}\left[\mathbf{n}_{R,i}\mathbf{n}_{R,i}^H\right]$. The received signal vector at the destination is the summation of the relayed signals and is given by

$$\mathbf{y}_{D,i} = \sum_{i=1}^{N_u}\mathbf{H}_{RD}\mathbf{F}\mathbf{y}_{R,i} + \mathbf{n}_D, \tag{3.2}$$

where the matrix $\mathbf{H}_{RD}$ describes the MIMO channel between the relay and the destination, $\mathbf{F}$ is a relaying matrix denoting the linear signal processing unit, and $\mathbf{n}_D$ is the noise vector with AWGN at the destination's branches, whose variance is σ_D^2, the autocorrelation matrix is $\sigma_D^2 \mathbf{I}_D$, and the covariance matrix is $\mathbf{R}_{nD} = \mathrm{E}\left[\mathbf{n}_D\mathbf{n}_D^H\right]$. Note that $\mathbf{F} = a\mathbf{I}_{N_{R,i}}$, where a is the amplification factor of the relay and is assumed identical for each relay branch and $\mathbf{I}_{N_{R,i}}$ is an identity matrix of dimension $N_{R,i}$.

Using (3.1) and (3.2), the received signal in the destination becomes

$$\mathbf{y}_D = \sum_{i=1}^{N_u}\mathbf{H}_{RD}\mathbf{F}\left(\mathbf{H}_{SR,i}\mathbf{x}_i + \mathbf{n}_{R,i}\right) + \mathbf{n}_{R,i}. \tag{3.3}$$

The resulting channel for all the users can be expressed by

$$\mathbf{H} = \mathbf{H}_{RD} \odot \mathbf{B}, \tag{3.4}$$

where $\mathbf{H}$ is the channel matrix from relays to destination, $\mathbf{B}$ is the beam gain matrix of size [number of users × number of beams] and $\odot$ is the element wise multiplication [25]. It is considered that one user's position can be defined based on the angle ϑ between the beam center and the receiver location with respect to the satellite and $\vartheta_{3\mathrm{dB}}$ is the corresponding 3-dB angle [26]. More specifically, each element of the beam gain matrix can be calculated as follows [27]

$$b(\vartheta,k) = b_{max}\left(\frac{J_1(u)}{2u} + 36\frac{J_3(u)}{u^3}\right)^2, \tag{3.5}$$

where $u = 2.07123\ \sin\vartheta/\sin\vartheta_{3dB}$ and J_1 and J_3 are the first kind Bessel functions of order one and three, respectively. In addition, $b_{max} = \left(\frac{\lambda}{4\pi}\right)^2 \frac{1}{(d_0)^2}$, where λ is the carrier wavelength and $d_0 \simeq 3,579 km$ [25], [28]. For simplicity purposes, the earth curvature and the satellite orbit geometry are not accounted for in the channel model. Subsequently, the variations in the distances of the beam centers and the distance between the satellites are not modeled. The assumption that the centers of all beams are equidistant from the satellite can be supported only for small coverage areas.

3.2.1 Statistical Channel Modeling

In this section, a statistical modeling approach for the satellite and the terrestrial channel is described. Specifically, the Rician distribution is utilized, in order to model the terrestrial channel. Then, a strong LoS signal also arrives at the receiver branches and the fading envelope follows a Rice distribution. In addition, the satellite channel is modeled using the experimentally verified Loo distribution [29], where the long-term shadowing due to roadside trees affects only the LoS component and is described through a log-normal distribution, whereas the NLoS component is described by a Rayleigh PDF. Hence, the resulting complex signal envelope is the sum of correlated lognormal and Rayleigh processes. The Loo distribution assumes that the foliage not only attenuates but also scatters the radio waves.

The terrestrial wireless radio channel is mostly characterized by the surrounding local scatterers in the vicinity of the terrestrial nodes, which produce multipath components. Since a strong LoS component is also present, the propagation environment can be characterized using the Rician distribution as follows [30]

$$\mathbf{H}_{SR,i} = \sqrt{\frac{K_i}{K_i + 1}} \overline{\mathbf{H}}_{SR,i} + \sqrt{\frac{1}{K_i + 1}} \tilde{\mathbf{H}}_{SR,i},$$ (3.6)

where K_r is the Rician factor, which expresses the relative power of the direct and scattered components of the received signal for the link between the relay and the destination and provides an indication of the link quality, $\overline{\mathbf{H}}_{R,D}$ is a deterministic unit rank matrix, which represents the direct component, and $\tilde{\mathbf{H}}_{R,D}$ is the channel matrix of the multipath components. When $K_r = 0$ the channel is described by a Rayleigh distribution, whereas a very large value of K_r, i.e., $K_r \to \infty$, implies the presence of a Gaussian channel.

Using the Loo distribution for the satellite channel, the channel matrix of the satellite link for the envelope h_{ij} is given by

$$\mathbf{H}_{RD} = \left[h_{ij} \right] = \left[\overline{h_{ij}} \right] + \left[\tilde{h_{ij}} \right] = \overline{\mathbf{H}}_{RD} + \tilde{\mathbf{H}}_{RD},$$ (3.7)

where

$$h_{ij} = \left| h_{ij} \right| \exp\left(j\phi_{i,j} \right)$$
$$= \left| \overline{h_{ij}} \right| \exp\left(j\overline{\phi_{i,j}} \right) + \left| \tilde{h_{ij}} \right| \exp\left(j\tilde{\phi_{i,j}} \right)$$ (3.8)

and $\overline{\phi_{i,j}}$, $\tilde{\phi_{i,j}}$ are uniformly distributed over $\left[0, 2\pi \right]$. The first factor represents the log-normal fading, while the second one describes the Rayleigh fading. Therefore, the Loo distribution extracted from (3.8) is the superposition of the log-normal distribution to model the large-scale fading and Rayleigh distribution for the modeling of small-scale fading. Specifically, the Loo probability density function is given by

$$p\left(\left| h_{ij} \right| \right) = \frac{\left| h_{ij} \right|}{b_0 \sqrt{2\pi\sigma^2}} \int_0^{\infty} \frac{1}{\overline{h_{ij}}} \exp\left[-\frac{\left(\ln \overline{h_{ij}} - \mu \right)^2}{2\sigma^2} - \frac{\left| \overline{h_{ij}} \right|^2 + \overline{h}_{ij}^2}{2b_0} \right] I_0 \left(\frac{\left| h_{ij} \right| \overline{h_{ij}}}{b_0} \right) d\overline{h_{ij}},$$ (3.9)

where b_0 is the average scattered power resulting from the multipath components, σ and μ are the standard deviation and mean, respectively, and $I_0(\cdot)$ is the zeroth-order modified Bessel function of the first kind.

3.2.2 Linear Signal Detection Schemes

In MIMO systems, spatial multiplexing is exploited, where multiple streams of independent data are transmitted from the transmitting antennas. These streams should be then separated at the receiver by means of appropriate processing techniques. Hence, signal detection is required for the signals. In spatial multiplexing MIMO systems, the optimum receiver would be the non-linear maximum likelihood (ML) receiver. However, the problem cannot be decomposed in scalar problems, since the columns of the channel matrix **H** are not orthogonal. Hence, joint detection should be performed. The complexity of ML decoding exponentially increases with the number of receive antennas. Therefore, suboptimum in terms of diversity order, techniques with decreased complexity have been developed.

In this section, the Zero-Forcing (ZF) and the Minimum Mean Squared Error (MMSE) linear signal detection techniques are used, which represent two standard linear signal detection methods for MIMO spatial multiplexing systems and are characterized by their simplicity, versatility, and ease of extracting performance metrics. In linear signal detectors, a linear transform is applied to the outputs of conventional matched filters to produce a new set of outputs, which may generate better results. These detectors treat all transmitted signals as interferences except for the desired stream from the target antenna at the transmitter. Therefore, interference signals from other antennas are minimized or nullified in the course of detecting the desired signal from the target antenna. To facilitate the detection of signals from each antenna, the estimated symbols are inverted by a weight matrix **W** as follows [31]

$$\tilde{\mathbf{x}} = \begin{bmatrix} \tilde{x}_1 \, \tilde{x}_2 \cdots \tilde{x}_{N_t} \end{bmatrix}^T = \mathbf{W}\mathbf{y}, \tag{3.10}$$

where $\mathbf{y} = \mathbf{H}\mathbf{x} + \mathbf{n}$ is the receive vector, $\mathbf{H}$ is the channel matrix, $\mathbf{x}$ is the transmit vector, and $\mathbf{n}$ is the noise vector for a generic MIMO communication system. Hence, a linear combination of the received signals in the destination node is considered. Note that there is one detection for each symbol, which depends on the number of the transmit antennas.

The ZF receiver, called also decorrelator or interference nulling receiver, is the simplest MIMO detector and attempts to cancel out the interstream interference using the Moore-Penrose pseudoinverse of the channel matrix $\mathbf{H}$. This matrix is either the left inverse of matrix $\mathbf{H}$, that is, $\mathbf{W}_{ZF}\mathbf{H} = \mathbf{I}_{N_R}$ for $N_T \geq N_R$, where $\mathbf{W}_{ZF}$ is the weight matrix of the ZF technique, and it holds that $\mathbf{W}_{ZF} = \left(\mathbf{H}^H \mathbf{H} \right)^{-1} \mathbf{H}^H$, where $(\cdot)^H$ is the Hermitian transpose operation, or the right inverse of $\mathbf{H}$, that is, $\mathbf{H}\mathbf{W}_{ZF} = \mathbf{I}_{N_T}$ for $N_R \geq N_T$, and it holds that $\mathbf{W}_{ZF} = \mathbf{H}^H \left(\mathbf{H}\mathbf{H}^H \right)^{-1}$. The ZF detection technique assumes that the base station has perfect knowledge of the channel state information (CSI) of all users' equipment present at the receiver. By pre-multiplying the received vector with the pseudo-inverse we get

$$\tilde{\mathbf{x}}_{ZF} = \mathbf{W}_{ZF}\mathbf{y} = \mathbf{W}_{ZF}\mathbf{H}\mathbf{x} + \mathbf{W}_{ZF}\mathbf{n} = \mathbf{x} + \mathbf{W}_{ZF}\mathbf{n}. \tag{3.11}$$

The noise enhancement effect plaguing the ZF detection technique can be reduced by using the MMSE detection technique, which is also considered suboptimal and exploits the knowledge of noise variance to maximize the SINR. To maximize the post-detection signal to interference plus noise ratio (SINR), the MMSE weight matrix is given by [31]

$$\mathbf{W}_{MMSE} = \left(\mathbf{H}^H \mathbf{H} + \sigma_n^2 \mathbf{I}_{N_T} \right)^{-1} \mathbf{H}^H. \tag{3.12}$$

The MMSE receiver uses the statistical information of noise σ_n^2. Thus, using the MMSE weight in (3.11), we obtain

$$\tilde{\mathbf{x}}_{MMSE} = \mathbf{W}_{MMSE}\mathbf{y}_2$$

$$= \left(\mathbf{H}^H\mathbf{H} + \sigma_n^2\mathbf{I}\right)^{-1}\mathbf{H}^H\left(\mathbf{H}\mathbf{x} + \mathbf{n}\right)$$

$$= \underbrace{\left(\mathbf{H}^H\mathbf{H} + \sigma_n^2\mathbf{I}\right)^{-1}\mathbf{H}^H\mathbf{H}\mathbf{x}}_{1} + \left(\mathbf{H}^H\mathbf{H} + \sigma_n^2\mathbf{I}\right)^{-1}\mathbf{H}^H\mathbf{n}$$

$$= \mathbf{x} + \left(\mathbf{H}^H\mathbf{H} + \sigma_n^2\mathbf{I}\right)^{-1}\mathbf{H}^H\mathbf{n}. \tag{3.13}$$

It can be proved that compared to ZF, the MMSE receiver avoids noise amplification but suffers from remaining interference.

The capacity of a MIMO channel using a linear detector is given by

$$C_{LD} = \sum_{i=1}^{k}\log_2\left(1 + SINR_k\right), \tag{3.14}$$

where the $SINR_k$ for each receiver is different. The SINR for the MMSE receiver for the *kth* spatial stream can be expressed as [32]

$$SINR_k^{MMSE} = \frac{1}{\left[\left(\mathbf{I}_{Nt} + SNR*\mathbf{H}^H\left(\mathbf{R}_n\right)^{-1}\mathbf{H}\right)^{-1}\right]_{kk}} - 1, \tag{3.15}$$

where $\mathbf{I}_{Nt}$ is a $N_t \times N_t$ identity matrix and $\mathbf{H}^H$ is the Hermitian transpose of $\mathbf{H}$. The SINR for the ZF receiver denoted by $SINR_k^{ZF}$ can be expressed as follows by conditioning on $\mathbf{H}$ [33]

$$SINR_k^{ZF} = \frac{SNR}{\left[\left(\mathbf{H}^H\left(\mathbf{R}_n\right)^{-1}\mathbf{H}\right)^{-1}\right]_{kk}}. \tag{3.16}$$

3.2.3 Numerical Results

This section demonstrates the performance of the proposed communication scenario in terms of the BER and the available channel capacity. Note that the Rician factor is set to 8 dB for all the terrestrial links. Fig. 3.3 demonstrates the end-to-end BER performance for different signal detection schemes and different number of users-sources. Quadrature phase shift keying (QPSK) modulation is used,

since satellite communications are sensitive to data loss due to the limited resources. According to the results, the best performance is achieved with MMSE. In addition, the two-users system outperforms the SU system. In Fig. 3.4, the advantage of the MMSE technique over the ZF technique is depicted in terms of the channel capacity. However, this advantage is nullified as the SNR increases. Finally, Fig. 3.5 demonstrates the channel capacity as a function of the number of users-sources and the number of antennas at the sources, when a MMSE signal detection scheme is exploited. One observes that the capacity increases as the number of single-antenna users-sources increases. However, when the users-sources are equipped with a large number of antennas, increasing the number of user-sources has an insignificant effect on the capacity.
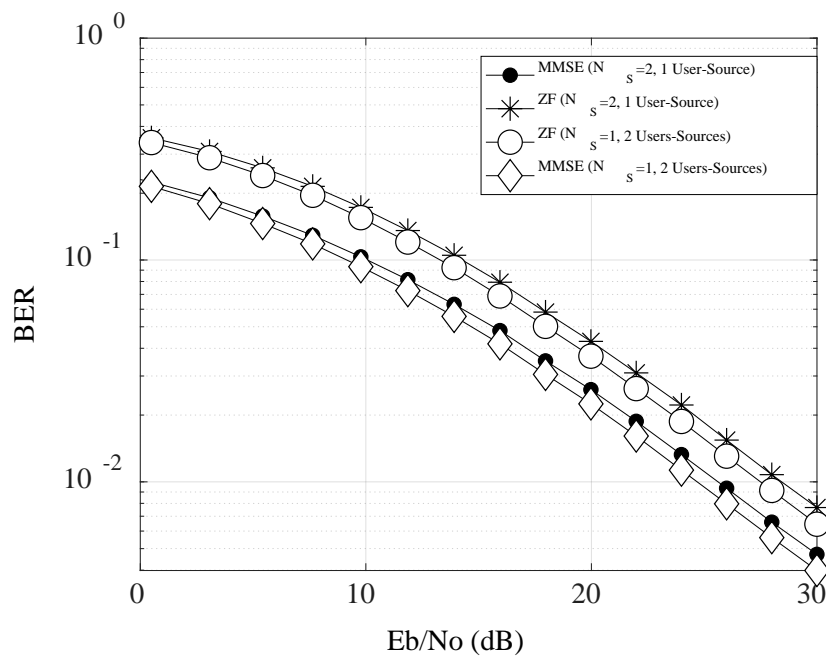
Fig. 3.3: End-to-end BER performance of a MU-MIMO satellite communication system for different signal detection schemes, where a single user-source equipped with two antennas or two users-sources equipped with single antennas are used.
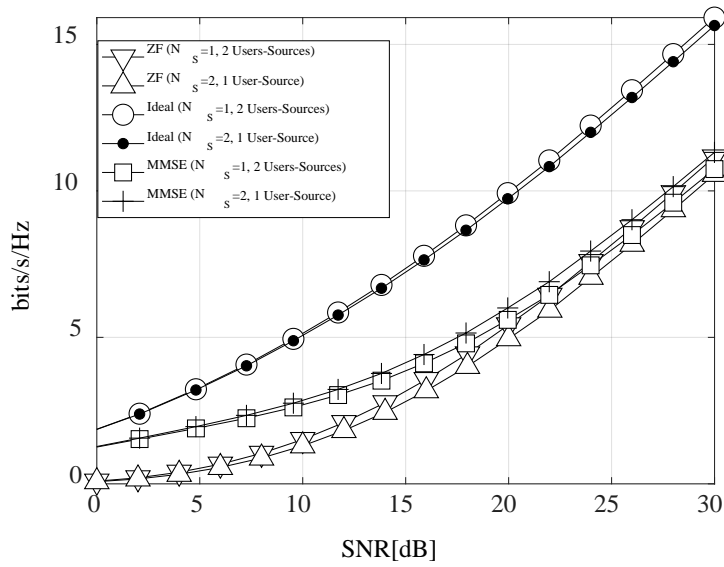
Fig. 3.4: Channel capacity of a MU-MIMO satellite communication system for different signal detection schemes, where a single user-source equipped with two antennas or two users-sources equipped with single antennas are used.
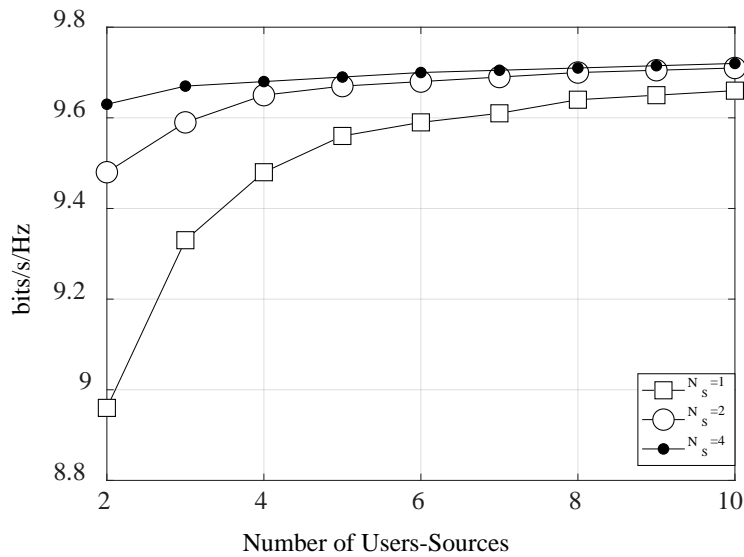
Fig. 3.5: Channel capacity of a MU-MIMO satellite communication system for different number of users-sources and different number of antennas at the users-sources.

# 3.3 Optimal Aerial Relay Placement for Multi-User MIMO Communications

This section considers a MIMO-OSTBC airborne communication system in slowly-varying, frequency-flat channels. In this system, K SD pairs try to communicate through a DF aerial relay platform. Although the amplify-and-forward AF scheme is simple to implement, DF offers better performance [18] and thus it has been widely adopted in cooperative networks. It is assumed that the direct links between the sources and the destinations are obstructed due to high attenuation in the propagation medium. Moreover, carrier frequencies well below 10 GHz are considered. Hence, both LoS and NLoS connections may exist in all transmission links, whereas rain effects are insignificant. To make all the links have the same transmission rate, it is assumed that all users and the relay employ uniform linear arrays (ULAs) with the same number of antennas, L, and hence they all use the same OSTBC structure. Nevertheless, the results can be extended to scenarios, where an arbitrary number of antennas exists.

To aid our analysis, S_k, R, and D_k, with $1 \leq k \leq K$, are affiliated with the k-th source, the relay, and the k-th destination, respectively. All of the SD pairs are belong to the set U, where $U = \{1,2,...,K\}$ and the k-th SD pair is denoted by (S_k, D_k). Due to hardware limitations, the link operates in a HD mode and the communication is conducted over two phases; the first phase includes the link between S_k and R, while the second phase involves the link between R and D_k. Time is divided in time-slots and multiple access is based on TDMA, where at each time-slot one SD pair is activated for transmission. As shown in Fig. 3.6, the MIMO channel between the source (destination) and the relay is expressed by the channel transfer matrix $\mathbf{H}_{S_k R} \in \mathbb{C}^{L \times L}$ $\left(\mathbf{H}_{RD_k} \in \mathbb{C}^{L \times L} \right)$ containing the complex faded channel gains $h_{S_k R, ji}$ $\left(h_{RD_k, ji} \right)$ between the i-th source (relay) and the j-th relay (destination) antennas for the user k. The elements of the channel matrices undergo

independent Nakagami-*m* fading, whereas the signal is degraded by AWGN at the receiver with variance denoted by N_o and being equal in all cases.

It is considered that groups of *G* transmitted symbols $s_{k,1}$, $s_{k,2}$,..., $s_{k,G}$ are selected from the signal constellation with average energy $\mathsf{E}\left[\left|s_{k,g}\right|^2\right]=1$, where $\mathsf{E}[\cdot]$ denotes expectation and $g=1,2,...G$. These symbols are encoded by an OSTBC matrix $\mathbf{C}_1 \in \mathbb{C}^{L \times T}$, for which the entries are linear combinations of $\left\{s_{k,g}\right\}_{g=1}^{G}$ and their complex conjugates with the exact construction depending on the specific OSTBC used. Note that *T* denotes the number of symbol periods used to send each OSTBC codeword. Hence, the code rate is $R_c = G/T$. The received signal matrix $\mathbf{Y}_{S_k R} \in \mathbb{C}^{L \times T}$ at the relay from the *k*-th source during the *t*-th symbol period in the first time slot is given by [21]

$$\mathbf{Y}_{S_k R} = \sqrt{\frac{P_S}{L}}\mathbf{H}_{SR}\mathbf{C}_1 + \mathbf{N}_R, \tag{3.17}$$
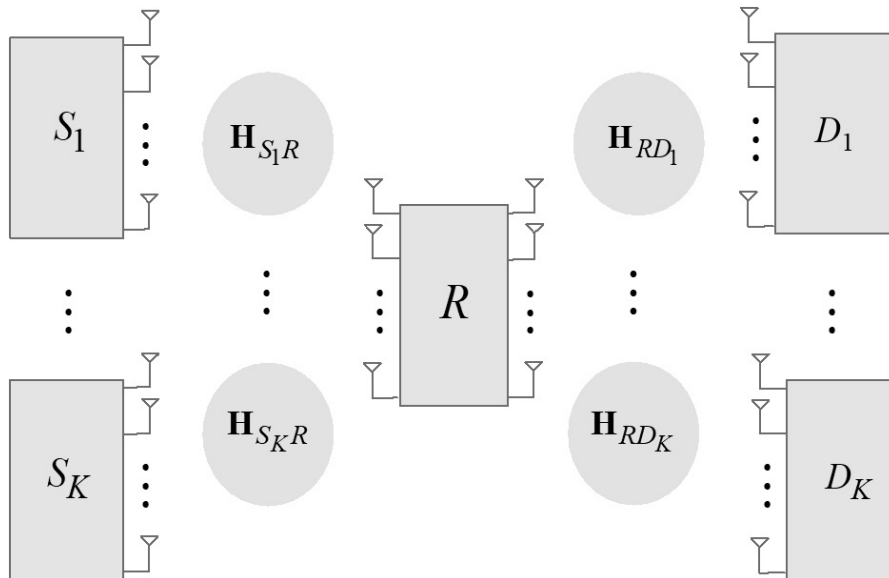
Fig. 3.6: The MS MD MIMO relay fading channel.

where P_S is the total source transmit power and $\mathbf{N}_R \in \mathbb{C}^{L \times T}$ is the noise matrix at the relay whose elements are modeled as independent and identically distributed (i.i.d.) complex Gaussian random variables with zero mean and variance N_o per dimension.

Since the orthogonal structure of the OSTBC can transform a MIMO channel into an equivalent SISO channel [34], the combined received signal at the relay from the k-th source is given by [20], [35]

$$y_{S_k R, g} = \sqrt{\frac{P_S}{L}} c \left\| \mathbf{H}_{S_k R} \right\|_F^2 s_{k,g} + n_{R,g}, \qquad (3.18)$$

where c is a constant that depends on the particular OSTBC used (e.g., $c = 1$ corresponds to the Alamouti scheme), $\left\| \mathbf{H}_{S_k R} \right\|_F^2 \triangleq \mathrm{tr}\left(\mathbf{H}_{S_k R} \mathbf{H}_{S_k R}^\dagger \right) = \sum_{j=1}^{L} \sum_{i=1}^{L} \left| h_{S_k R, ij} \right|^2$, $\left\| \cdot \right\|_F^2$ is the squared Frobenius norm of a matrix, $\mathrm{tr}(\cdot)$ denotes the trace operator, $\dagger$ denotes the transpose conjugate of a matrix, and $n_{R,g}$ is the filtered zero-mean complex Gaussian noise at the relay with variance $cN_o \left\| \mathbf{H}_{S_k R} \right\|_F^2$. The total energy of the symbol transmitted through the source antennas can be normalized to the number L of these antennas and hence, the instantaneous SNR per symbol at the relay can be written as [20], [35]

$$\gamma_{S_k R} = \frac{\overline{\gamma}_{S_k R}}{L m_{SR} R_c} \left\| \mathbf{H}_{S_k R} \right\|_F^2, \qquad (3.19)$$

where $\overline{\gamma}_{S_k R}$ is the average SNR per antenna and $m_{SR} \geq 1/2$ is the Nakagami-m fading parameter, which is assumed identical for all the users of the S_k-R links. From (3.19) one observes that the performance of STBC depends on the statistical properties of the squared Frobenius norm of the channel matrix.

In this section, a channel state information (CSI)-assisted DF relay scheme is adopted. More specifically, centralized CSI acquisition is assumed, where at the start of each time-slot, each SD pair transmits a pilot sequence to the relay. By

assuming that the reciprocity property of antennas holds, the relay is able to estimate the CSI of the links of each SD pair. Next, the relay broadcasts the index of the SD pair with the best E2E SNR and this pair is activated for transmission. Moreover, relay positioning and power allocation information is transmitted to achieve the minimum outage probability subject to the total power constraint. Then, the signals $y_{S_k R, g}$ are encoded by an STBC matrix $\mathbf{C}_2$ with a rate R_c and are sent to the k-th destination. The received signal matrix $\mathbf{Y}_{D_k}$, the combined received signal $y_{D_k, g}$, and the instantaneous SNR γ_{RD_k} per symbol at the k-th destination can be defined as in (3.17), (3.18), and (3.19), respectively, by replacing the indices. The instantaneous E2E SNR per symbol at the k-th destination is given by

$$\gamma_{D_k} \simeq \min\left\{\gamma_{SR_k}, \gamma_{RD_k}\right\}. \tag{3.20}$$

To analyze the performance of the proposed system, one should obtain the statistics of the E2E SNR provided in (3.20).

Let δ_S, δ_R, and δ_D denoting the spacing between two adjacent antenna elements at the sources, relay, and destinations, respectively. In this context, it is assumed that $(L-1)\delta_S$ and $(L-1)\delta_D$ are much smaller than the distance between any of the users and that $(L-1)\delta_R$ is much smaller than the distance between any of the users and the relay. Then, the channel gains $\left\{h_{S_k R, ij}\right\}$ and $\left\{h_{RD_k, ij}\right\}$ have mean power $\mathrm{E}\left[\left|h_{S_k R, ij}\right|^2\right] \propto d_{S_k R}^{-a}$ and $\mathrm{E}\left[\left|h_{RD_k, ij}\right|^2\right] \propto d_{RD_k}^{-a}$, respectively, where $d_{S_k R}$ $\left(d_{RD_k}\right)$ is the distance between the k-th source (relay) and the relay (k-th destination) and a is the path loss exponent, which is assumed identical to all links. Since these proportionalities cannot be directly applied, the proportionality factors should be evaluated. The path loss exponent for air-to-ground links, closely follows the exponent observed in free-space path-loss [36], [37]. Hence, assuming $a=2$ and unity antenna gains and adopting the Frii's formula [38], we obtain

$$E\left[\left|h_{S_kR,ij}\right|^2\right] \approx \left(\frac{\lambda}{4\pi}\right)^2 d_{S_kR}^{-2}, \tag{3.21}$$

$$E\left[\left|h_{RD_k,ij}\right|^2\right] \approx \left(\frac{\lambda}{4\pi}\right)^2 d_{RD_k}^{-2}, \tag{3.22}$$

where λ is the carrier wavelength. Using (3.21) and (3.22), the average SNR per antenna at the relay and the k-th destination node can be written, respectively, as

$$\overline{\gamma}_{S_kR} = \frac{P_S}{N_o}E\left[\left|h_{S_kR,ij}\right|^2\right] \approx \frac{P_S}{N_o}\left(\frac{\lambda}{4\pi}\right)^2 d_{S_kR}^{-2}, \tag{3.23}$$

$$\overline{\gamma}_{RD_k} = \frac{P_R}{N_o}E\left[\left|h_{RD_k,ij}\right|^2\right] \approx \frac{P_R}{N_o}\left(\frac{\lambda}{4\pi}\right)^2 d_{RD_k}^{-2}, \tag{3.24}$$

where P_R is the total relay transmit power.

3.3.1 Channel Statistics

To model the channel fading distribution in air-to-ground propagation scenarios, the Rician, Rayleigh, and Nakagami-m distributions have been suggested [36]. This section considers that the channel behavior is subjected to independent but non-identically distributed (i.n.i.d.) Nakagami-m fading conditions [20]. The Nakagami-m distribution includes other well-known ones as special cases, whereas it has also the important advantage of approximating other distributions. Since the Nakagami-m distribution is utilized to model the channels fading behavior for the S_k–R and R–D_k links, the PDF of $\left|h_{S_kR,ij}\right|$ can be expressed $\forall x \geq 0$, $m_{SR} \geq 1/2$, and $\Omega_{SR} > 0$, as [39]

$$f_{\left|h_{S_kR,ij}\right|}(x) = \frac{2m_{SR}^{m_{SR}}x^{2m_{SR}-1}}{\Omega_{SR}^{m_{SR}}\Gamma(m_{SR})}\exp\left(-\frac{m_{SR}x^2}{\Omega_{SR}}\right), \tag{3.25}$$

where Ω_{SR} is the power scaling parameter, which is assumed identical for all the users of the S_k-R links, and $\Gamma(a) = \int_0^\infty t^{a-1}e^{-t}dt$ is the complete Gamma function [40,

eq. (8.310/1)]. Using (3.25) for $m_{SR} = 1$, the Rayleigh distribution can be obtained. The PDF in (3.25) can also approximately describe the Rician fading for $m_{SR} = \left(K_{SR} + 1 \right)^2 / \left(2K_{SR} + 1 \right)$, where K_{SR} is the Rician factor of the S_k–R links, i.e., the average power ratio of the strong LoS component to the NLoS component. Thus, depending on the value of the parameter $m_{SR} \left(m_{RD} \right)$, the S_k–R and R–D_k links may experience either symmetric, e.g., Rician/Rician, or asymmetric, e.g., Rayleigh/Rician, fading phenomena. The value of the Rician factor strongly depends on the elevation angle of the relay and the operating frequency and varies between 0.9 and 28 dB, as experimentally verified in [41], [42]. However, the value of the Rician factor is directly related with the propagation area and is expected to be lower in highly urbanized areas, where the scatterers are usually dense and tall.

Although the received fading amplitudes in all user antennas are i.i.d., these fading amplitudes may be i.n.i.d. for two distinct users. Then, $\left\| \mathbf{H}_{S_k R} \right\|_F^2$ and the received SNR $\gamma_{S_k R}$ (for each user in OSTBC) are distributed as Gamma random variables with parameter $m_{SR} \xi$ and mean $m_{SR} \xi \overline{\gamma}_{S_k R} / L m_{SR} R_c = L \overline{\gamma}_{S_k R} / R_c$, where $\xi = L \times L$. The PDF of the instantaneous SNR received at R is given by [20]

$$f_{\gamma_{S_k R}} \left(\gamma_{S_k R} \right) = \left(\frac{m_{SR} \mu}{\overline{\gamma}_{S_k R}} \right)^{m_{SR} \xi} \frac{\gamma_{S_k R}^{m_{SR} \xi - 1}}{\Gamma \left(m_{SR} \xi \right)} \exp \left(-\frac{m_{SR} \mu \gamma_{S_k R}}{\overline{\gamma}_{S_k R}} \right), \tag{3.26}$$

where $\mu = L R_c$. Besides, the CDF of the instantaneous SNR received at R can be expressed as [43]

$$F_{\gamma_{S_k R}} \left(\gamma_{S_k R} \right) = \frac{1}{\Gamma \left(m_{SR} \xi \right)} \Gamma \left(m_{SR} \xi, \frac{m_{SR} \mu \gamma_{S_k R}}{\overline{\gamma}_{S_k R}} \right), \tag{3.27}$$

where $\Gamma \left(n, x \right) = \Gamma \left(n \right) \exp \left(-x \right) \sum_{k=0}^{n-1} \frac{x^k}{k!}$ stands for the upper incomplete Gamma function [40, eq. (8.350/2)]. The PDFs of $\left| h_{RD_k, ij} \right|$ and γ_{RD_k} and the CDF of γ_{RD_k} can be defined as in (3.25), (3.26), and (3.27), respectively, by replacing the indices.

3.3.2 Geometrical Characteristics

To develop the optimization problem, this section considers realistic 3-D positioning of the terrestrial users and the aerial relay platform. The geometrical characteristics of the system under consideration for the $S_1 - D_1$ and $S_k - D_k$ user pairs are shown in Figs. 3.7 and 3.8. Fig. 3.7 presents a 3-D view of this system, while Fig. 3.8 presents the projection of this system to the *x-y* plane. One observes that the *x*-axis is the line that connects the coordinate origin S_1 with D_1. To aid our analysis, we denote as d_{ab} the distance between two points a and b. Then, $H_R = d_{R\tilde{R}}$ is the altitude of the relay, corresponding to the minimum altitude above the ground level required for safety considerations, e.g., terrain or building avoidance, and $\tilde{R}$ is the sub-platform point (SPP) denoting the projection of R onto the *x-y* plane. The location of the relay seen from S_1 (D_1) can be specified by the azimuth angle $\omega_{S_1 R}$ $\left(\omega_{RD_1} \right)$ and the elevation angle $\beta_{S_1 R}$ $\left(\beta_{RD_1} \right)$.
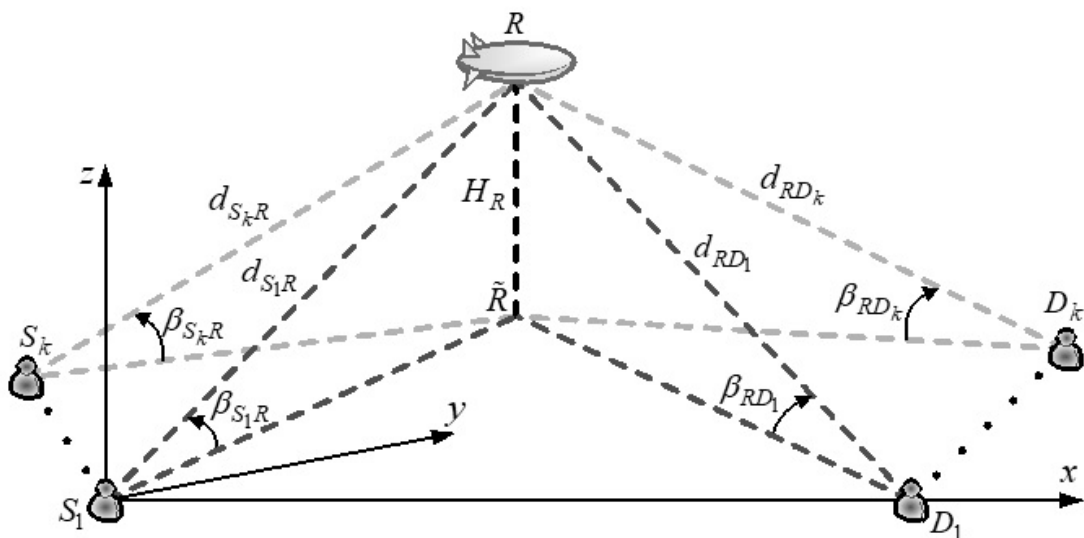
Fig. 3.7: Geometrical characteristics of the MS MD aerial platform aided communication system.
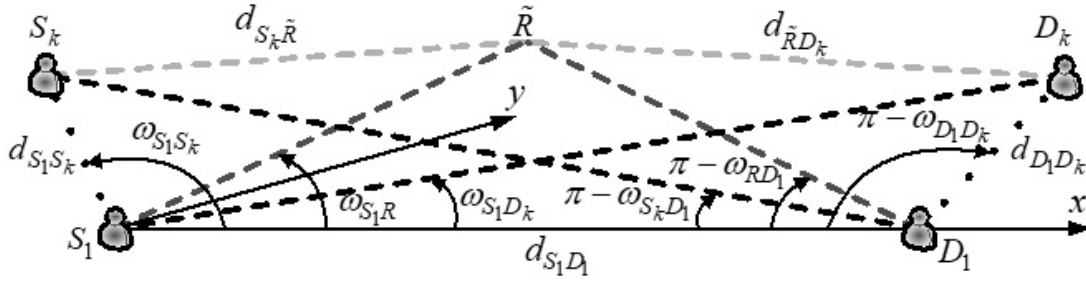
Fig. 3.8: Projection of the MS MD aerial platform aided communication system on the *xy* plane.

Applying the Pythagorian theorem to the triangle $S_k R \tilde{R}$ in Fig. 3.7 and the cosine law to the triangle $S_k S_1 \tilde{R}$ in Fig. 3.8, we obtain

$$d_{S_k R} = \left[\frac{H_R^2}{\sin^2 \beta_{S_1 R}} + d_{S_1 S_k}^2 - 2 \frac{H_R d_{S_1 S_k}}{\tan \beta_{S_1 R}} \cos\left(\omega_{S_1 S_k} - \omega_{S_1 R} \right) \right]^{1/2}. \qquad (3.28)$$

Moreover, applying the cosine law to the triangle $S_1 S_K D_1$ in Fig. 3.8, we obtain

$$\omega_{S_1 S_k} = \begin{cases} 0, & k = 1 \\ \arccos\left(\dfrac{d_{S_1 D_1}^2 + d_{S_1 S_k}^2 - d_{S_k D_1}^2}{2 d_{S_1 D_1} d_{S_1 S_k}} \right), & 2 \leq k \leq K, \end{cases} \qquad (3.29)$$

where $d_{S_1 D_1} - d_{S_1 S_k} \leq d_{S_k D_1} \leq d_{S_1 D_1} + d_{S_1 S_k}$. As shown in the Appendix, (3.28) can be written in an approximated form as a function of $\beta_{S_1 R}$ and $\omega_{S_1 R}$ as

$$d_{S_k R} \approx \left(\frac{H_R^2}{\sin^2 \beta_{S_1 R}} + d_{S_1 S_k}^2 - 2 \frac{H_R}{\tan \beta_{S_1 R}} d_{S_1 S_k} \sin \omega_{S_1 R} \right)^{1/2}. \qquad (3.30)$$

Assuming that $H_R \gg d_{S_1 S_k}$, e.g., the case of HAP-to-ground links, where the height of the relay is about 20 km [44], and using the approximate relation $\sqrt{1+x} \approx 1 + x/2$ for small x, (3.30) can be further approximated as

$$d_{S_k R} \approx \frac{H_R}{\sin \beta_{S_1 R}} - d_{S_1 S_k} \cos \beta_{S_1 R} \sin \omega_{S_1 R}. \tag{3.31}$$

Similarly, applying the Pythagorian theorem to the triangle $D_k R \tilde{R}$ in Fig. 3.7 and the cosine law to the triangle $S_1 \tilde{R} D_k$ in Fig. 3.8, we obtain

$$d_{RD_k} = \left[\frac{H_R^2}{\sin^2 \beta_{S_1 R}} + d_{S_1 D_k}^2 - 2 \frac{H_R d_{S_1 D_k}}{\tan \beta_{S_1 R}} \cos\left(\omega_{S_1 R} - \omega_{S_1 D_k} \right) \right]^{1/2}. \tag{3.32}$$

In addition, applying the cosine law to the triangle $S_1 D_1 D_k$ in Fig. 3.8, we obtain

$$\omega_{S_1 D_k} = \arccos\left(\frac{d_{S_1 D_k}^2 + d_{S_1 D_1}^2 - d_{D_1 D_k}^2}{2 d_{S_1 D_k} d_{S_1 D_1}} \right), \tag{3.33}$$

where $d_{S_1 D_k} - d_{S_1 D_1} \leq d_{D_1 D_k} \leq d_{S_1 D_k} + d_{S_1 D_1}$. As shown in the Appendix, (3.32) can be written in an approximated form as a function of $\beta_{S_1 R}$ and $\omega_{S_1 R}$ as

$$d_{RD_k} \approx \left[\frac{H_R^2}{\sin^2 \beta_{S_1 R}} + d_{S_1 D_k}^2 - 2 \frac{H_R}{\tan \beta_{S_1 R}} \left(d_{S_1 D_k} \cos \omega_{S_1 R} + d_{D_1 D_k} \sin \omega_{S_1 R} \right) \right]^{1/2}. \tag{3.34}$$

3.3.3 User Scheduling, Outage Probability, and Spectral Efficiency

Depending on the CSI obtained from the K SD pairs, the maximum SNR-based opportunistic scheduler on the relay can select and activate for communication the SD pair with the best E2E SNR among all the active SD pairs. Using (3.20), the SD pair selection will activate the k^*-th SD pair in each time slot according to:

$$k^* = \arg\max_{k \in U} \min \left\{ \gamma_{S_k, R}, \gamma_{R, D_k} \right\}. \tag{3.35}$$

The outage probability is defined as the probability that the SNR at the destination goes below a predetermined outage threshold γ, i.e., $P_{out} = \Pr\left[\gamma_{D_b} \leq \gamma \right]$, where

$\Pr[\cdot]$ is the probability operation and γ_{D_b} is the E2E SNR of the best SD pair. In this case, the communication system cannot achieve adequate reception. The outage probability can be obtained from the CDF of the E2E instantaneous SNR in (3.20) as $P_{out} = F_{\gamma_{D_b}}(\gamma)$, where $F_{\gamma_{D_b}}(\gamma)$ is the CDF of the best SD pair selected from K available SD pairs. Using the theory of order statistics [45] for i.n.i.d. γ_{D_k}, the outage probability can be expressed as

$$P_{out} = F_{\gamma_{D_b}}(\gamma) = \prod_{k=1}^{K} \Pr\left(\gamma_{D_k} \leq \gamma\right) = \prod_{k=1}^{K} F_{\gamma_{D_k}}(\gamma), \tag{3.36}$$

where

$$F_{\gamma_{D_k}}(\gamma) = 1 - \left[\left(1 - F_{\gamma_{S_kR}}(\gamma)\right)\left(1 - F_{\gamma_{RD_k}}(\gamma)\right)\right] \tag{3.37}$$

is the CDF of the instantaneous E2E SNR per symbol for the k-th pair. One observes that the system is not in outage provided that at least one of the links is not get in outage or, equivalently, the SNR of that link becomes larger than γ. The PDF of γ_{D_b} can be obtained by taking the derivative of the CDF in (20) with respect to γ as

$$f_{\gamma_{D_b}}(\gamma) = \sum_{k=1}^{K} f_{\gamma_{D_k}}(\gamma) \prod_{\substack{j=1 \\ j \neq k}}^{K} F_{\gamma_{D_j}}(\gamma), \tag{3.38}$$

where $f_{\gamma_{D_k}}(\gamma)$ is the PDF of the instantaneous E2E SNR per symbol at the k-th destination. In the high SNR regime, i.e., when $\{\overline{\gamma}_{S_kR}, \overline{\gamma}_{R,D_k}\} \to \infty$, $F_{\gamma_{D_k}}(\gamma)$ can be written in an approximation form as [12]

$$F_{\gamma_{D_k}}(\gamma) \approx F_{\gamma_{S_kR}}(\gamma) + F_{\gamma_{RD_k}}(\gamma). \tag{3.39}$$

Using (3.23), (3.24), (3.27), (3.39), and the approximate relation $\exp(-x) \approx 1 - x$ for small x, the outage probability can be written as [12]

$$F_{\gamma_{D_k}}(\gamma) \approx A \frac{d_{S_kR}^{2m_{SR}\xi}}{P_S^{m_{SR}\xi}} + B \frac{d_{RD_k}^{2m_{RD}\xi}}{P_R^{m_{RD}\xi}}, \tag{3.40}$$

where

$$A = \frac{\left[m_{SR} \mu \gamma N_o \left(\frac{4\pi}{\lambda} \right)^2 \right]^{m_{SR}\xi}}{\Gamma\left(m_{SR}\xi + 1 \right)},$$

(3.41)

$$B = \frac{\left[m_{RD} \mu \gamma N_o \left(\frac{4\pi}{\lambda} \right)^2 \right]^{m_{RD}\xi}}{\Gamma\left(m_{RD}\xi + 1 \right)}.$$

(3.42)

Note that the approximate closed-form expression in (3.40) is valid in a broad range of SNR [12]. From (3.40)-(3.42) it is obvious that P_{out} is not only related with the system geometry, but also depends on the source and relay transmit power, the number of antennas, and the channel fading in each link.

It is assumed that the discrete-rate adaptive modulator chooses the highest bit-rate modulation scheme for that user that satisfies a target BER. In this section, a M-ary adaptive modulation selection scheme is performed by dividing the entire SNR region into $N+1$ fading regions defined by SNR thresholds $0 < a_1 < ...a_n < a_{n+1} = \infty$, where $n \in \{1,2,...,N\}$ is a positive integer and N designates the N-mode modulations with constellation sizes $M_n = 2^{\beta_n}$, where β_n denotes the bits/symbol [20]. The lower part of each SNR region is the smallest SNR required to achieve the target BER. For the signals whose SNR values are smaller than the smallest threshold a_1 that corresponds to BPSK modulation and $\beta_n = 1$, there will be no transmission, i.e. outage exists. However, for signals whose SNRs are higher than a_N, the highest modulation mode will be used. The threshold values a_n act as switching levels and can be calculated for a certain BER$_t$ as follows [46]:

$$a_n = \begin{cases} \frac{1}{2} \left[Q^{-1}\left(BER_t \right) \right]^2, \, n = 1 \\ \frac{-(2^n - 1)}{1.5} \ln\left(5BER_t \right), \, 2 \leq n \leq N. \\ +\infty, \, n = N+1 \end{cases}$$

(3.43)

where $Q^{-1}(\cdot)$ denotes the inverse Gaussian Q-function. The achievable average spectral efficiency (SE) in bits/s/Hz is defined as [47]

$$\overline{SE} = \sum_{n=1}^{N} \beta_n P_n,\tag{3.44}$$

where $P_n = \int_{a_n}^{a_{n+1}} f_{\gamma_{D_b}}(\gamma)d\gamma = \left[F_{\gamma_{D_b}}(a_{n+1}) - F_{\gamma_{D_b}}(a_n) \right]$ is the probability of the modulation mode selection. At high SNR values, $a_n \leq \gamma \leq a_{n+1} = \infty$, and hence $F_{\gamma_{D_b}}(a_{N+1}) = 1$. Then, at high SNRs, (3.44) can be expressed in a closed form as

$$\overline{SE} = \sum_{n=1}^{N} \beta_n \left[F_{\gamma_{D_b}}(a_{n+1}) - F_{\gamma_{D_b}}(a_n) \right],\tag{3.45}$$

where $F_{\gamma_{D_b}}(a_n)$ and $F_{\gamma_{D_b}}(a_{n+1})$ can be obtained using (3.40)-(3.42) and replacing γ by a_n and a_{n+1}, respectively.

3.3.4 Optimization Problems

An important design parameter is to determine the optimal position of the aerial relay platform that will minimize the outage probability. Although it is not trivial to find the optimal position due to the irregular-shaped propagation area, the approximations derived in the Appendix simplify the optimization procedure. This section studies optimization problems and derives solutions.

In order to find the optimal position of the relay one should estimate both the optimal azimuth angle and elevation angle of the relay with respect to a reference point. Let the coordinate origin S_1 be the reference point, $P_{out} = f\left(\omega_{S_1 R}, \beta_{S_1 R}\right)$ be the cost function, and $\omega_{S_1 R,opt}$, $\beta_{S_1 R,opt}$ be the critical angles, which minimize the cost function. Based on Appendix and considering predetermined power allocation $\left(P_S / N_o, P_R / N_o\right)$ and fixed values of H_R, $\left\{d_{S_1 S_k}\right\}$, $\left\{d_{S_1 D_k}\right\}$, the problem of finding the optimal azimuth angle of the relay with respect to S_1 can be stated as

$$\omega^{*}_{S_1R} = \arg \min_{\omega_{S_1R}} P_{out}$$

$$\text{subject to: } 0 < \omega_{S_1R} < \pi/2. \tag{3.46}$$

Using (3.36), the second derivative of P_{out} with respect to ω_{S_1R} can be written as

$$\frac{\partial^2 P_{out}}{\partial \omega^2_{S_1R}} = \sum_{j_1+j_2+\dots+j_K=2} \binom{2}{j_1, j_2, \dots, j_K} \left(\prod_{k=1}^{K} F_{\gamma_{D_k}}^{(j_k)}\left(\omega_{S_1R}\right) \right). \tag{3.47}$$

Since $\partial^2 P_{out}/\partial \omega^2_{S_1R} > 0$, the objective function is a strictly convex function of $\omega_{S_1R} \in (0, \pi/2)$. The optimal relay location is the root of the first derivative of P_{out} with respect to ω_{S_1R}, which can be obtained as follows

$$\frac{\partial P_{out}}{\partial \omega_{S_1R}} = \sum_{k=1}^{K} \frac{\partial F_{\gamma_{D_k}}\left(\omega_{S_1R}\right)}{\partial \omega_{S_1R}} \prod_{\substack{j=1 \\ j \neq k}}^{K} F_{\gamma_{D_k}}\left(\omega_{S_1R}\right). \tag{3.48}$$

Since $F_{\gamma_{D_k}}\left(\omega_{S_1R}\right) \neq 0 \ \forall \omega_{S_1R} \in (0, \pi/2)$, the optimal relay location in the azimuth domain is the root of $\sum_{k=1}^{K} \partial F_{\gamma_{D_k}}\left(\omega_{S_1R}\right) / \partial \omega_{S_1R} = 0$. Using (3.40)-(3.42), we obtain

$$\frac{\partial F_{\gamma_{D_k}}\left(\omega_{S_1R}\right)}{\partial \omega_{S_1R}} \approx$$

$$\frac{2Bm_{RD}\xi H_R \left(d_{S_1D_k} \sin\omega_{S_1R} - d_{D_1D_k} \cos\omega_{S_1R}\right)}{P_R^{m_{RD}\xi} \tan\beta_{S_1R}}$$

$$\times \left[\frac{H_R^2}{\sin^2\beta_{S_1R}} + d_{S_1D_k}^2 - 2\frac{H_R}{\tan\beta_{S_1R}} \left(d_{S_1D_k} \cos\omega_{S_1R} - d_{D_1D_k} \sin\omega_{S_1R}\right) \right]^{m_{RD}\xi-1}$$

$$- \frac{2Am_{SR}\xi H_R d_{S_1S_k} \cos\omega_{S_1R}}{P_S^{m_{SR}\xi} \tan\beta_{S_1R}}$$

$$\times \left(\frac{H_R^2}{\sin^2\beta_{S_1R}} + d_{S_1S_k}^2 - 2\frac{H_R}{\tan\beta_{S_1R}} d_{S_1S_k} \sin\omega_{S_1R} \right)^{m_{SR}\xi-1}. \tag{3.49}$$

It is noted that using numerical solving techniques, numerical values for ω_{S_1R} can be obtained. However, in order to derive closed-form solutions, the special case of single antennas, i.e., $L=1$, and symmetric Rayleigh/Rayleigh fading in all links, i.e.,

$m_{SR} = m_{RD} = 1$, is studied, which results to $A = B = \gamma N_o R_c (4\pi / \lambda)^2$. Then, (3.49) becomes

$$\frac{\partial F_{\gamma_{D_k}}\left(\omega_{S_1R}\right)}{\partial \omega_{S_1R}} \approx \frac{2H_R \gamma N_o R_c}{P_S P_R \tan \beta_{S_1R}} \left(\frac{4\pi}{\lambda}\right)^2 \left[d_{S_1D_k} P_S \sin \omega_{S_1R} - \left(d_{D_1D_k} P_S + d_{S_1S_k} P_R \right) \cos \omega_{S_1R} \right]. \quad (3.50)$$

Using (3.50), $\omega_{S_1R,opt}$ can be calculated as

$$\omega_{S_1R,opt} \approx \arctan\left[\frac{\left(P_R \sum_{k=1}^{K} d_{S_1S_k} \right) + \left(P_S \sum_{k=1}^{K} d_{D_1D_k} \right)}{P_S \sum_{k=1}^{K} d_{S_1D_k}} \right]. \quad (3.51)$$

Considering equal power allocation, i.e., $P_S = P_R$, (3.51) becomes

$$\omega_{S_1R,opt} \approx \arctan\left[\frac{\sum_{k=1}^{K} \left(d_{S_1S_k} + d_{D_1D_k} \right)}{\sum_{k=1}^{K} d_{S_1D_k}} \right]. \quad (3.52)$$

Since $\left\{ d_{S_1S_k}, d_{D_1D_k} \right\} \ll d_{S_1D_k}$, $\omega_{S_1R,opt}$ is a small angle in this scenario. Moreover, using (3.51) for the special case of $K = 1$, i.e., one SD pair, we obtain $\omega_{S_1R,opt} = 0°$. Then, S_1, R, and D_1 are collinear and are positioned across the x-axis. The simplified results of single-user single-antenna systems agree with the results in [19].

Similarly, based on Appendix, the problem of finding the optimal elevation angle of the relay with respect to S_1 can be stated as

$$\beta_{S_1R}^* = \arg \min_{\beta_{S_1R}} P_{out}$$

subject to: $\arctan\left(H_R / \max\left\{ d_{S_1D_k} \right\} \right) < \beta_{S_1R,opt} < \pi / 2 \quad (3.53)$

and the optimal relay location is the root of $\sum_{k=1}^{K} \partial F_{\gamma_{D_k}}\left(\beta_{S_1 R}\right) / \partial \beta_{S_1 R} = 0$. Using (3.40)-

(3.42), $\partial F_{\gamma_{D_k}}\left(\beta_{S_1 R}\right) / \partial \beta_{S_1 R}$ can be approximated as

$$
\frac{\partial F_{\gamma_{D_k}}\left(\beta_{S_1 R}\right)}{\partial \beta_{S_1 R}} \approx
$$

$$
\frac{2 B m_{RD} \xi H_R \left(d_{S_1 D_k} \cos \omega_{S_1 R} + d_{D_1 D_k} \sin \omega_{S_1 R} - \dfrac{H_R}{\tan \beta_{S_1 R}} \right)}{P_R^{m_{RD} \xi} \sin^2 \beta_{S_1 R}}
$$

$$
\times \left[\frac{H_R^2}{\sin^2 \beta_{S_1 R}} + d_{S_1 D_k}^2 - 2 \frac{H_R}{\tan \beta_{S_1 R}} \left(d_{S_1 D_k} \cos \omega_{S_1 R} - d_{D_1 D_k} \sin \omega_{S_1 R} \right) \right]^{m_{RD} \xi - 1}
$$

$$
+ \frac{2 A m_{SR} \xi H_R \left(d_{S_1 S_k} \sin \omega_{S_1 R} - \dfrac{H_R}{\tan \beta_{S_1 R}} \right)}{P_S^{m_{SR} \xi} \sin^2 \beta_{S_1 R}}
$$

$$
\times \left(\frac{H_R^2}{\sin^2 \beta_{S_1 R}} + d_{S_1 S_k}^2 - 2 \frac{H_R}{\tan \beta_{S_1 R}} d_{S_1 S_k} \sin \omega_{S_1 R} \right)^{m_{SR} \xi - 1}. \tag{3.54}
$$

For the special case of symmetric Rayleigh/Rayleigh fading in all links and single antennas, (3.54) becomes

$$
\frac{\partial F_{\gamma_{D_k}}\left(\beta_{S_1 R}\right)}{\partial \beta_{S_1 R}} \approx \frac{2 H_R \gamma N_o R_c}{P_S P_R \sin^2 \beta_{S_1 R}} \left(\frac{4\pi}{\lambda} \right)^2 \left[d_{S_1 D_k} P_S \cos \omega_{S_1 R} - \frac{H_R P_t}{\tan \beta_{S_1 R}} + \left(d_{S_1 S_k} P_R + d_{D_1 D_k} P_S \right) \sin \omega_{S_1 R} \right].
$$
$$
\tag{3.55}
$$

Using (3.55), $\beta_{S_1 R, opt}$ can be calculated as

$$
\beta_{S_1 R, opt} \approx \arctan \left[\frac{K H_R P_T}{\cos \omega_{S_1 R} P_S \displaystyle\sum_{k=1}^{K} d_{S_1 D_k} + \sin \omega_{S_1 R} \left(P_R \displaystyle\sum_{k=1}^{K} d_{S_1 S_k} + P_S \displaystyle\sum_{k=1}^{K} d_{D_1 D_k} \right)} \right], \tag{3.56}
$$

where $P_T = P_S + P_R$ is the total power. Moreover, using (3.51), (3.56) becomes

$$\beta_{S_1R,opt} \approx \arctan\left(\frac{KH_R}{\displaystyle\sum_{k=1}^{K} d_{S_1D_k}} \frac{P_T}{P_S} \cos\omega_{S_1R,opt}\right).$$ (3.57)

It is noted that using (3.57), the joint optimization of the azimuth and elevation angle, i.e., the optimization of the location of the relay, is obtained. Considering equal power allocation, (3.57) yields

$$\beta_{S_1R,opt} \approx \arctan\left(\frac{2KH_R}{\displaystyle\sum_{k=1}^{K} d_{S_1D_k}}\right).$$ (3.58)

Furthermore, using the approximate expressions in (3.52) and (3.58), we obtain $d_{S_kR} \approx d_{RD_k}$. Hence, observing (3.40), one concludes that $\omega_{S_1R,opt}$ and $\beta_{S_1R,opt}$ approximately correspond to the root of $\displaystyle\sum_{k=1}^{K} \partial F_{\gamma_{D_k}}\left(\omega_{S_1R}\right)/\partial\omega_{S_1R} = 0$ and $\displaystyle\sum_{k=1}^{K} \partial F_{\gamma_{D_k}}\left(\beta_{S_1R}\right)/\partial\beta_{S_1R} = 0$, respectively, for the generalized scenario of symmetric fading in all links, i.e., $m_{SR} = m_{RD}$, L antennas, and equal power allocation.

To formulate the third optimization problem, we consider a predetermined relay location with respect to S_1, i.e., specific ω_{S_1R} and β_{S_1R}. Thus, the problem of finding the optimal power allocation can be stated as follows

$$P_S^*, P_R^* = \arg\min_{P_S, P_R} P_{out}$$

$$\text{subject to: } P_S + P_R = P_T \text{ and } \{P_S, P_R\} > 0.$$ (3.59)

One can easily show that $\partial^2 P_{out}/\partial\omega_{S_1R}^2 > 0$ and hence the objective function is a strictly convex function of $P_S \in (0, P_T)$. The optimal source transmit power P_S is the root of $\displaystyle\sum_{k=1}^{K} \partial F_{\gamma_{D_k}}\left(P_S\right)/\partial P_S = 0$. Using (3.40)-(3.42), we obtain

$$\frac{\partial F_{\gamma_{D_k}}(P_S)}{\partial P_S} \approx \frac{Bm_{RD}\xi\left(\dfrac{d_{RD_k}}{P_T - P_S}\right)^{m_{RD}\xi}}{P_T - P_S} - \frac{Am_{SR}\xi\left(\dfrac{d_{S_kR}}{P_S}\right)^{m_{SR}\xi}}{P_S}. \tag{3.60}$$

For the special case of single antennas and symmetric Rayleigh/Rayleigh fading in all links, (3.60) becomes

$$\frac{\partial F_{\gamma_{D_k}}(P_S)}{\partial P_S} \approx \gamma N_o R_c \left(\frac{4\pi}{\lambda}\right)^2 \left[\frac{d_{RD_k}}{(P_T - P_S)^2} - \frac{d_{S_kR}}{P_S^2}\right]. \tag{3.61}$$

Using (3.61), $P_{S,opt}$ and $P_{R,opt}$ can be derived, respectively, as

$$P_{S,opt} \approx P_T \frac{\rho - \sqrt{\rho}}{\rho - 1}, \tag{3.62}$$

$$P_{R,opt} \approx P_T \frac{\sqrt{\rho} - 1}{\rho - 1}, \tag{3.63}$$

where $\rho = \left(\sum_{k=1}^{K} d_{S_kR}\right) / \left(\sum_{k=1}^{K} d_{RD_k}\right)$. Using (3.52) and (3.58), for which equal power allocation is considered, we obtain $d_{S_kR} \approx d_{RD_k}$ and $\rho \approx 1$. Then, using (3.62) and applying the L'Hôpital's rule, it follows that $P_{S,opt} \approx P_T \lim_{\rho \to 1}\left(1 - \frac{1}{2\sqrt{\rho}}\right) = 0.5P_T$, which confirms the equal power allocation. This is the case where the relay location and the power allocation are jointly optimized at the same time to further improve the performance, the fading in all links is symmetric, i.e., $m_{SR} = m_{RD}$, and L antennas are used. For ease of reference, Table 3.1 summarizes the guidelines for the optimization of the relay location and the power allocation depending on the channel fading conditions.

Table 3.1

Guidelines for the Optimization of the Relay Location and the Power Allocation

	$m_{SR} = m_{RD} = 1$		$m_{SR} = m_{RD}$		$m_{SR} \neq m_{RD}$
	$P_S \neq P_R$	$P_S = P_R$	$P_S \neq P_R$	$P_S = P_R$	
$\omega_{S_1 R, opt}$	Use (3.49) for $L > 1$ and (3.51) for $L = 1$	Use (3.52)	Use (3.49)	Use (3.52)	Use (3.49)
$\beta_{S_1 R, opt}$	Use (3.54) for $L > 1$ and (3.57) for $L = 1$	Use (3.58)	Use (3.54)	Use (3.58)	Use (3.54)
$P_{S, opt}$	Use (3.60) for $L > 1$ and (3.62) for $L = 1$	$P_T / 2$	Use (3.60)	$P_T / 2$	Use (3.60)

3.3.5 Numerical Results

This section quantifies some of our analytical and closed-form findings and investigates the outage performance of the MS MD aerial relay platform system with opportunistic scheduling over MIMO Nakagami-*m* fading channels. It is considered that the carrier frequency is equal to 2.1 GHz [48] and hence $\lambda \approx 0.14$ m. It is also considered that $H_R = 20$ km, $\gamma = 0$ dB, $a = 2$, and $R_c = 1$. Unless indicated otherwise, the values of the other system parameters used to obtain the curves in Figs. 3.9-3.11 and the results in Table 3.3 are presented in Table 3.2.

Fig. 3.9 depicts the outage probability, as a function of the source transmit SNR for equal power allocation and different number of SD pairs and antenna elements.

Moreover, the outage probability obtained using the exact mathematical expressions in (3.28) and (3.32) is compared with the ones obtained using the approximate expressions in (3.30) and (3.34). To clearly present the impact of these parameters on the outage probability and indicate the minimum achieved outage, the worst case of symmetric Rayleigh/Rayleigh channel fading is considered, i.e., $m_{SR} = m_{RD} = 1$. However, in many practical situations, a LoS component exists. Note that the non-optimized values of $\omega_{S_1R} = 30°$ and $\beta_{S_1R} = 60°$ are used. One observes that the approximations are valid and, as expected, the outage probability substantially decreases, as L increases. Besides, a significant performance improvement can be achieved, as the number of K increases. Nevertheless, the number of antennas is more influential than the number of SD pairs.

Fig. 3.10 shows the outage probability as a function of the azimuth angle ω_{S_1R} and elevation angle β_{S_1R} of the relay. It is considered that the Rician factor in all the links is equal to 3 dB for the Fig. 3.10a, which corresponds to $m_{SR} = m_{RD} = 1.8$. Besides, in Fig. 3.10b, we consider that $m_{SR} = 1$ and $m_{RD} = 5$. Although ω_{S_1R} and β_{S_1R} effectively control the outage performance, there exists a particular $\omega_{S_1R,opt} - \beta_{S_1R,opt}$ pair that minimizes the outage probability. Using (3.52) and (3.58), we obtain $\omega_{S_1R,opt} \approx 3°$ and $\beta_{S_1R,opt} \approx 45°$, respectively, whereas using (3.49) and (3.54) yields $\omega_{S_1R,opt} \approx 89°$ and $\beta_{S_1R,opt} \approx 85°$, respectively. Hence, we confirm the utility of the optimization recommendations.

Figs. 3.11 demonstrates the outage probability, as a function of the source transmit SNR for both the optimal and the non-optimal relay location and power allocation and symmetric Rayleigh/Rayleigh channel fading. It is obvious that the optimized system outperforms the non-optimized one. More specifically, the minimum outage is achieved, provided that the relay location and the power allocation are jointly optimized. Fig. 3.11 also indicates that the proper relay location is more requisite than the power allocation and hence, a communication system designer should consider the geometric/physical characteristics of the

system. Note that the azimuth angle of the relay slightly affects the outage performance, which in turns suggests that the relay may shift from the optimal location and have a circular trajectory with a negligible effect on the outage.

Finally, Table 3.3 handles the joint optimization of the relay location and power allocation and demonstrates the range of optimal values of ω_{S_1R}, β_{S_1R}, and P_S as function of the Nakagami-m m_{SR} and m_{RD} parameters. These parameters act actually as weights and control the effect of the system geometry and the power allocation on the outage performance. As m_{SR} $\left(m_{RD} \right)$ increases with respect to $m_{RD}\left(m_{SR} \right)$, which is considered constant and equal to 1, ω_{S_1R} moderately decreases (increases) and tends to $0°\left(90°\right)$. Besides, as $m_{SR}\left(m_{RD} \right)$ increases, β_{S_1R} also drastically decreases (increases) and the relay moves closer to the destinations (sources), while less (more) source transmit power is needed. In particular, better first (second) hop performance is observed and the overall system performance is more dependent on the second (first) hop. Thus, allocating more power to the relay (sources) improves the outage performance.
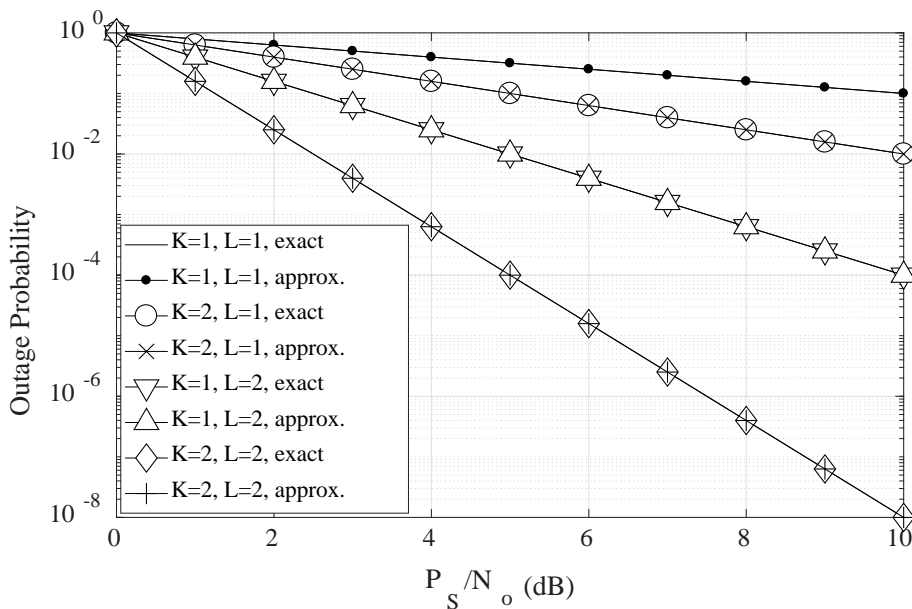
Fig. 3.9: Outage probability in terms of the source transmit SNR for symmetric Rayleigh/Rayleigh channel fading and different number of antennas and SD pairs.
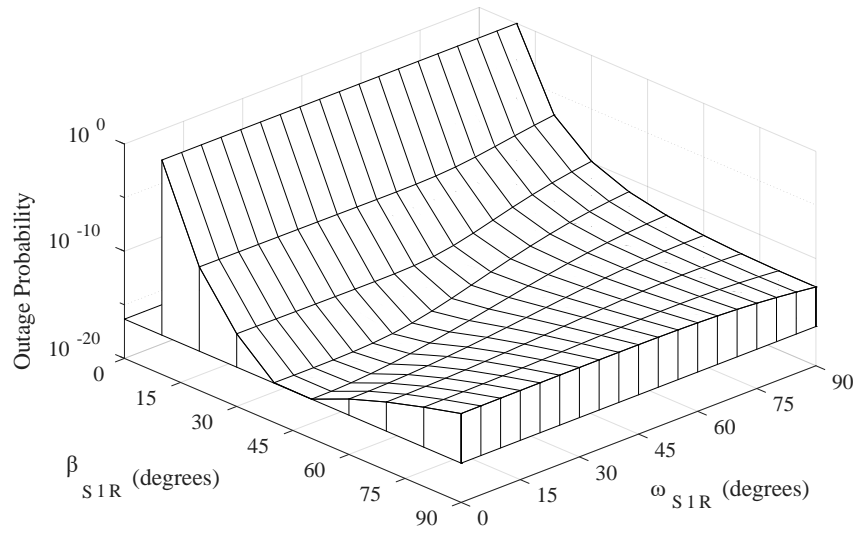
(a)
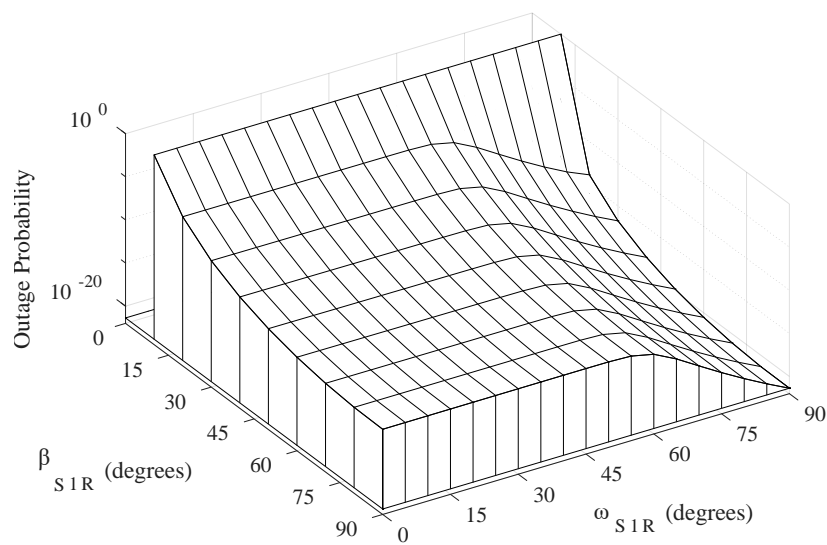
(b)

Fig. 3.10: Outage probability as a function of the azimuth and elevation angle of the relay for (a) symmetric Rician/Rician and (b) assymetric Rayleigh/Rician channel fading.

Table 3.2
Values of System Parameters Used in Figs. 3.9-3.11 and Table 3.3

Parameter	Fig. 3.9	Fig. 3.10a	Fig. 3.10b	Fig. 3.11	Table 3.3
K (# SD Pairs)	1-2	2			
L (# antennas)	1-2	2			
$d_{S_1 S_2}$ (km)	2				
$d_{S_1 D_1}$ (km)	60	40		60	60
$d_{S_1 D_2}$ (km)	61	41		61	61
$d_{D_1 D_2}$ (km)	2				
m_{SR}	1	1.8	1		Varies
m_{RD}	1	1.8	5	1	Varies
P_S / N_o (dB)	0 to 10	5		0 to 10	Varies
P_R / N_o (dB)	0 to 10	5		-3 to 7, non-opt. / 0 to 10, opt.	Varies
$\omega_{S_1 R}$ $(^\circ)$	30, non-opt.	Varies		30, non-opt. / 2, opt.	Varies
$\beta_{S_1 R}$ $(^\circ)$	60, non-opt.	Varies		60, non-opt. / 34, Opt.	Varies
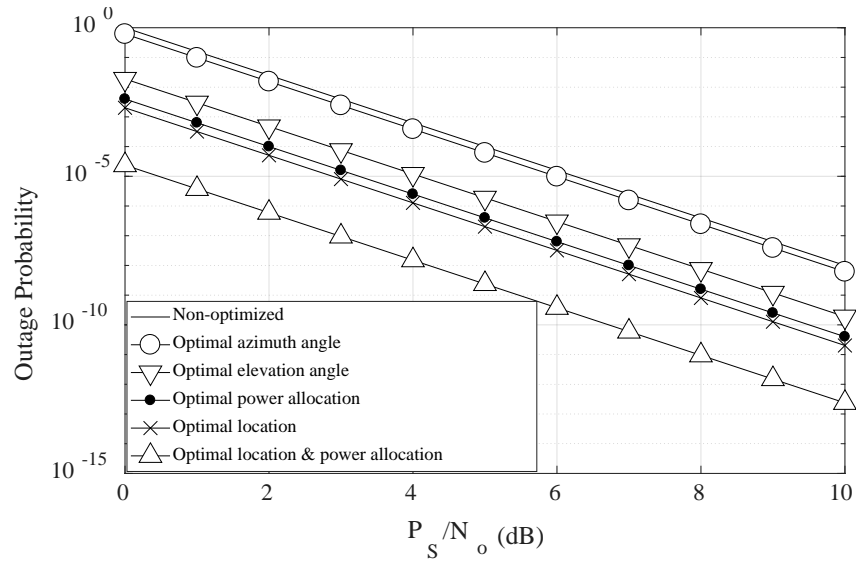
Fig. 3.11: Outage probability of the non-optimized and optimized system in terms of the source transmit SNR for symmetric Rayleigh/Rayleigh fading.

Table 3.3

Variation of the Jointly Optimized System Parameters Depending the Channel Fading Conditions

m_{SR}	1	1.5	2	2.5	3	3.5	4	4.5	5	5.5	6	6.5	7	7.5	8
$\omega_{S_1R,opt}\left(^{\circ}\right)$	2.5	1.9	1.6	1.5	1.5	1.4	1.4	1.4	1.4	1.4	1.4	1.37	1.36	1.36	1.36
$\beta_{S_1R,opt}\left(^{\circ}\right)$	44.9	37.2	33.8	32.0	30.9	30.2	29.8	29.4	29.2	29.0	28.8	28.7	28.6	28.5	28.4
$P_{S,opt}/P_T$	0.5	0.49	0.47	0.44	0.42	0.39	0.37	0.36	0.34	0.33	0.32	0.31	0.30	0.29	0.29

m_{RD}	1	1.5	2	2.5	3	3.5	4	4.5	5	5.5	6	6.5	7	7.5	8
$\omega_{S_1R,opt}\left(^{\circ}\right)$	2.5	3.6	4.8	6.1	7.4	8.6	9.7	10.8	11.8	12.9	13.6	14.4	15.1	15.5	16.3
$\beta_{S_1R,opt}\left(^{\circ}\right)$	44.9	55.5	63.0	68.1	71.5	73.9	75.7	76.9	78.0	78.8	79.4	80.1	80.7	81.0	81.1
$P_{S,opt}/P_T$	0.5	0.51	0.53	0.56	0.58	0.61	0.63	0.64	0.66	0.67	0.68	0.69	0.70	0.71	0.71

REFERENCES

[1] R. Xu, F.C.M. Lau, "Performance analysis for MIMO systems using zero forcing detector over fading channels," *Communications, IEE Proceedings,* vol. 153, no. 1, pp.74-80, 2 Feb. 2006.

[2] D. Christopoulos, J. Arnau, S. Chatzinotas, C. Mosquera, and B. Ottersten, "MMSE performance analysis of generalized multibeam satellite channels," *Communications Letters, IEEE ,* vol. 17, no. 7, pp. 1332–1335, 2013.

[3] A. Al-Hourani, S. Kandeepan, and S. Lardner, "Optimal LAP altitude for maximum coverage," *IEEE Wireless Commun. Lett.*, vol. 3, no. 6, pp. 569–572, Dec. 2014.

[4] M. Alzenad, A. El-Keyi, F. Lagum, and H. Yanikomeroglu, "3-D placement of an unmanned aerial vehicle base station (UAV-BS) for energy efficient maximal coverage," *IEEE Wireless Commun. Lett.*, vol. 6, no. 4, pp. 434–437, Aug. 2017.

[5] J. Lyu, Y. Zeng, R. Zhang, and T. J. Lim, "Placement optimization of UAV-mounted mobile base stations," *IEEE Commun. Lett.*, vol. 21, no. 3, pp. 604–607, Mar. 2017.

[6] R. Yaliniz, A. El-Keyi, and H. Yanikomeroglu, "Efficient 3-D placement of an aerial base station in next generation cellular networks," in *Proc. IEEE Int. Conf. Commun. (ICC)*, Kuala Lumpur, Malaysia, May 2016.

[7] F. Jiang and A. L. Swindlehurst, "Optimization of UAV Heading for the Ground-to-Air Uplink," *IEEE Journal on Selected Areas in Communications*, vol. 30, no. 5, pp. 993-1005, Jun. 2012.

[8] O. Jian, Z. Yi, L. Min, and L. Jia, "Optimization of beamforming and path planning for UAV-assisted wireless relay networks," *Chinese Journal of Aeronautics*, vol. 27, no. 2, pp. 313-320, 2014.

[9] H. He, S. Zhang, Y. Zeng, and R. Zhang, "Joint altitude and beamwidth optimization for UAV-enabled multiuser communications," *IEEE Commun. Letters*. vol. 22, no. 2, pp. 344-347, Feb. 2018.

[10] M. M. Azari, F. Rosas, K. C. Chen, and S. Pollin, "Optimal UAV positioning for terrestrial-aerial communication in presence of fading," in *Proc. IEEE Global Communications Conference (GLOBECOM) 2016*, pp. 1-7, 2016.

[11] J. Lyu, Y. Zeng, and R. Zhang, "Cyclical multiple access in UAV-aided communications: A throughput-delay tradeoff," *IEEE Wireless Commun.* Lett., vol. 5, no. 6, pp. 600-603, Dec. 2016.

[12] S. S. Ikki, "Optimisation study of power allocation and relay location for amplify-and-forward systems over Nakagami-m fading channels," *Emerging Telecommunications Technologies*, vol. 25, no. 3, pp. 334-342, Mar. 2014.

[13] H. Wang, G. Ren, J. Chen, G. Ding and Y. Yang, "Unmanned Aerial Vehicle-Aided Communications: Joint Transmit Power and Trajectory Optimization," *IEEE Wireless Communications Letters*.

[14] F. Ono, H. Ochiai, and R. Miura, "A wireless relay network based on unmanned aircraft system with rate optimization," *IEEE Trans. Wireless Commun.*, vol. 15, no. 11, pp. 7699-7708, Nov. 2016.

[15] E. Larsen, L. Landmark, and O. Kure, "Optimal UAV relay positions in multi-rate networks," in *Proc. Wireless Days*, Porto, Portugal, pp. 8-14, Mar. 2017.

[16] Y. Zeng, R. Zhang, and T. J. Lim, "Throughput maximization for UAV-enabled mobile relaying systems," *IEEE Trans. Commun.*, vol. 64, no. 12, pp. 4983-4996, Dec. 2016.

[17] E. T. Michailidis, N. Nomikos, P. Bithas, D. Vouyioukas, and A. G. Kanatas, "Optimal Relay Location and Opportunistic User-Scheduling for Stratospheric Communications," in *Proc. 10th International Conference on Advances in Satellite and Space Communications (SPACOMM) 2018*, Athens, Greece, 22-26 Apr. 2018.

[18] Y. Chen, W. Feng and G. Zheng, "Optimum Placement of UAV as Relays," *IEEE Communications Letters*, vol. 22, no. 2, pp. 248-251, Feb. 2018.

[19] S. Zhang, H. Zhang, Q. He, K. Bian and L. Song, "Joint Trajectory and Power Optimization for UAV Relay Networks," *IEEE Communications Letters*, vol. 22, no. 1, pp. 161-164, Jan. 2018.

[20] M. Torabi, D. Haccoun, and W. Ajib, "Analysis of the performance of multiuser MIMO systems with user scheduling over Nakagami-*m* fading channels," *Physical Communication*, vol. 3, no. 3, pp. 168-179, Sep. 2010.

[21] L. Yang and Q. T. Zhang, "Performance Analysis of MIMO Relay Wireless Networks With Orthogonal STBC," *IEEE Transactions on Vehicular Technology*, vol. 59, no. 7, pp. 3668-3674, Sep. 2010.

[22] P. Zhan, K. Yu and A. L. Swindlehurst, "Wireless Relay Communications with Unmanned Aerial Vehicles: Performance and Optimization," *IEEE Transactions on Aerospace and Electronic Systems*, vol. 47, no. 3, pp. 2068-2085, Jul. 2011.

[23] X. Liang, S. Jin, K.-K. Wong, T. Hong, and H. Zhu, "Multi-pair massive MIMO relay networks: power scaling laws and user scheduling strategy," IET Communications, vol. 11, no. 10, pp. 1619-1625, Jul. 2017.

[24] A. Asadi and V. Mancuso, "A Survey on Opportunistic Scheduling in Wireless Communications," *IEEE Communications Surveys & Tutorials*, vol. 15, no. 4, pp. 1671-1688, 2013.

[25] G. Zheng, S. Chatzinotas, and B. Otterstern. Generic "Optimization of Linear Precoding in Multibeam Satellite Systems", *IEEE Transactions on Wireless Communications*, Jun. 2012.

[26] D. Christopoulos, S. Chatzinotas, G. Zheng, J. Grotz, and B. Ottersten, "Linear and non-linear techniques for multibeam joint processing in satellite communications," *EURASIP J. on Wirel. Commun. and Networking 2012*, 2012:162.

[27] M. A. Diaz, N. Courville, C. Mosquera, G. Liva, G.E. Corazza, "Non-Linear Interference Mitigation for Broadband Multimedia Satellite Systems," in Proc. International Workshop on Satellite and Space Communications (IWSSC) 2007, pp. 61-65, 13-14 Sep. 2007.

[28] D. Christopoulos, S. Chatzinotas, M. Matthaiou, and B. Ottersten, "Capacity analysis of multibeam joint decoding over composite satellite channels," in *Proc. Fifth Asilomar Conference on Signals, Systems and Computers (ASILOMAR)*, pp. 1795-1799, 2011.

[29] C. Loo and J. S. Butterworth, "Land mobile satellite channel measurements and modeling," in *Proceedings of the IEEE*, vol. 86, no. 7, pp. 1442-1463, Jul. 1998.

[30] N. Letzepis and A. Grant, "Capacity of the multiple spot beam satellite channel with Rician fading," *IEEE Trans. Inf. Theory*, vol. 54, no. 11, pp. 5210-5222, Nov. 2008.

[31] Y. S. Cho, J. Kim, W. Y. Yang, and C. G. Kang, *MIMO-OFDM Wireless Communications with Matlab*, Wiley, 2010.

[32] M. Jing, Z. Ying, S. Xin, and Y. Yan, "On capacity of wireless ad hoc networks with MIMO MMSE receivers," *IEEE Trans. on Wireless Communications*, vol. 7, no. 12, pp. 5493-5503, Dec. 2008.

[33] R. Xu, F.C.M. Lau, "Performance analysis for MIMO systems using zero forcing detector over fading channels," Communications, *IEE Proceedings*, vol. 153, no. 1, pp.74-80, 2 Feb. 2006.

[34] E. G. Larsson and P. Stoica, *Space-Time Block Coding for Wireless Communications*, New York: Cambridge Univ. Press, 2003.

[35] H. Shin and J. H. Lee, "Performance analysis of space-time block codes over keyhole Nakagami-m fading channels," *IEEE Transactions on Vehicular Technology*, vol. 53, no. 2, pp. 351-362, Mar. 2004.

[36] W. Khawaja, et al., "A Survey of Air-to-Ground Propagation Channel Modeling for Unmanned Aerial Vehicles," arXiv:1801.01656v1, 2018.

[37] R. Amorim, P. Mogensen, T. Sorensen, I. Z. Kovacs, and J. Wigard, "Pathloss Measurements and Modeling for UAVs Connected to Cellular Networks," in *Proc. IEEE 85th Vehicular Technology Conference (VTC Spring) 2017*, Sydney, NSW, pp. 1-6, 2017.

[38] T. Rappaport, *Wireless Communications: Principles and Practice*, 2nd ed. Upper Saddle River, NJ: Prentice Hall PTR, 2002.

[39] M. Nakagami, *The m-distribution – A general formula of intensity distribution of rapid fading*, W.C. Hoffman (Ed.), Statistical Methods in Radio Wave Propagation, Pergamon, Elmsford, NY, 1960.

[40] I. S. Gradshteyn and I. M. Ryzhik, *Table of Integrals, Series, and Products*, 6th ed. New York: Academic, 2000.

[41] Iskandar and S. Shimamoto, "Channel characterization and performance evaluation of mobile communication employing stratospheric platforms," *IEICE Transactions on Communications*, vol. E89-B, no. 3, pp. 937-944, Mar. 2006.

[42] D. W. Matolak and R. Sun, "Unmanned aircraft systems: air-ground channel characterization for future applications," *IEEE Veh. Technol. Mag.*, vol. 10, no. 2, pp. 79–85, Jun. 2015.

[43] B. Kumbhani and R. S. Kshetrimayum, *MIMO Wireless Communications over Generalized Fading Channels*, CRC Press, 2017.

[44] A. Aragón-Zavala, J. L. Cuevas-Ruíz, and J. A. Delgado-Penín, *High-Altitude Platforms for Wireless Communications*, New York, USA: John Wiley & Sons, Dec. 2008.

[45] H. A. David and H. N. Nagaraja, *Order Statistics*, 3rd ed, John Wiley & Sons, 2003.

[46] M.S. Alouini, A.J. Goldsmith, Adaptive modulation over Nakagami fading channels, Wirel. Pers. Commun. 13 (1) (2000) 119-143.

[47] L. Hanzo, C.H. Wong, M.S. Yee, Adaptive wireless transceivers: Turbo-Coded, Turbo-Equalised and Space-Time Coded TDMA, CDMA and OFDM Systems, John Wiley & Sons Ltd, 2002.

[48] RESOLUTION 221 (Rev.WRC-07), Use of high-altitude platform stations providing IMT-2000 in the bands 1885-1980 MHz, 2010-2025 MHz and 2110-2170 MHz in Regions 1 and 3 and 1885-1980 MHz and 2110-2160 MHz in Region 2, International Telecommunication Union, Geneva, Switzerland, 2007.

# 4

Single-User Multi-Relay Aerospace Communications

4.1   Introduction

This chapter investigates the use of two aerial relay platforms acting as DF relay nodes, in order to facilitate challenging triple-hop long-range wireless communication between two terrestrial mobile stations. Although the AF scheme is simple to implement, DF offers better performance and is a common assumption in multi-hop networks. A mixed SISO Radio-Frequency/Free-Space-Optical/Radio-Frequency (RF/FSO/RF) airborne communication scenario is initially considered, where an RF transmission scheme is adopted for the communication between the terrestrial stations and the relays, whereas these relays are interconnected through an FSO link. Since FSO systems should operate under accurate pointing requirements, employing FSO techniques is highly challenging and insufficient as soon as the terrestrial stations are in motion. Apart from considering single antennas and apertures, this chapter also studies a MIMO RF/FSO/RF scenario. Since an air-to-ground communication channel is expected to be Rician in its general form [1], the Rician distribution is adopted to model the channels for the RF links. To investigate the effect of atmospheric turbulence on the FSO link, a Kolmogorov power spectrum for refractive-index fluctuations is considered and the Gamma-Gamma (G-G) distribution is used, which matched data values obtained from measurements, under a variety of turbulence conditions [2]. Finally, the effects of pointing errors are described by the Rayleigh distribution [3]. Mathematical expressions are derived for the outage probability and numerical results are provided for different values of the system parameters.

The rest of the chapter is organized as follows. Section 4.2 presents the system model. In Section 4.3, the RF and FSO fading channels are modeled. In Section 4.4, the outage probability is mathematically derived. Section 4.5 presents the MIMO extension of the system model. Finally, results are provided in Section 4.6.

4.2 System Model

In this chapter, a mixed RF/FSO/RF airborne communication system with slowly-varying and frequency-flat-fading channels is considered. As shown in Fig. 4.1, the transmitted signal from a source node propagates through two serial DF stratospheric relays of similar size and type before arriving at a destination node. It is considered that the direct link between the source and the destination is obstructed due to high attenuation. To aid our analysis, the subscripts S, D, and R_m, where $1 \leq m \leq 2$, are affiliated with the source, the destination, and the m-th relay, respectively. In this system, the S–R_1 and R_2–D links use RF technology, while the R_1–R_2 link is based on FSO technology. The communication is assumed to operate in a half-duplex mode and to be conducted over three phases: $S \rightarrow R_1$, $R_1 \rightarrow R_2$, and $R_2 \rightarrow D$. The source and the destination are equipped with single antennas. Besides, the relays not only include single antennas, but also single lasers and single photo-detectors.
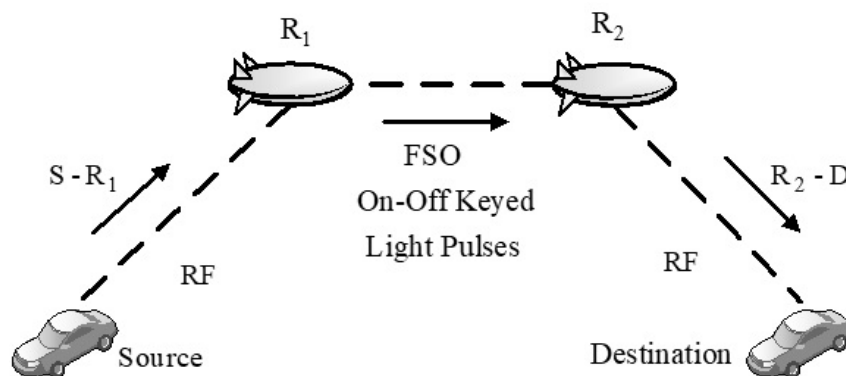
Fig. 4.1: Simple representation of a three-hop mixed RF/FSO/RF stratospheric communication system.

The received signal at the stratospheric relay R_1 can be expressed as [4]

$$y_{S,R_1} = \sqrt{P_S}\, h_{S,R_1} x_{S,R_1} + n_{R_1},$$ (4.1)

where P_S is the transmit power, h_{S,R_1} is a non-zero-mean complex Gaussian random variable, x_{S,R_1} is the transmitted symbol from the source with $\mathrm{E}\left[\left|x_{S,R_1}\right|^2\right]=1$, and n_{R_1} represents the zero-mean complex Gaussian noise at R_1 with N_{o,R_1} noise Power Spectral Density (PSD). Using (4.1), the instantaneous Signal-to-Noise Ratio (SNR) at R_1 can be written, respectively, as

$$\gamma_{S,R_1} = \frac{P_S}{N_{O,R_1}}\left|h_{S,R_1}\right|^2,$$ (4.2)

In the FSO link, the cost-effective Intensity Modulation Direct-Detection (IM/DD) is employed. The received RF signal at the R_1 is decoded and converted to optical signal by employing the Subcarrier Intensity Modulation (SIM) technique. In particular, after filtering by a Bandpass Filter (BPF), a Direct Current (DC) bias is added to the filtered RF signal to ensure that the optical signal is non-negative. Then, the biased signal is sent to a continuous wave laser driver. The retransmitted optical signal at R_1 is written as [5]

$$y_{R_1,opt} = \sqrt{P_{opt}}\left(1 + M y_{S,R_1}\right),$$ (4.3)

where P_{opt} denotes the average transmitted optical power and it is related to the relay electrical power P_{R_1} by the electrical-to-optical conversion efficiency η_1 as $P_{opt} = n_1 P_{R_1}$, and M denotes the modulation index.

The optical signal at R_2 received from R_1 can be expressed as

$$y_{R_1,R_2} = I\left[\sqrt{P_{opt}}\left(1 + M y_{S,R_1}\right)\right] + n_{R_2},$$ (4.4)

where $I > 0$ is the received fading gain (irradiance) between the laser of R_1 and the photodetector of R_2 through the optical channel and n_{R_2} is the zero-mean complex Gaussian noise at R_2 with N_{o,R_2} noise PSD.

The DC component is filtered out at R_2 and an optical-to-electrical conversion is performed. Then, assuming that $M = 1$, the received signal can be expressed as

$$y_{R_1,R_2} = I\sqrt{P_{ele}}\left[\sqrt{P_{opt}}\,y_{S,R_1}\right] + n_{R_2}, \tag{4.5}$$

where $P_{ele} = n_2 P_{opt} = n_1 n_2 P_{R_1}$ is the electrical power received at R_2 and n_2 is the optical-to-electrical conversion efficiency.

The instantaneous SNR at R_2 can be approximated as [4]

$$\gamma_{R_2} \simeq \min\left\{\gamma_{S,R_1}, \gamma_{R_1,R_2}\right\}, \tag{4.6}$$

where $\gamma_{R_1,R_2} = \left(n_1 n_2 P_{R_1} I^2\right)/N_{o,R_2}$. The performance of the FSO link is limited by background radiation and thermal noise, which can be modeled as Independent and Identically Distributed (i.i.d.) AWGN, as an accurate approximation of the Poisson photon-counting detection model [6].

The FSO signal at the R_2 is finally reconverted to an RF signal before being sent to the destination over the second RF link. The signal received at the destination can be written as

$$y_D = \sqrt{P_{R_2}}\,h_{R_2,S}\,x_{R_2,S} + n_D, \tag{4.7}$$

where P_{R_2} is the transmit power, $h_{R_2 S}$ is a non-zero-mean complex Gaussian random variable (leading to a Rician distributed amplitude), $x_{R_2,S}$ is the signal transmitted by the R_2 with $E\left\{\left|x_{R_2,S}\right|^2\right\} = 1$, and n_D is the zero-mean complex Gaussian noise at D with $N_{o,D}$ noise PSD. Using (4.7), the SNR at the destination can be written as

$$\gamma_{R_2,D} = \frac{P_{R_2}}{N_{O,D}} \left| h_{R_2,D} \right|^2. \tag{4.8}$$

The instantaneous end-to-end SNR at the destination can be approximated as [4]

$$\gamma_D \simeq \min \left\{ \gamma_{S,R_1}, \gamma_{R_1,R_2}, \gamma_{R_2,D} \right\}. \tag{4.9}$$

4.3 Statistical Channel Modeling

In this chapter, the Rician distribution is utilized to model the channels for the RF links. The Probability Density Function (PDF) of the instantaneous SNR received at R_1, denoted as γ_{S,R_1}, is given by [7]

$$f_{\gamma_{S,R_1}}\left(\gamma_{S,R_1}\right) = \frac{K_1+1}{\bar{\gamma}_{S,R_1}} \exp\left(-\left(K_1+1\right)\frac{\gamma_{S,R_1}}{\bar{\gamma}_{S,R_1}} - K_1\right) I_0\left(2\sqrt{K_1\left(K_1+1\right)\frac{\gamma_{S,R_1}}{\bar{\gamma}_{S,R_1}}}\right), \tag{4.10}$$

where K_1 is the Rician factor of the first RF link, i.e., the average power ratio of the line-of-sight (LoS) component to the Non-Line-of-Sight (NLoS) component, and $I_0(\cdot)$ is the modified Bessel function of the first kind and zero-th order. The Rician factor K_1 strongly depends on the elevation angle of the relays and the operating frequency [8]. The PDF $f_{\gamma_{R_2,D}}\left(\gamma_{R_2,D}\right)$ of the Rician distribution for the second RF link with Rician factor K_2 can be defined as in the first RF link by replacing the indices.

For the FSO link, a composite optical channel model is used, which includes the effects of the atmospheric attenuation, the turbulence, and the pointing errors [9]. The channel state I models the random attenuation of the propagation channel and arises due to the path loss I^l, the atmospheric turbulence I^a, and the pointing errors I^p. The combined optical channel model is defined as follows

$$I = I^l I^a I^p. \tag{4.11}$$

Since the time scales of these fading processes are of the order of 10^{-3} s to -10^{-2} s [10], which are far larger than the bit interval $\left(\approx 10^{-9} \text{ s for multi-Gbps systems}\right)$, I is considered to be constant over a large number of transmitted bits [11].

4.3.1 Effects of Atmospheric Attenuation

The atmospheric attenuation is deterministic and is defined by the exponential Beers–Lambert Law [12]

$$I^{l}(L) = \exp(-\sigma L), \tag{4.12}$$

where $I^{l}(L)$ represents the atmospheric attenuation loss of the FSO link over a path of length L and σ is the wavelength- and weather- dependent attenuation coefficient. The attenuation I^{l} is considered fixed during a long period of time.

4.3.2 Effects of Turbulence

In this chapter, the effects of turbulence are modeled using the G-G distribution. Hence, the PDF of I^{a} is given by [13]

$$f_{I^{a}}\left(I^{a}\right) = \frac{2(ab)^{(a+b)/2}}{\Gamma(a)\Gamma(b)} \left(I^{a}\right)^{\frac{(a+b)}{2}-1} K_{a-b}\left(2\sqrt{abI^{a}}\right), \tag{4.13}$$

where $K_{u}(\cdot)$ is the u-th order modified Bessel function of the second kind. Note that (4.13) can be written in terms of the Meijer's G-function as $K_{u}(x) = 0.5 G_{0,2}^{2,0}\left[x^{2}/4 \,\middle|\, u/2 \; u/2\right]$ [14]. The parameters a and b are directly related to the atmosphere and can be adjusted to achieve a good agreement between $f_{I^{a}}\left(I^{a}\right)$ and measurement data. These parameters are determined by the Rytov scintillation model. However, for large distances, as those involved in the proposed system, this model is inappropriate due to the hot spot displacement of the beam caused by the beam wander, i.e., the deflection of the beam due to

turbulence. By considering the beam wander effect, a and b can be modeled as [15]

$$a = \left[\frac{4.42\sigma_R^2 \Lambda_e^{5/6} \sigma_{pe}^2}{w_{LT}^2} + \exp\left(\frac{0.49\sigma_B^2}{\left(1 + 0.56(1+\Theta)\sigma_B^{12/5}\right)^{7/6}} \right) - 1 \right]^{-1}, \qquad (4.14)$$

$$b = \left[\exp\left(\frac{0.51\sigma_B^2}{\left(1 + 0.69\sigma_B^{12/5}\right)^{5/6}} \right) - 1 \right]^{-1}, \qquad (4.15)$$

where $\sigma_R^2 = 1.23 C_n^2 k^{7/6} L^{11/6}$ is the Rytov variance, C_n^2 is the index of refraction structure parameter, $\Lambda_e = 2L / kw_{LT}^2$, $k = 2\pi / \lambda$ is the wave number, λ is the carrier wavelength, $w_{LT} = w\sqrt{1 + 1.33\sigma_R^2 \Lambda^{5/6}}$ is the long-term spot radius, w is the beam radius at the receiver, $\Lambda = 2L / kw^2$, σ_{pe}^2 is the variance of pointing error caused by beam wander ([16], p. 350), σ_B^2 is the Rytov variance with beam wander correction ([16], p. 351), $\Theta = \Theta_0 / \left(\Theta_0^2 + \Lambda_0^2\right)$, $\Theta_0 = 1 - L / F_0$, F_0 is the phase curvature parameter of the Gaussian beam at the transmitter, $\Lambda_0 = 2L / kw_0^2$, and w_0 is the transmitter beam radius. Using [17, eq. (3)], one can also obtain the Scintillation Index (SI) σ_I^2. The value of C_n^2 represents the turbulence condition of the atmosphere and can be estimated using the Hufnagel-Valley model, which is based on various empirical scintillation data of the atmosphere. This model defines the index of refraction structure parameter as a function of the wind speed and the altitude of the aerial platforms above the ground level as ([16], p. 481)

$$C_n^2(h) = 0.00594 \left(\frac{u}{27} \right)^2 \left(10^{-5} h \right)^{10} \exp\left(-\frac{h}{1000} \right)$$

$$+ 2.7 \times 10^{-16} \exp\left(-\frac{h}{1500} \right) + \hat{A} \exp\left(-\frac{h}{100} \right), \qquad (4.16)$$

where $\hat{A}$ is the nominal value of the $C_n^2(0)$ at the ground, u is wind speed in m/s, and h is the altitude of the aerial platforms in meters. As C_n^2 increases, the turbulence becomes stronger. For applications involving propagation along a horizontal path, it is customary to assume that C_n^2 remains constant [16].

4.3.3 Effects of Pointing Errors

To ensure that the communication scenario is viable, proper LoS alignment between the relays via appropriate pointing and tracking mechanisms is required. In this chapter, a model that incorporates geometric spreading in the pointing error PDF ([12], p. 1703) is used. Considering a Gaussian beam profile of beam waist w_z (at a distance z) and modeling the random radial displacement of the beam at the detector as Rayleigh distributed, the PDF of the pointing error I^p includes the random attenuation due to both geometric spreading and pointing errors and can be expressed as [12]

$$f_{I^p}\left(I^p\right) = \frac{\gamma^2}{(A)^{\gamma^2}}\left(I^p\right)^{\gamma^2-1}, \ 0 \leq I^p \leq A, \qquad (4.17)$$

where $\gamma = w_{eq}/2\sigma_s$, $w_{eq}^2 = w_z^2\sqrt{\pi}\cdot\mathrm{erf}(u)/\left[2u\exp\left(-u^2\right)\right]$ is the equivalent beam width at the receiver, $u = \left(\sqrt{\pi}a_r\right)/\left(\sqrt{2}w_z\right)$, σ_s is the jitter standard deviation due to the pointing error at the detector determined by the degree of the misalignment between the transmitter and receiver apertures, $A = \left[\mathrm{erf}(u)\right]^2$, and a_r is the receiver aperture radius.

Using (4.12), (4.13), and (4.17), the PDF of the composite channel in (4.11) can be evaluated by writing the Bessel function $K_u(\cdot)$ in terms of the Meijer's G-function as [3]

$$f_I(I) = \frac{ab\gamma^2}{AI\Gamma(a)\Gamma(b)}G_{1,3}^{3,0}\left[\frac{ab}{AI^l}I \ \middle| \ \begin{matrix} \gamma^2 \\ \gamma^2-1, a-1, b-1 \end{matrix}\right]. \qquad (4.18)$$

Using (4.18), the PDF of the instantaneous SNR received at R_2, denoted as γ_{R_1,R_2}, can be expressed as

$$f_{\gamma_{R_1,R_2}}\left(\gamma_{R_1,R_2}\right)=\frac{ab\gamma^2}{2AI'\Gamma(a)\Gamma(b)}\sqrt{\frac{1}{\gamma_{R_1,R_2}\overline{\gamma}_{R_1,R_2}}}G_{1,3}^{3,0}\left[\frac{ab}{AI'}\sqrt{\frac{\gamma_{R_1,R_2}}{\overline{\gamma}_{R_1,R_2}}}\middle|\begin{array}{c}\gamma^2\\\gamma^2-1,a-1,b-1\end{array}\right],(4.19)$$

where $\overline{\gamma}_{R_1,R_2}$ is the average SNR received at R_2.

4.4 Derivation of the Outage Probability

The outage probability is defined as the probability that the SNR at the destination falls below a predetermined outage threshold γ_{out}, i.e., $P_{out}=\Pr[\gamma_D\leq\gamma_{out}]$, where $\Pr[\cdot]$ is the probability operation. In this case, the communication system cannot achieve adequate reception. The outage probability can be obtained from the Cumulative Distribution Function (CDF) of the end-to-end SNR as $P_{out}=F_{\gamma D}(\gamma_{out})$. This CDF can be written in terms of the CDFs of the three hops' SNRs as [18]

$$P_{out}=F_{\gamma D}\left(\gamma\right)=1-\left[\left(1-F_{\gamma S,R_1}\left(\gamma\right)\right)\left(1-F_{\gamma R_1,R_2}\left(\gamma\right)\right)\left(1-F_{\gamma R_1,D}\left(\gamma\right)\right)\right], \qquad (4.20)$$

where $F_{\gamma S,R_1}(\gamma)$, $F_{\gamma R_1,R_2}(\gamma)$, and $F_{\gamma R_1,D}(\gamma)$ are the CDFs of the SNRs of the first, second, and third hop, respectively. One observes that the system falls in outage providing that at least one of the three hops gets in outage or, equivalently, the SNR of one hop becomes less than γ_{out}.

The CDF of the instantaneous SNR received at R_1 can be expressed as [19]

$$F_{\gamma_{S,R_1}}\left(\gamma_{S,R_1}\right)=1-Q_1\left[\sqrt{2K_1},\sqrt{\frac{2(K_1+1)}{\overline{\gamma}_{S,R_1}}\gamma_{S,R_1}}\right], \qquad (4.21)$$

where $Q_1[\cdot]$ is the Marcum Q_1-function. The CDF $F_{\gamma_{R_2,D}}\left(\gamma_{R_2,D}\right)$ of the Rician distribution for the second RF link can be similarly defined by replacing the indices.

The CDF of the instantaneous SNR received at R_2 can be obtained as follows

$$F_{\gamma_{R_1 R_2}}\left(\gamma_{R_1,R_2}\right)=\int_0^{\gamma_{R_1,R_2}} f_{\gamma_{R_1,R_2}}\left(x\right)dx. \tag{4.22}$$

Using (4.19) and [20, eq. (07.34.21.0003.01)], (4.22) becomes

$$F_{\gamma_{R_1,R_2}}\left(\gamma_{R_1,R_2}\right)=\frac{ab\gamma^2}{Al'\Gamma\left(a\right)\Gamma\left(b\right)}\sqrt{\frac{\gamma_{R_1,R_2}}{\overline{\gamma}_{R_1,R_2}}}G_{2,4}^{3,1}\left[\frac{ab}{Al'}\sqrt{\frac{\gamma_{R_1,R_2}}{\overline{\gamma}_{R_1,R_2}}}\left|\begin{array}{c}0,\gamma^2\\\gamma^2-1,a-1,b-1,-1\end{array}\right.\right]. \tag{4.23}$$

The expressions in (4.21) and (4.23) can be numerically evaluated using well-known software packages, e.g., Mathematica and MATLAB.

4.5 Application of MIMO Technology

Since the RF links act as a bottleneck and limit the end-to-end data rate of RF/FSO systems, MIMO techniques for the RF links are employed in this section. In particular, this section studies a multiple-relay-assisted MIMO airborne communication system with slowly-varying and frequency-flat-fading channels. As shown in Fig. 4.2, the transmitted signal from a source node propagates through two DF serial stratospheric relays, being in distance L, before arriving at the destination node. These relays are of similar size and type, are situated approximately 20 km above the ground, and act as optical transceivers. It is considered that the direct link between the source and the destination is obstructed due to high attenuation. Note that there exist three point-to-point propagation links before the source signal is arriving at the destination. The proposed communication system involves mixed RF/FSO/RF links, i.e., the S-R_1 and R_2-D links use RF technology, while the link between the relays is based on FSO technology. The RF channels are Nakagami-m, $m \geq 1/2$, fading RF MIMO channels with the source, the relays, and the destination equipped with L_S, L_R, and L_D antenna elements, respectively. The relays also include single transmit apertures (or photo sources), which are simultaneously intensity modulated with identical

signals (repetition coding across lasers, e.g. [21], and single receive apertures (or photo-detectors). The first relay, i.e., R_1, converts the received RF signals to the optical signals with a SIM scheme. Then, this relay transmits the FSO signal modulated with on-off keying (OOK), which is widely employed in practical systems, to the destination through the second aerial relay platform.
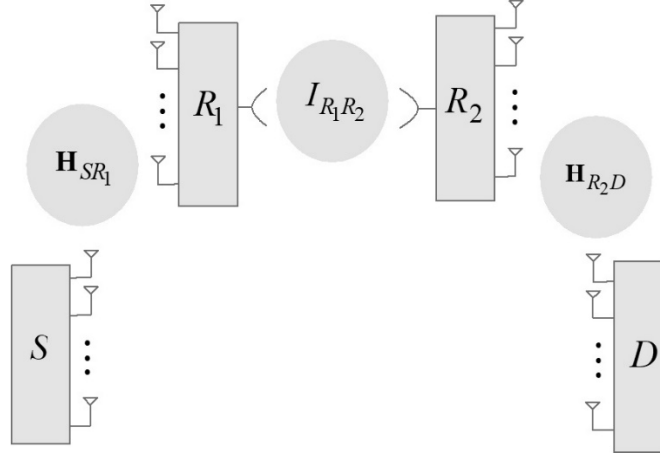
Fig. 4.2: The MIMO mixed RF/FSO/RF fading channel.

More specifically, the source transmits L_S number of data symbols simultaneously to R_1 over Nakagami-m fading RF MIMO channels. The received signal vector $\mathbf{y}_{S,R_1} \in \mathbb{C}^{L_R \times 1}$ at the stratospheric relay R_1 is:

$$\mathbf{y}_{S,R_1} = \sqrt{\frac{P_S}{L_S}} \mathbf{H}_{S,R_1} \mathbf{s} + \mathbf{n}_{R_1}, \tag{4.24}$$

where P_S is the total source transmit power, $\mathbf{H}_{SR_1} \in \mathbb{C}^{L_R \times L_S}$ is the channel transfer matrix for the transmission from the source to the 1st relay, $\mathbf{s} \in \mathbb{C}^{L_S \times 1}$ is the signal vector transmitted by the source with $\mathrm{E}\left[\mathbf{s}\mathbf{s}^H \right] = \mathbf{I}_{L_S}$, and $\mathbf{n}_{R_1} \sim \mathcal{NC}\left(\mathbf{0}, N_{o,R_1} \mathbf{I}_{L_R} \right)$ is the $L_R \times 1$ zero-mean circularly symmetric complex Gaussian noise vector at the relay, where N_{o,R_1} is the noise power spectral density (PSD). By employing a ZF receiver,

the instantaneous SNR for the ith symbol corresponding to the S-R_1 link can be expressed as [22]

$$\gamma_{S,R_1}^i = \frac{P_S}{L_S N_{O,R_1} \left[\left(\mathbf{H}_{SR_1}^H \mathbf{H}_{SR_1} \right)^{-1} \right]_{i,i}},$$ (4.25)

where $i = 1, 2, ..., L_S$ and $\mathbf{H}_{SR_1}^H \mathbf{H}_{SR_1}$ is a $L_S \times L_S$ complex Wishart distributed matrix with L_R degrees of freedom. Note that $L_R \geq L_S$, in order to decode all the L_S transmitted symbols using the ZF receiver.

In the FSO long-haul links, the cost-effective IM/DD is employed, where the transmitted signals are real and non-negative. The relay R_1 decodes the received bits using ZF receiver, i.e., it multiplies the pseudo-inverse of $\mathbf{H}_{S,R_1}$ with the received vector $\mathbf{y}_{S,R_1}$ and forwards them to the relay R_2 over the first FSO link. Then, these bits are converted to optical signal by employing the SIM technique, and then forwarded to the R_2 over an FSO link. In particular, after filtering by a BPF, a DC bias is added to the filtered RF signal to ensure that the optical signal is non-negative. Then, the biased signal is sent to a continuous wave laser driver. The instantaneous SNR at R_2 can be expressed using (4.6).

The FSO signal at the R_2 is finally reconverted to an RF signal before being sent to the destination over the second RF link. The received signal vector $\mathbf{y}_{R_2,D} \in \mathbb{C}^{L_D \times 1}$ at the destination can be written as

$$\mathbf{y}_{S,R_1} = \sqrt{\frac{P_{R_2}}{L_R}} \mathbf{H}_{R_2,D} \mathbf{c} + \mathbf{n}_D,$$ (4.28)

where $\mathbf{H}_{R_2 D} \in \mathbb{C}^{L_D \times L_R}$ is the channel transfer matrix for the transmission from the 2nd relay to the destination, $\mathbf{c} \in \mathbb{C}^{L_R \times 1}$ is the signal vector transmitted by the second relay with $\mathrm{E}\left[\mathbf{c}\mathbf{c}^H \right] = \mathbf{I}_{L_R}$, and $\mathbf{n}_D \sim \mathcal{NC}\left(\mathbf{0}, N_{o,D} \mathbf{I}_{L_D} \right)$ is the $L_D \times 1$ zero-mean circularly symmetric complex Gaussian noise vector at the destination, where $N_{o,D}$ is the

noise PSD. By employing a ZF receiver, the instantaneous SNR for the ith symbol corresponding to the R_1-D link can be expressed as [22]

$$\gamma_{R_2D}^i = \frac{P_{R_2}}{L_R N_{O,D}\left[\left(\mathbf{H}_{R_2D}^H \mathbf{H}_{R_2D}\right)^{-1}\right]_{i,i}},$$

(4.29)

where $\mathbf{H}_{R_2D}^H \mathbf{H}_{R_2D}$ is a $L_R \times L_R$ complex Wishart distributed matrix with L_D degrees of freedom. Note that $L_D \geq L_R$, in order to decode all the L_R transmitted symbols using the ZF receiver. Note that the CDF of γ_{S,R_1}^i and $\gamma_{R_2D}^i$ of the Nakagami-m distribution for MIMO channels can be written using (3.27), whereas the instantaneous end-to-end SNR at the destination can be approximated using (4.9). Then, the outage probability can be calculated using (4.20).

4.6 Numerical Results

In this section, the performance of the proposed system is evaluated in terms of the outage probability. Unless indicated otherwise, the values of model parameters used are $\overline{\gamma}_{S,R_1} = \overline{\gamma}_{R_2,D} = 20$ dB, $\overline{\gamma}_{R_1,R_2} = 50$ dB, $\gamma_{out} = 0$ dB, $K_1 = K_2 = K = 10$ dB, $L = 400$ km, $h = 20$ km, $\sigma = 0.01$ dB/km (clear weather conditions), $w = w_0 = 2$ cm, $\Theta_0 = 0$ (focus Gaussian beam), and $\sigma_s = 0.15$ m. Note that a laser aperture diameter of $2a_r = 0.3$ m is assumed. Then, $w_z = 1.38$ m [23]. A wavelength $\lambda = 1550$ nm is considered for the FSO link since it is widely used for most airborne optical communication scenarios. In addition, two values of the wind speed that determine C_n^2 are considered; $u_1 = 10$ m/s (best case) and $u_2 = 30$ m/s (worst case) [17]. For these values, we obtain $C_{n,u_1}^2 \approx 1.72 \cdot 10^{-19}$ m$^{-2/3}$, $C_{n,u_2}^2 \approx 1.55 \cdot 10^{-18}$ m$^{-2/3}$, $\sigma_{R,u_1}^2 \approx 0.2$, $\sigma_{R,u_2}^2 \approx 1.82$, $\sigma_{I,u_1}^2 \approx 0.08$, and $\sigma_{I,u_2}^2 \approx 0.67$.

Figure 4.3 depicts the outage probability for different values of the Rician factor $K_1 = K_2 = K$ and $u = 10$ m/s. It is obvious that increasing the Rician factor improves the performance of the system. Note that a certain outage floor exists at high

values of K due to the average SNR over the FSO link. Hence, all curves tend to the same saturation floor.

Figure 4.4 demonstrates the outage probability for both the best and worst case of turbulence conditions and different inter-platform distance. As this distance decreases, a significant performance improvement can be achieved. However, the variation of the FSO propagation distance slightly affects the outage probability when the worst case of turbulence conditions is observed.

Figure 4.5 shows the effect of the normalized jitter standard deviation σ_s / a_r on the outage probability for u = 10 m/s. One observes that the performance significantly degrades and the pointing errors have a dominant effect on the system performance, as σ_s / a_r increases.
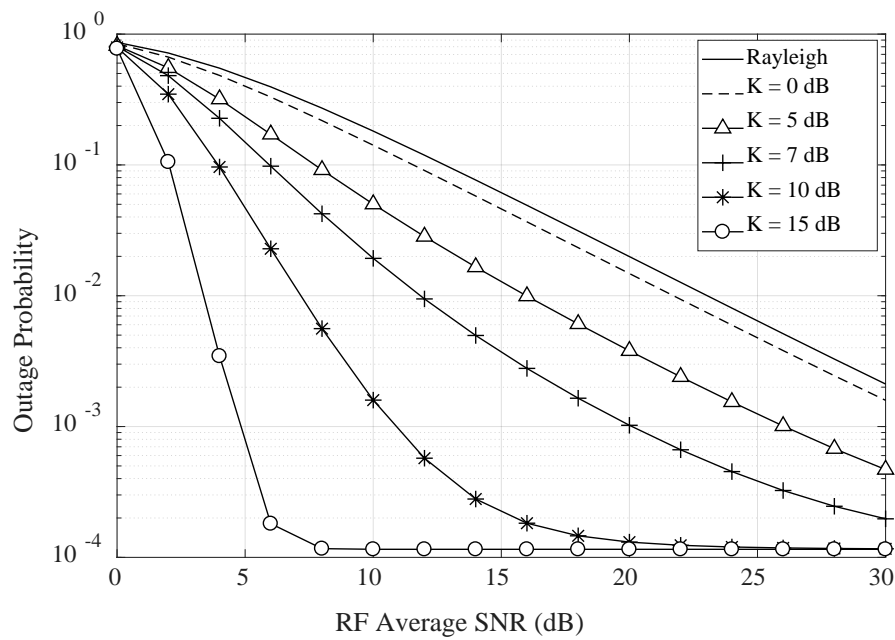
Fig. 4.3: The outage probability in terms of the RF average SNR for different Rician factor of the RF links.
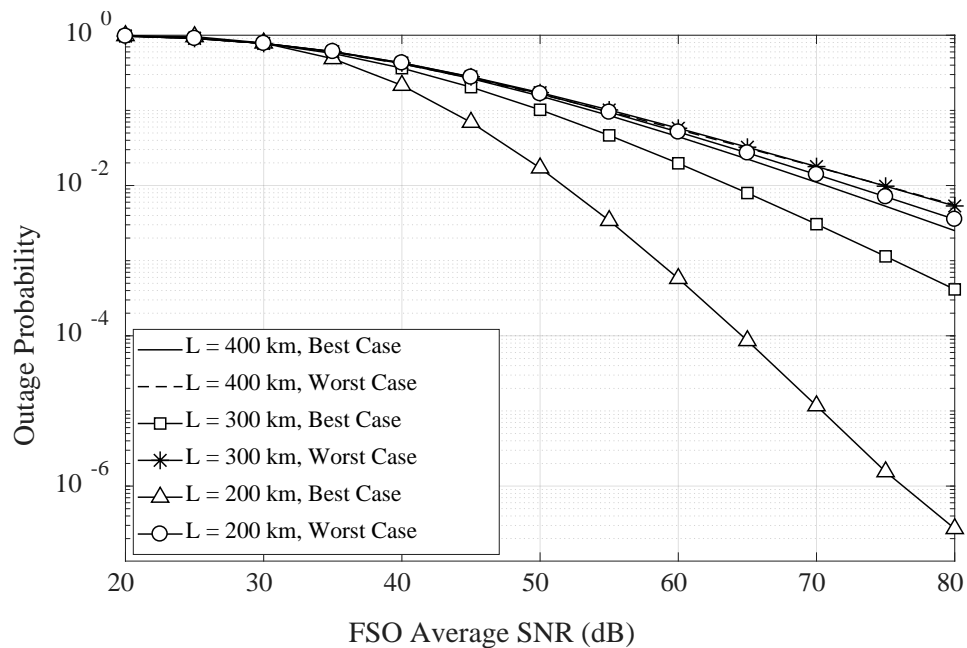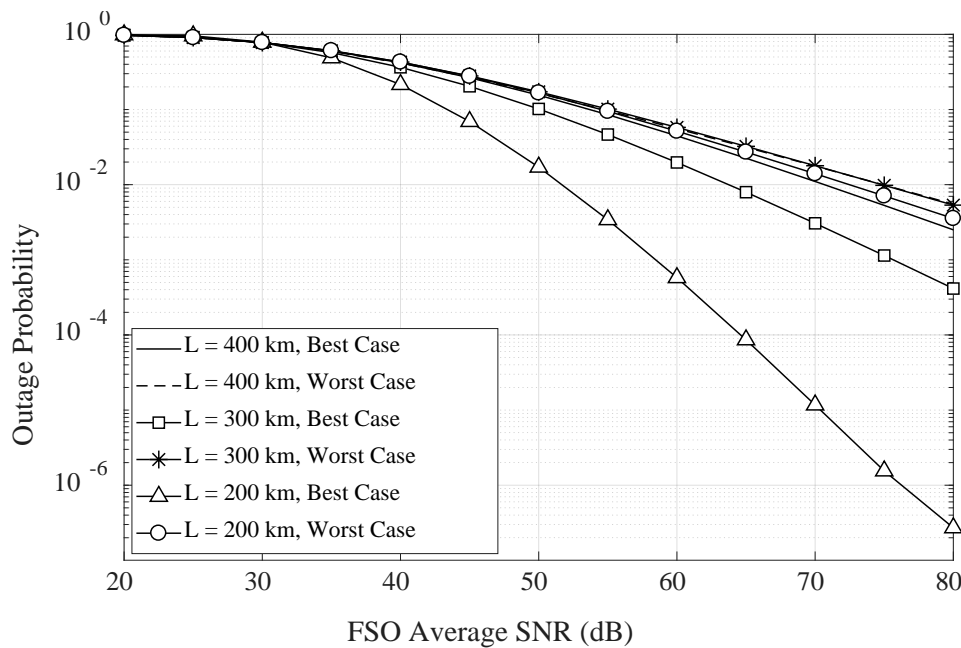
Fig. 4.4: The outage probability in terms of the FSO average SNR for different turbulence strength and different inter-platform distance.
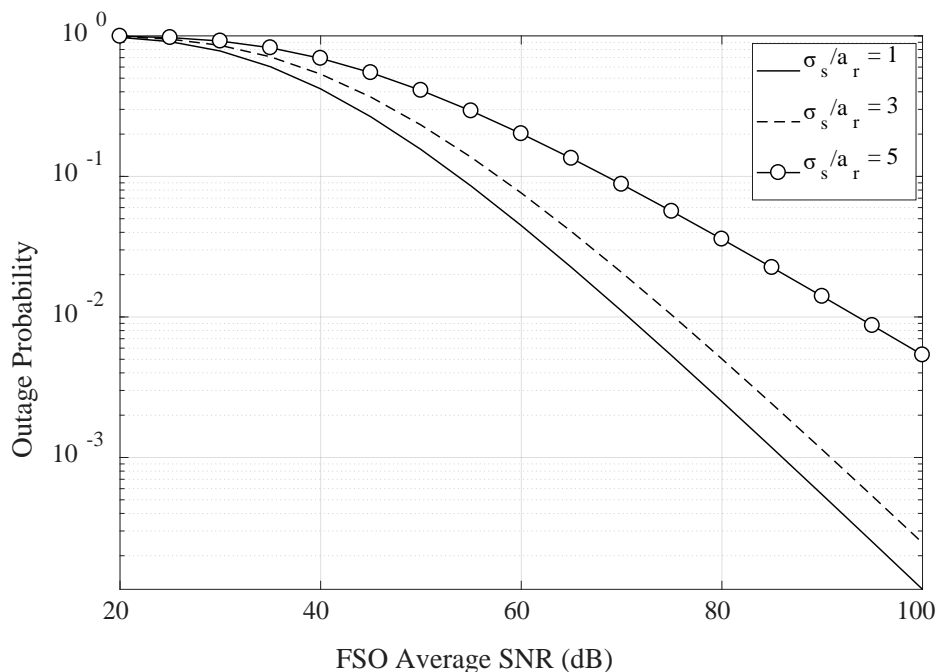
Fig. 4.5: The outage probability in terms of the FSO average SNR for different normalized jitter standard deviation.

Figure 4.6 demonstrates the outage probability for both the best and worst case of turbulence conditions and different inter-platform distance. As this distance decreases, a significant performance improvement can be achieved. However, the variation of the FSO propagation distance slightly affects the outage probability when the worst case of turbulence conditions is observed.

Fig. 4.6: The outage probability in terms of the FSO average SNR for different turbulence strength and different inter-platform distance.

REFERENCES

[1] A. Aragón-Zavala, J. L. Cuevas-Ruíz, and J. A. Delgado-Penín, *High Altitude Platforms for Wireless Communications*, 1st ed. New York: Wiley, Dec. 2008.

[2] F. S. Vetelino, C. Young, L. Andrews, and J. Recolons, "Aperture averaging effects on the probability density of irradiance fluctuations in moderate-to-strong turbulence," *Applied Optics*, vol. 46, no. 11, pp. 2099-2108, Apr. 2007.

[3] M. Sharma, D. Chadha, and V. Chandra, "High-altitude platform for free-space optical communication: Performance evaluation and reliability analysis," *J. Opt. Commun. Netw.*, vol. 8, no. 8, pp. 600-609, Aug. 2016.

[4] A. M. Salhab, "A New Scenario of Triple-Hop Mixed RF/FSO/RF Relay Network with Generalized Order User Scheduling and Power Allocation," *EURASIP Journal on Wireless Communications and Networking* (2016) 2016:260.

[5] E. Lee, J. Park, D. Han, and G. Yoon, "Performance analysis of the asymmetric dual-hop relay transmission with mixed RF/FSO links," *IEEE Photonic Tech. L.*, vol. 23, no. 21, pp. 1642-1644, 2011.

[6] S. M. Navidpour, M. Uysal, and M. Kavehrad, "BER performance of free-space optical transmission with spatial diversity," *IEEE Trans. Wirel. Commun.*, vol. 6, no. 8, pp. 2813-2819, Aug. 2007.

[7] M. K. Simon and M.-S. Alouini, *Digital Communication over Fading Channels*, 2nd ed. New York: Wiley, 2005.

[8] Iskandar and S. Shimamoto, "Channel characterization and performance evaluation of mobile communication employing stratospheric platforms," *IEICE Trans. on Commun.*, vol. E-B, no. 3, pp. 937-944, Mar. 2006.

[9] C. Datsikas, K. P. Peppas, N. C. Sagias, and G. S. Tombras, "Serial free-space optical relaying communications over gamma-gamma atmospheric turbulence channels," *J. Opt. Commun. Netw.*, vol. 2, pp. 576-586, Jul. 2010.

[10] X. Zhu and J. Kahn, "Free space optical communication through atmospheric turbulence channels," *IEEE Trans. Commun.*, vol. 50, no. 8, pp. 1293–1300, Aug. 2002.

[11] H. G. Sandalidis, "Coded free-space optical links over strong turbulence and misalignment fading channels," *IEEE Trans. Commun.*, vol. 59, no. 3, pp. 669-674, 2011.

[12] A. A. Farid, S. Member, and S. Hranilovic, "Outage capacity optimization for free-space optical links with pointing errors," *J. Lightwave Technol.*, vol. 25, pp. 1702-1710, Jul. 2007.

[13] M. A. Al-Habash, "Mathematical model for the irradiance probability density function of a laser beam propagating through turbulent media," *J. Opt. Eng.*, vol. 40, no. 8, pp. 1554-1562, Aug. 2001.

[14] V. S. Adamchik and O. I. Marichev, "The algorithm for calculating integrals of hypergeometric type functions and its realization in REDUCE system," in *Proc. Int. Conf. on Symbol. and Algeb. Comp.*, Tokyo, Japan, pp. 212-224, 1990.

[15] Y. Ren, A. Dang, B. Luo, and H. Guo, "Capacities for long-distance free-space optical links under beam wander effects," *IEEE Photon. Techn. Lett.*, vol. 22, no. 14, pp. 1069-1071, Jul. 2010.

[16] L. Andrews and R. L. Philips, *Laser Beam Propagation Through Random Media*, 2nd ed. Bellingham, WA: SPIE, pp. 350-351, 2005.

[17] S. Parthasarathy, D. Giggenbach, and A. Kirstädter, "Channel modelling for free-space optical inter-HAP links using adaptive ARQ transmission," in *Proc. SPIE 9248*, 92480Q, pp. 1-11, Oct. 2014.

[18] S. S. Ikki and S. Aissa, "A study of optimization problem for amplify-and-forward relaying over Weibull fading channels with multiple antennas," *IEEE Commun. Lett.*, vol. 15, no. 11, pp. 1148-1151, 2011.

[19] A. A. Abu-Dayya and N. C. Beaulieu, "Switched diversity on microcellular Ricean channels", *IEEE Trans. Veh. Technol.*, vol. 43, no. 4, pp. 970-976, 1994.

[20] The Wolfram Functions Site, 2013. [Online]. Available from: http://functions.wolfram.com [retrieved: March, 2018].

[21] E. Bayaki, R. Schober and R. K. Mallik, "Performance analysis of MIMO free-space optical systems in gamma-gamma fading," *IEEE Transactions on Communications*, vol. 57, no. 11, pp. 3415-3424, Nov. 2009.

[22] B. K. Chalise and L. Vandendorpe, "Performance analysis of linear receivers in a MIMO relaying system," *IEEE Communications Letters*, vol. 13, no. 5, pp. 330–332, 2009.

[23] N. Vaiopoulos, H. G. Sandalidis, and D. Varoutas, "Using a HAP network to transfer WiMAX OFDM signals: Outage probability analysis," *J. Opt. Commun. Netw.*, vol. 5, pp. 711-721, Jul. 2013.

5

Massive MIMO Aerospace Communications

5.1 Introduction

The analysis and design of massive MIMO communications systems require the development of realistic channel models, which enable the proper characterization of the fading channel and the thorough study of the channel statistics. These channel models are significantly different from conventional MIMO channel models as indicated by measurements on massive MIMO channels [1], [2]. Since the number of antennas is huge in massive MIMO systems, the far-field assumption in conventional MIMO channels may no longer be appropriate and the wavefront should be assumed as spherical instead of plane. As shown in [3], the plane wavefront assumption underestimates the rank of the channel matrix. In addition, appearance and disappearance of clusters, i.e., group of physical scattering elements, can occur on the array axis and each antenna may have its own set of observable clusters. As a result, the wide-sense stationarity (WSS) assumption, which assumes that channel statistics are unchanged with respect to time, does not necessarily hold for massive MIMO channels. Also, power imbalance and Rician K-factor variation over the antenna array are seen as well.

The radio links of terrestrial nodes are usually vulnerable to fading effects arising from scattering, reflection, diffraction, or blockage of the radiated energy by objects in the propagation environment. Since impairments of the signal are mainly caused by the environment near to the user, a realistic positioning of the scatterers is essential for an accurate channel model. Thus, when terrain and scattering distributions are available, physical-geometrical models are preferred. In realistic channel models, the scatterers would disperse in elevation (or the vertical plane) and the impact of elevation angles needs to be addressed, as reported in [4]. A 3-D

regular-shaped geometry-based stochastic model (RSGBSM) for MIMO stratospheric channels was proposed in [5]. However, this model is improper because it neglects the impact of the non-stationarity or spherical assumptions on the channel statistics. To address these issues, this chapter proposes a novel 3-D RSGBSM for massive MIMO non-stationary stratospheric channels, which incorporates the spherical wavefront assumption, cluster evolution on the time and array axes, and 3-D cluster properties to capture massive MIMO channel characteristics. In the proposed model, near-field effects caused by the increasing antenna elements are considered, including the variation of the azimuth and elevation angles of arrival/departure (AoA/AoD) and the Doppler frequency for sufficiently separated antenna elements. Note that these azimuth and elevation angles are assumed to be mutually independent. Also, appearance and disappearance of clusters, i.e., cluster evolution, on both the array and time axes are jointly modeled by birth-death processes, which make the proposed massive MIMO channel models essentially non-stationary. The received complex faded envelope is constructed as a superposition of the LoS and the NLoS rays. This model assumes that a cluster of scatterers in the vicinity of a terrestrial mobile station (TMS) can be represented by a cylindrical volume, where the scatterers are non-uniformly distributed. The space-time correlation function (STCF) and the Doppler power spectral density (PSD) are derived considering several parameters, such as the elevation angle of the stratospheric base station (SBS), the array configuration, the Doppler spread, and the distribution of the scatterers. The numerical results demonstrate the theoretical derivations. To the best of the author's knowledge, this is the first 3-D GBSM for massive MIMO non-stationary stratospheric channels.

The remainder of this chapter is organized as follows. In Section 5.2, the massive MIMO stratospheric communication system is described and a 3-D geometrical channel model is introduced. Section 5.3 studies the non-stationarity properties of the proposed theoretical model, whereas Section 5.4 presents the statistical properties. Numerical results are presented in Section 5.5.

5.2 System Model

The system model employed throughout this chapter considers a downlink massive MIMO stratospheric radio channel with L_T transmit and L_R receive antenna elements communicating at carrier frequency f_c and N clusters with I rays in a 3-D space. All antennas are fixed, omni-directional, and are numbered as $1 \leq p \leq p' \leq L_T$ and $1 \leq q \leq q' \leq L_R$, respectively. The L_T antenna elements of the free of local scattering quasi-stationary SBS are situated approximately 20 km above the ground and it is assumed that the L_R antenna elements of the TMS are in motion. The spacing between two adjacent antenna elements at the SBS and TMS is denoted by δ_T and δ_R, respectively. Both azimuth and elevation angles in the 3-D space are considered for clusters, antenna arrays, movement direction of clusters, and movement direction of the TMS antenna array. Note that the far-field conditions for conventional MIMO channels are not assumed in the proposed model. Thus, the wavefront of each wireless link is assumed to be spherical. Then, the azimuth and elevation AoAs and AoDs on the antenna arrays are no longer equal for each antenna element and the phase of each antenna element is determined by geometrical relationships.

It is considered that the propagation environment is characterized by 3-D scattering conditions, where each cluster is represented by a cylinder with radius $R_{n,max}$ ($n = 1, 2, \ldots, N$) and height $H_{n,max}$. In particular, a cylinder is the volume containing a cluster of scatterers and hence the radio waves may travel in both horizontal and vertical planes. As shown in Fig. 5.1, the TMS is located in the center of a multi-cylindrical-shaped region of scattering elements. The distance between the TMS and the scatterers is not constant and the radius of each cylinder corresponds to the maximum distance between the TMS and an effective scatterer (ray), which is positioned within the cylinder. This approach is realistic for stratospheric communications scenarios, due to the high elevation angles and the use of omni-directional antennas at the user terminals. Since the scattered waves are mostly owing to buildings, poles, trees, and hills that can be found only up to a

predefined maximum height, the maximum scatterer height corresponds to the height of the cylinder. The scatterers are randomly distributed in space without considering the length of the path traveled. Note that the path length is compensated by a time delay.

Conventional MIMO channel models assume that a cluster of scatterers is always observable to all the antennas on an antenna array. Since large-scale antenna configurations are used in both the SBS and the TMS, the visibility of the entire number of scatterers from all the antenna elements may be not attained and a cluster may only be observable to a subset of antennas on an antenna array depending on the distance between these elements. More specifically, each antenna has its own set of observable spherical clusters. It is considered that $C_q^R(t)$ $\left(C_p^T(t)\right)$ is the cluster set in which clusters are observable to the q-th (p-th) TMS (SBS) antenna at time instant t. Let N be the total number of clusters that are observable to at least one TMS and one SBS antenna and I be the number of rays within Cluster$_n$. Then, the value of N can be calculated as [6]

$$N = \text{card}\left(\bigcup_{q=1}^{L_R}\bigcup_{p=1}^{L_T}\left(C_p^T(t)\bigcap C_q^R(t)\right)\right), \tag{5.1}$$

where $\text{card}(S)$ denotes the cardinality of a set S and $\bigcup$ and $\bigcap$ represent the union and intersection of sets, respectively. Then, a cluster is observable to the q-th TMS and the p-th SBS antenna if and only if this cluster is in the set $\left\{C_p^T(t)\bigcap C_q^R(t)\right\}$. The sets $\left\{C_q^R(t)\right\}$ and $\left\{C_p^T(t)\right\}$ can be generated based on the cluster evolution (birth-death process) on both the time and array axes as described in Section 5.3.

As $I \rightarrow \infty$, the theoretical model of the wideband massive MIMO channel matrix can be represented as an $L_R \times L_T$ complex matrix $\mathbf{H}(t,\tau) = \left[h_{qp}(t,\tau)\right]_{L_R \times L_T}$. Based on the 3-D model, the multipath complex gains between the p-th SBS antenna and the q-th TMS antenna at time t and delay τ can be expressed as [6]
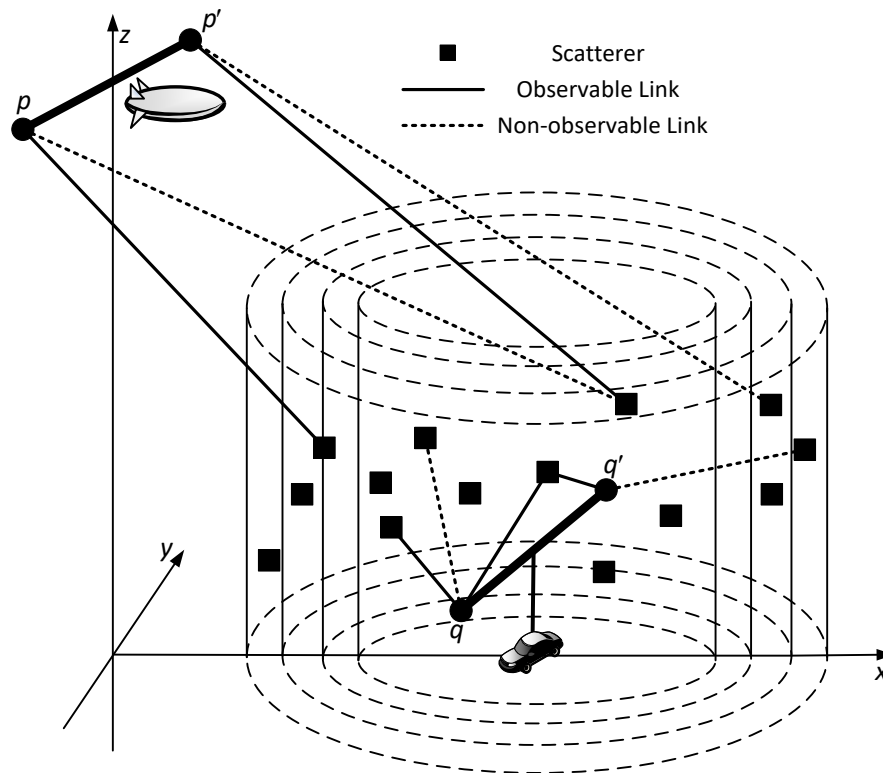
Fig. 5.1: Simple representation of the 3-D RSGBSM multi-cluster massive MIMO stratospheric channel model.

$$h_{q,p}(t,\tau) = \sum_{n=1}^{N_{total}} h_{q,p,n}(t)\delta(\tau - \tau_n(t)). \tag{5.2}$$

-if $Cluster_n \in \left\{ C_p^T(t) \bigcap C_q^R(t) \right\}$,

$$h_{q,p,n}(t) = \delta(n-1)\sqrt{\frac{K_{q,p}}{K_{q,p}+1}}\exp\left[j\left(2\pi f_q^{LoS}t + \varphi_{p,q}^{LoS}\right)\right]$$

$$+\sqrt{\frac{P_n}{K_{q,p}+1}}\lim_{N\to\infty}\frac{1}{\sqrt{N}}\sum_{n=1}^{N}\exp\left[j\left(2\pi f_{q,n,i}t + \varphi_{p,q,n,i}\right)\right] \tag{5.3}$$

-if $Cluster_n \notin \left\{ C_p^T(t) \bigcap C_q^R(t) \right\}$,

$$h_{q,p,n}(t) = 0, \tag{5.4}$$

where K_{qp} is the LoS Rician factor, P_n is the power of the n-th cluster, and f_q^{LoS}, $\varphi_{p,q}^{LoS}$, $f_{q,n,i}$, and $\varphi_{p,q,n,i}$ are derived in Section 5.2.1. To simplify the model, it is assumed that the Rician factor is constant during the generation of channel coefficients.

5.2.1 Geometrical Characteristics

The geometrical characteristics of the proposed model and the definition of the Cartesian coordinate system are illustrated in Fig. 5.2, which presents the LoS and single-bounce NLoS paths of the 3-D vector-based model for a 2x2 MIMO stratospheric channel. Based on this simple configuration, uniform linear arrays (ULAs) with an arbitrary large number of antennas can be constructed. Although it is assumed that both the SBS and TMS are equipped with ULAs, the proposed model can be easily modified to support arbitrary antenna array layouts, such as uniform circular antenna arrays (UCAs), spherical antenna arrays, uniform planar arrays (UPAs), and 3-D cube arrays. Note that shadowing within the cylinder is neglected in this model. In addition, attenuation due to rain, oxygen absorption, water vapor, clouds, precipitation, and vegetation is bypassed, since these atmospheric-environmental phenomena do not significantly affect communication links at L- and S- frequency bands [7]. Let $\tilde{A}$ denote the projection of a point A onto the x-y plane. One observes that the x-axis is the line that connects coordinate origin O (the centre of the projections $\tilde{p}$ and $\tilde{p}'$ of the SBS antenna elements p and p' onto the xy plane), and O' (the lower center of the cylinder). In addition, O_T and O_R are the array centers at the SBS and TMS, respectively. To aid the analysis, the distance between two points a and b is denoted as $d(a,b)$. Then, the distance between $\tilde{O}_T$ and $\tilde{O}_R$ is $d(\tilde{O}_T,\tilde{O}_R)=\tilde{D}_{TR}$ and the heights of the SBS and TMS antennas arrays are $d(\tilde{O}_T,O_T)=H_T$ and $d(\tilde{O}_R,O_R)=H_R$, respectively. Note that $H_T \gg H_R$ and that the elevation angle of SBS relative to O_R is given by

$\theta_T \approx \arcsin\left(H_T / D_{TR}\right)$, where $D_{TR} = d\left(O_T, O_R\right)$ is the initial distance between the SBS and TMS. It is assumed that the TMS is moving with speed v_R in the direction determined by the angle γ_R, whereas SBS is a solar-powered quasi-stationary airship of about 150-200 m in length [7].
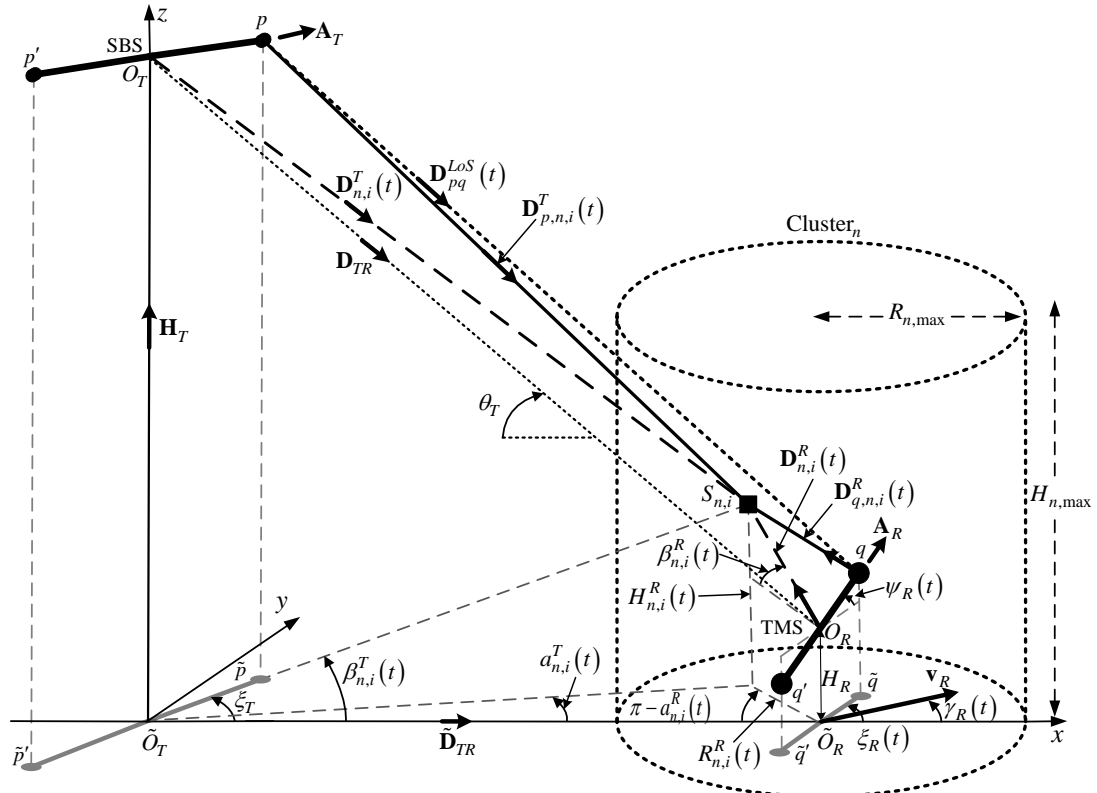

Fig. 5.2: The 3-D RSGBSM model for a 2×2 MIMO stratospheric channel.

The q-th TMS antenna position vector can be expressed as follows

$$\mathbf{A}_q^R(t) = \Delta_R^{(q)} \begin{bmatrix} \cos \xi_R(t)\cos\psi_R(t) \\ \sin \xi_R(t)\cos\psi_R(t) \\ \sin\psi_R(t) \end{bmatrix}^T + \tilde{\mathbf{D}}_{TR}, \qquad (5.5)$$

where $\Delta_R^{(q)} = \left[(L_R + 1)/2 - q\right]\delta_R$, $\xi_R(t)$ represents the orientation of the TMS antenna array relative to the x-axis, $\psi_R(t)$ is the elevation angle of the qth TMS

antenna element, and $\tilde{\mathbf{D}}_{TR} = \left[\tilde{D}_{TR}, 0, 0\right]^T$ denotes the initial position vector of the TMS, where $\tilde{D}_{TR} \approx H_T / \tan\theta_T$. The p-th SBS antenna position vector is similarly defined; however, assuming that the SBS antenna array is parallel to the xy plane and SBS displacements along the x-, y-, and z-axes due to stratospheric winds and pressure variations are ignored, $\psi_T = 0$ and thus we obtain

$$\mathbf{A}_p^T = \Delta_T^{(p)} \begin{bmatrix} \cos\xi_T \\ \sin\xi_T \\ 0 \end{bmatrix}^T + \mathbf{H}_T, \tag{5.6}$$

where $\Delta_T^{(p)} = \left[(L_T + 1)/2 - p\right]\delta_T$ and $\mathbf{H}_T = \left[0, 0, H_T\right]^T$ denotes the initial position vector of the SBS. It should be noticed that the position vectors are time-dependent. In addition, the LoS distance vector between the p-th SBS antenna element and the q-th TMS antenna element can be expressed as follows

$$\mathbf{D}_{pq}^{LoS}(t) = \mathbf{A}_q^R(t) - \mathbf{A}_p^T. \tag{5.7}$$

Let $a_{n,i}^R(t)$ and $\beta_{n,i}^R(t)$ be the azimuth and elevation angles, respectively, between the i-th ray of Cluster$_n$ and the q-th element of the TMS antenna array, and $a_{n,i}^T(t)$ and $\beta_{n,i}^T(t)$ be the azimuth and elevation angles, respectively, between the i-th ray of Cluster$_n$ and the SBS antenna array. Note that $\beta_{n,i}^R(t) \approx \arctan\left(H_{n,i}^R(t)/R_{n,i}^R(t)\right)$, where $R_{n,i}^R(t)$ is the radial distance of the i-th ray of Cluster$_n$ from the TMS and $H_{n,i}^R(t)$ stands for the height of this ray. The distance vectors of the i-th ray of Cluster$_n$ at the TMS and SBS are calculated, respectively, as

$$\mathbf{D}_{n,i}^R(t) = D_{n,i}^R(t) \begin{bmatrix} \cos a_{n,i}^R(t)\cos\beta_{n,i}^R(t) \\ \sin a_{n,i}^R(t)\cos\beta_{n,i}^R(t) \\ \sin\beta_{n,i}^R(t) \end{bmatrix}^T + \tilde{\mathbf{D}}_{TR}$$

$$= D_{n,i}^R(t) \begin{bmatrix} \cos a_{n,i}^R(t)\cos\left[\arctan\left(H_{n,i}^R(t)/R_{n,i}^R(t)\right)\right] \\ \sin a_{n,i}^R(t)\cos\left[\arctan\left(H_{n,i}^R(t)/R_{n,i}^R(t)\right)\right] \\ \sin\left[\arctan\left(H_{n,i}^R(t)/R_{n,i}^R(t)\right)\right] \end{bmatrix}^T + \tilde{\mathbf{D}}_{TR}, \tag{5.8}$$

$$\mathbf{D}_{n,i}^{T}(t) = D_{n,i}^{T}(t) \begin{bmatrix} \cos\alpha_{n,i}^{T}(t)\cos\beta_{n,i}^{T}(t) \\ \sin\alpha_{n,i}^{T}(t)\cos\beta_{n,i}^{T}(t) \\ \sin\beta_{n,i}^{T}(t) \end{bmatrix}^{T} + \mathbf{H}_{T}, \tag{5.9}$$

where $D_{n,i}^{R}(t)$ and $D_{n,i}^{T}(t)$ are the Frobenius norms of $\mathbf{D}_{n,i}^{R}(t)$ and $\mathbf{D}_{n,i}^{T}(t)$, respectively. Note that as the SBS elevation angle θ_{T} increases, the distance D_{TR} decreases. Without loss of generality, we assume that $\theta_{T} \leq 85°$. For $\theta_{T} = 85°$ (maximum value of the aforementioned inequality) and $H_{T} = 20$ km, we obtain $\tilde{D}_{TR} \approx (H_{T} / \tan\theta) \approx 1750$ m. As long as $R_{n,\max}$ is equal to up a few hundreds of wavelengths, the assumption $R_{n,\max} \ll \tilde{D}_{TR}$ is valid and $\alpha_{n,i}^{T}$ is a small angle. Similarly, we obtain $H_{n,\max} \ll \tilde{D}_{TR}$ and we conclude that $\beta_{n,i}^{T}$ is also a small angle. Then, using the results in [5], (5.9) becomes

$$\mathbf{D}_{n,i}^{T}(t) = D_{n,i}^{T}(t) \begin{bmatrix} 1 \\ R_{n,i}^{R}(t)\sin\alpha_{n,i}^{R}(t)/\tilde{D}_{TR} \\ H_{n,i}^{R}(t)\sin\beta_{n,i}^{R}(t)/\tilde{D}_{TR} \end{bmatrix}^{T} + \mathbf{H}_{T}. \tag{5.10}$$

The distance vectors between the *i*-th ray of Cluster$_n$ and antenna elements are calculated as

$$\mathbf{D}_{q,n,i}^{R}(t) = \mathbf{D}_{n,i}^{R}(t) - \mathbf{A}_{q}^{R}(t), \tag{5.11}$$

$$\mathbf{D}_{p,n,i}^{T}(t) = \mathbf{D}_{n,i}^{T}(t) - \mathbf{A}_{p}^{T}(t). \tag{5.12}$$

In addition, the phase between the *q*-th TMS antenna and the *p*-th SBS antenna via the *i*-th ray at the SBS, and the *n*-th cluster is derived as

$$\varphi_{p,q,n,i}(t) = \varphi_{n,i} + \frac{2\pi}{\lambda}\left[\left\|\mathbf{D}_{p,n,i}^{T}(t)\right\| + \left\|\mathbf{D}_{q,n,i}^{R}(t)\right\|\right], \tag{5.13}$$

where $\|\cdot\|$ denotes the Euclidean norm and $\varphi_{n,i}$ is the initial phase of the signal at the SBS and is drawn from a uniform 0° to 360° degree distribution. Accordingly,

the Doppler frequency of the q-th receive antenna via the i-th ray of the n-th cluster is presented as

$$f_{q,n,i}(t) = \frac{f_{R,\max}\left\langle \mathbf{D}^{R}_{q,n,i}(t), \mathbf{v}_{R}\right\rangle}{\left\|\mathbf{D}^{R}_{q,n,i}(t)\right\|\left\|\mathbf{v}_{R}\right\|}, \tag{5.14}$$

where $f_{R,\max} = v_{R}/\lambda$ is the maximum Doppler frequency associated with TMS, λ is the carrier wavelength, $\langle\cdot,\cdot\rangle$ represents the inner product and $\mathbf{v}_{R}$ is the velocity vector of the TMS antenna array. Similarly, the phase and the Doppler frequency of the LoS component can be calculated, respectively, as

$$\varphi^{LoS}_{p,q}(t) = \varphi_{LoS} + \frac{2\pi}{\lambda}\left\|\mathbf{D}^{LoS}_{pq}(t)\right\|, \tag{5.15}$$

$$f^{LoS}_{q}(t) = \frac{f_{R,\max}\left\langle \mathbf{D}^{LoS}_{pq}(t), \mathbf{v}_{R}\right\rangle}{\left\|\mathbf{D}^{LoS}_{pq}(t)\right\|\left\|\mathbf{v}_{R}\right\|}, \tag{5.16}$$

where φ_{LoS} is the LoS phase, which is drawn from a uniform 0º to 360º degree distribution.

The generation procedure of the channel impulse response consists of the generation of the initial cluster set, generation of parameters for the initial cluster set, array-time evolution of clusters, and the generation of channel impulse response. The algorithm in Fig. 5.3 is a generalized version of the QUAsi Deterministic RadIo channel GenerAtor (QuaDRiGa) channel model [8] (which is also an extension of the WINNER channel model [9]) and includes the array-time evolution of clusters to capture massive MIMO channel characteristics. More specifically, the QuaDRiGa channel model ignores the resolvable rays and varying numbers of rays within clusters and generates the initial delays, powers, and azimuth and elevation AoAs and AoDs for each cluster. To create the non-stationarities across the array, the proposed channel model modifies this procedure, in order obtain one azimuth angle and one elevation angle of departure for each sub-array.
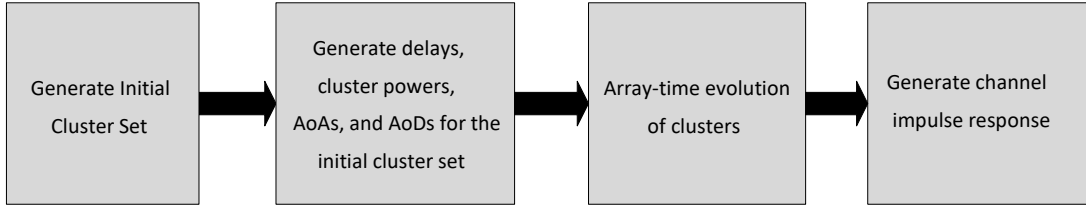
Figure 5.3: Algorithm flowchart of the generation of the channel impulse response.

5.3 Non-Stationary Properties

The non-stationary process of the proposed channel model is based on the array-time evolution of clusters through a birth-death process. To model both the phenomena of cluster appearance/disappearance on antenna arrays and the non-stationary behavior of clusters on the time axis, the cluster sets $\left\{C_q^R(t)\right\}$ and $\left\{C_p^T(t)\right\}$ for each antenna are initially generated based on birth-death process on both the time and array axes [6]. The first procedure determines the cluster set of each antenna. Then, the geometrical relationships are updated with respect to the mobility of the TMS and the clusters. Besides, the second procedure determines all parameters for each cluster.

It is assumed that the initial cluster sets of the 1-st receive and the 1-st transmit antenna are represented, respectively, as $C_1^R(t) = \left\{c_x^R : x = 1,2,...,N\right\}$ and $C_1^T(t) = \left\{c_x^T : x = 1,2,...,N\right\}$ at the initial time instant t, where c_x^R and c_x^T are two representations of the x-th cluster. These clusters in cluster set $C_1^R(t)$ and $C_1^T(t)$ evolve according to birth-death process on the array axis to recursively generate the cluster sets of the rest of antennas at the SBS and the TMS, respectively, at the initial time instant t, which is expressed as

$$C_{q-1}^R(t) \xrightarrow{E} C_q^R(t),$$ (5.17)

$$C_{p-1}^T(t) \xrightarrow{E} C_p^T(t),$$ (5.18)

where the operator $\overset{E}{\rightarrow}$ denotes cluster evolution (on either the array or time axis). It is assumed that the appearance and disappearance of clusters is statistically independent. The probability for the duration between two cluster-births is exponentially distributed [10], i.e.,

$$p_G(\delta) = \lambda_G \exp(-\lambda_G \delta)\sigma(\delta), \tag{5.19}$$

where $E[\delta] = 1/\lambda_G$, λ_G (per meter) is the cluster generation (birth) rate on the array axis, and $\sigma(\cdot)$ is the unity step function. The life duration of each cluster is exponentially distributed as follows [11]

$$p_R(\delta) = \lambda_R \exp(-\lambda_R \delta)\sigma(\delta), \tag{5.20}$$

where $E[\delta] = 1/\lambda_R$ and λ_R (per meter) is the cluster recombination (death) on the array axis. Hence, with the evolutions $C^R_{q-1}(t) \overset{E}{\rightarrow} C^R_q(t)$ and $C^T_{p-1}(t) \overset{E}{\rightarrow} C^T_p(t)$, the survival probabilities of the clusters in the inside the cluster set on array axis at the TMS and the SBS can be, respectively, modeled as exponential functions as follows [11]

$$P^R_{survival} = \int_{\delta_R}^{+\infty} p_R(\delta)d\delta = \exp(-\lambda_G \delta_R), \tag{5.21}$$

$$P^T_{survival} = \int_{\delta_T}^{+\infty} p_R(\delta)d\delta = \exp(-\lambda_G \delta_T). \tag{5.22}$$

Similarly, the birth probabilities of the new cluster at the TMS and SBS can be expressed, respectively, as

$$P^R_{new} = \int_0^{\delta_R} p_G(\delta)d\delta = 1 - \exp(-\lambda_G \delta_R), \tag{5.23}$$

$$P^T_{new} = \int_0^{\delta_T} p_G(\delta)d\delta = 1 - \exp(-\lambda_G \delta_T). \tag{5.24}$$

The cluster sets of the rest of the antenna elements $C_q^R(t)$ ($q = 2,3,...,L_R$) and $C_p^T(t)$ ($p = 2,3,...,L_T$) can be generated from the evolution of $C_1^R(t)$ and $C_1^T(t)$, respectively, based on (5.21)-(5.24). To simulate the randomness of a real propagation environment, the cluster indices $\bigcup_{q=1}^{L_R} C_q^R(t)$ and $\bigcup_{q=1}^{L_R} C_p^T(t)$ are randomly shuffled and paired. Then the cluster indices are reassigned from 1 to N.

To generate the parameters of the initial clusters, i.e., the delays and the normalized power, a typical urban macro-cell scenario is considered [9]. Thus, it is assumed that these parameters follow the exponential distribution. The exponential delay distribution delays can be expressed as

$$\tau_n = -r_\tau \sigma_\tau \ln(X_n), \tag{5.25}$$

where r_τ is the delay distribution proportionality factor, σ_τ is delay spread, and $X_n \sim \text{Uni}(0,1)$. Then, the delays are normalized by subtracting with minimum delay and sorted to descending order. Moreover, the powers of each cluster can be expressed as

$$P_n = \exp\left(-\tau_n \frac{r_\tau - 1}{r_\tau \sigma_\tau}\right) 10^{-\frac{Z_n}{10}}, \tag{5.26}$$

where $Z_n \sim N(0,\xi)$ is the per cluster shadowing term in dB. To ensure that the sum power of all clusters is equal to one, the cluster powers are normalized. The power of each ray within a cluster is equal to P_n / N.

Several different distributions, such as uniform [12], von Mises [13] and Laplacian [14], [15], were used in prior work to characterize the azimuth angle $a_{n,i}^R$. In this work, the von Mises pdf (also known as the circular normal distribution) is used, because it approximates many of the aforementioned distributions, and is empirically justified in urban and suburban areas in [16]. The von Mises pdf is defined as

$$f\left(a_{n,i}^{R}\right) = \frac{e^{k\cos\left(a_{n,i}^{R}-\mu_{n}\right)}}{2\pi I_{0}\left(k_{n}\right)}, \quad -\pi \leq a_{n,i}^{R} \leq \pi, \tag{5.27}$$

where $I_{0}\left(\cdot\right)$ is the zeroth-order modified Bessel function of the first kind, $\mu_{n} \in \left[-\pi,\pi\right]$ is the mean angle at which the scatterers are distributed in the x-y plane, and $k_{n} \geq 0$ controls the spread around the mean.

In order to characterize the distance $R_{n,i}^{R}$, the hyperbolic pdf [17] is used, which is empirically justified in [18], [19]. This distribution is more realistic and flexible than other commonly used distributions, such as the uniform distribution [20], [21], because it allows scatterers to assume higher concentration in a flexible area in the vicinity of the TMS. The hyperbolic pdf is defined as follows [17]-[19]

$$f\left(R_{n,i}^{R}\right) = \frac{a_{n}}{\tanh\left(a_{n}R_{n,i,\max}\right)\cosh^{2}\left(a_{n}R_{n,i}^{R}\right)}, \quad 0 < R_{n,i}^{R} \leq R_{n,\max}. \tag{5.28}$$

The parameter a_{n} controls the spread of the scatterers around the TMS and its applicable value is in the interval $\left(0,1\right)$. As the elevation angle of the aerial platform decreases, the scatterers are expected to be more widely distributed, which corresponds to a possible decrease of a_{n}. Nevertheless, a_{n} can be accurately obtained through measurements in different propagation environments.

The building height was found to follow normal [22], log-normal [22]-[24] or Rayleigh distribution [25], depending on the selected urban or suburban environment. Specifically, the corresponding distributions matched geographical data values obtained from measurements of building heights conducted in high and medium built-up density areas in different European countries. In order to characterize the height $H_{n,i}^{R}$, the log-normal pdf is adopted, which is defined as

$$f\left(H_{n,i}^{R}\right) = \frac{e^{-\frac{\left[\ln\left(H_{n,i}^{R}\right)-\ln\left(H_{n,\mathrm{mean}}\right)\right]^{2}}{2\sigma_{n}^{2}}}}{H_{n,i}^{R}\sigma_{n}\sqrt{2\pi}}, \quad 0 < H_{n,i}^{R} \leq H_{n,\max}, \tag{5.29}$$

where the parameters $H_{n,\text{mean}}$ and σ_n are the mean and standard deviation of $H_{n,i}^{R}$, respectively.

The mobility of the TMS and the clusters give rise to a time-variant channel impulse response. Hence, the geometry relationships of the TMS and the clusters should be updated from t to $t + \Delta t$. At the next time instant $t + \Delta t$, the time-axis evolution of clusters is operated as follows

$$C_q^R(t) \xrightarrow{E} C_q^R(t + \Delta t), \tag{5.30}$$

$$C_p^T(t) \xrightarrow{E} C_p^T(t + \Delta t). \tag{5.31}$$

Similar to the evolution on array axis, the survival probability of each cluster can be calculated as

$$P_{survival}(\Delta t) = \exp\left[-\lambda_R^t \left(\|\mathbf{v}_R\| \Delta t + P_f u_c \Delta t\right)\right], \tag{5.32}$$

where λ_R^t is the recombination rate on time axis, P_f is the percentage of moving clusters, u_c is the speed of n-th cluster, and $\|\mathbf{v}_R\| \Delta t + P_f u_c \Delta t$ is the channel fluctuation. The birth probability of the new cluster at time $t + \Delta t$ can be expressed as

$$P_{new}(\Delta t) = 1 - \exp\left[-\lambda_G^t \left(\|\mathbf{v}_R\| \Delta t + P_f u_c \Delta t\right)\right], \tag{5.33}$$

where λ_G^t is the generation rate on the time axis. After the time evolution process, the clusters can be categorized as survival clusters or newly generated clusters.

Survived clusters: The properties of survived clusters, i.e., delays, Doppler frequencies, and azimuth and elevation AoAs and AoDs, should be recalculated based on the updates of geometrical relationships from t to $t + \Delta t$. More specifically, the distance vectors should be updated due to mobility of the receiver and clusters as follows

$$\mathbf{D}_{n,i}^{R}\left(t+\Delta t\right)=\mathbf{D}_{n,i}^{R}\left(t\right)+\mathbf{v}_{n}\Delta t, \tag{5.34}$$

$$\mathbf{D}_{q,n,i}^{R}\left(t+\Delta t\right)=\mathbf{D}_{n,i}^{R}\left(t\right)-\mathbf{A}_{q}^{R}\left(t\right)+\left(\mathbf{v}_{n}-\mathbf{v}_{R}\right)\Delta t. \tag{5.35}$$

Besides, the time-variant phase and Doppler frequency can be, respectively, expressed as

$$\varphi_{p,q,n,i}\left(t+\Delta t\right)=\varphi_{0}+\frac{2\pi}{\lambda}\Big[\left\|\mathbf{D}_{p,n,i}^{T}\left(t\right)\right\|+\left\|\mathbf{D}_{q,n,i}^{R}\left(t+\Delta t\right)\right\|\Big], \tag{5.36}$$

$$f_{q,n,i}\left(t+\Delta t\right)=\frac{f_{R,\max}\left\langle\mathbf{D}_{q,n,i}^{R}\left(t+\Delta t\right),\mathbf{v}_{R}\right\rangle}{\left\|\mathbf{D}_{q,n,i}^{R}\left(t+\Delta t\right)\right\|\left\|\mathbf{v}_{R}\right\|}. \tag{5.37}$$

Finally, the geometrical relationships of LoS components are also updated as follows:

$$\mathbf{D}_{pq}^{LoS}\left(t+\Delta t\right)=\mathbf{A}_{q}^{R}\left(t\right)+\mathbf{v}_{R}\Delta t-\mathbf{A}_{p}^{T}, \tag{5.38}$$

$$\varphi_{p,q}^{LoS}\left(t+\Delta t\right)=\varphi_{0}+\frac{2\pi}{\lambda}\left\|\mathbf{D}_{pq}^{LoS}\left(t+\Delta t\right)\right\|, \tag{5.39}$$

$$f_{p,q}^{LoS}\left(t+\Delta t\right)=\frac{f_{R,\max}\left\langle\mathbf{D}_{pq}^{LoS}\left(t+\Delta t\right),\mathbf{v}_{R}\right\rangle}{\left\|\mathbf{D}_{pq}^{LoS}\left(t+\Delta t\right)\right\|\left\|\mathbf{v}_{R}\right\|}. \tag{5.40}$$

Newly generated clusters: The azimuth and elevation AoAs and AoDs, the delays, and the distances of newly generated clusters are initialized according to the aforementioned statistical distributions. The power of each cluster is calculated and normalized as in [9]. Denote the set of all survived clusters as C_{survived} and the set of all newly generated clusters as C_{new} after the time-axis evolution. The average total power of survived and newly generated clusters should be normalized as [26]

$$\sum_{\text{Cluster}_{i}\in C_{survived}}P_{i}+\sum_{\text{Cluster}_{j}\in C_{new}}P_{j}=1. \tag{5.41}$$

5.4 Statistical Properties

Considering a 3-D non-isotropic scattering environment, the STCF between the channel gains $h_{qp}(t)$ and $h_{q'p'}(t)$ is defined as [27]

$$R_{qp,q'p',n}(\delta_T,\delta_R,\Delta t,t) = \mathrm{E}\left[\frac{h^*_{qp,n}(t)h^*_{q'p',n}(t+\Delta t)}{\left|h^*_{qp,n}(t)\right|\left|h^*_{q'p',n}(t+\Delta t)\right|}\right]. \tag{5.42}$$

where $(\cdot)^*$ denotes complex conjugate operation. Since the LoS component and NLoS components are independent, (5.42) can be rewritten as the sum of the STCFs of the LoS component and the NLoS components as follows

$$R_{q,p,q'p',n}(\delta_T,\delta_R,\Delta t,t) = R^{LoS}_{q,p,q'p',n}(\delta_T,\delta_R,\Delta t,t) + R^{NLoS}_{q,p,q'p',n}(\delta_T,\delta_R,\Delta t,t), \tag{5.43}$$

where

$$R^{LoS}_{q,p,q'p',n}(\delta_T,\delta_R,\Delta t,t) = \frac{K\delta(n-1)}{(K+1)}\exp(j\Phi_{LoS}), \tag{5.44}$$

$$R^{NLoS}_{q,p,q'p',n}(\delta_T,\delta_R,\Delta t,t) = \frac{1}{K\delta(n-1)+1}E\left[\lim_{I\to\infty}\frac{1}{\sqrt{I}}\sum_{i=1}^{I}\exp(j\Phi_{NLoS})\right], \tag{5.45}$$

$$\Phi_{LoS} = 2\pi f^{LoS}_{q'}(t+\Delta t)(t+\Delta t) - 2\pi f^{LoS}_{q}(t)t + \varphi^{LoS}_{p',q'}(t+\Delta t) - \varphi^{LoS}_{p,q}(t), \tag{5.46}$$

$$\Phi_{NLoS} = 2\pi f^{NLoS}_{q',n,i}(t+\Delta t)(t+\Delta t) - 2\pi f^{NLoS}_{q,n,i}(t)t + \varphi^{NLoS}_{p',q',n,i}(t+\Delta t) - \varphi^{NLoS}_{p,q,n,i}(t). \tag{5.47}$$

By setting $\Delta t = 0$, the STCF reduces to the spatial correlation function (SCF) $R_{q,p,q'p',n}(\delta_T,\delta_R,t)$. Besides, by setting $p=p'$ and $q=q'$, the temporal correlation function (TCF) $R_{q,p,n}(\Delta t,t)$ is obtained. Finally, the time-dependent Doppler PSD with respect to the Doppler frequency f is the Fourier transform of the TCF and can be expressed as follows

$$S_n(f,t) := \int_{-\infty}^{\infty} R_{qp,n}(\Delta t,t)\exp(-j2\pi f\Delta t)d(\Delta t). \tag{5.48}$$

5.5 Numerical Results

This section provides numerical results and investigates the absolute spatial and temporal correlation, as well as the PDF of Doppler frequency. Unless indicated otherwise, the values of the model parameters used to obtain the curves are $L_T = 10$, $L_R = 40$, $t = 1$ sec, $\theta_T = 60°$, $\xi_T = \xi_R = \pi/2$, $\psi_R = 0°$, $H_T = 20$ km, $H_R = 1$ m, $k = 3$, $\mu = 0°$, $R_{1,max} = 200$ m, $H_{1,max} = 60$ m, $\lambda = 0.15$ m, $\|\mathbf{v}_R\| = 4$ m/s, $a_u = \pi/6$, $f_{R,max} = 40$ Hz, and $\gamma_R = \pi/6$. In the simulations, it is assumed that $\lambda_G = 80/\text{m}$ [28, Table I] and $\lambda_R = 4/\text{m}$. Hence, the mean number of clusters is 20 [9]. It is also assumed that $l = 20$, $r_\tau = 2.3$ [11], $\sigma_\tau = 0.32$ [11], $\xi = 3$ dB [11], and $P_f = 0.3$ [28]. Moreover, a typical densely built-up district (London, U.K. [157]) is considered to be the scattering region, i.e., the surrounding buildings act as scatterers, and the values of the corresponding model parameters used are $H_{1,max} = 100$ m, $H_{1,mean} = 17.6$ m, and $\sigma = 0.31$. In addition, it is assumed that $a = 0.01$, which corresponds to a reasonable average distance between the TMS and an effective scatterer of approximately 60 m. This value was observed by applying ray-tracing techniques to 3-D digital maps of European typical urban environments. Specifically, the AWE Communications Winprop software package was used, which is designed to accurately predict the propagation characteristics between the link of a transmitter and a receiver including all important parameters of the mobile radio channel. Finally, in order to clearly present the influence of each model parameter on the correlation, and indicate the minimum achieved correlation, it is considered that the Rician factor of all links is equal to 0 (Rayleigh channel). However, in many cases a LoS component exists.

Fig. 5.4 demonstrates the absolute values of the SCF $R_{q,p,q'p',n}(\delta_T, \delta_R, t)$. One observes that the correlation decreases, as the normalized antenna spacings increase at both the SBS and TMS sides. Moreover, fluctuations are also observed as the antenna spacing at receiver side increases due to the non-stationary properties and the mobility of the receiver.
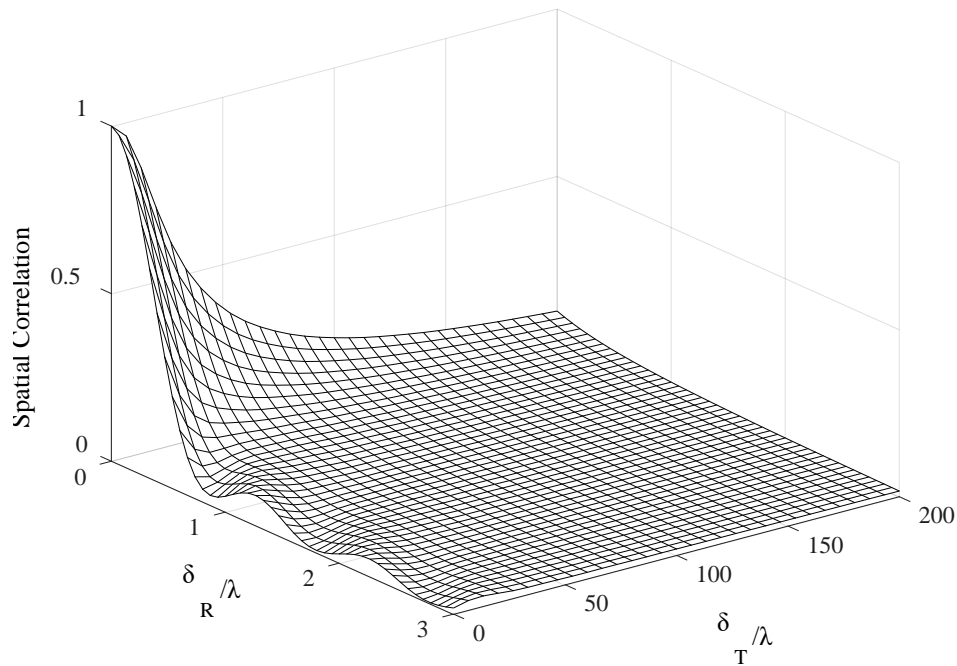
**Fig. 5.4:** Absolute values of the SCF of the 3-D model.

Fig. 5.5 demonstrates an example of cluster evolution on the array axis. Although there exist initially 20 observable clusters to the first antenna element, these clusters evolve according to the birth-death process and probabilities described in Section 5.3. Hence, 5 clusters disappear during the evolution process and 5 new clusters have been generated. More specifically, different TMS antenna elements may observe different cluster sets. For instance, the cluster sets of the 3rd and the 15th TMS antenna elements share 18 common clusters.

Finally, Fig. 5.6 depicts the normalized time-dependent Doppler PSD of the proposed model for massive MIMO channels and the corresponding Doppler PSD of the conventional model for MIMO channels in [5]. One observes that the Doppler PSD of the conventional model is symmetrical with respect to 0. Nevertheless, this is not observed for the proposed non-stationary massive MIMO channel model. In particular, the Doppler PSD at different time instants varies due to the non-stationary properties on the time axis.
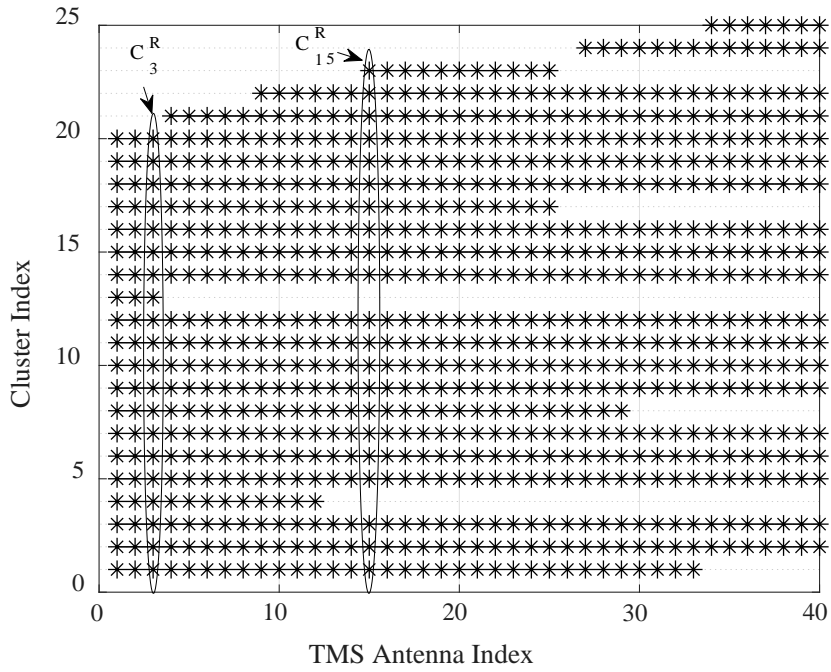
Figure 5.5: A representative example of the cluster evolution on the TMS antenna array, where the symbol "∗" designates the observable cluster.
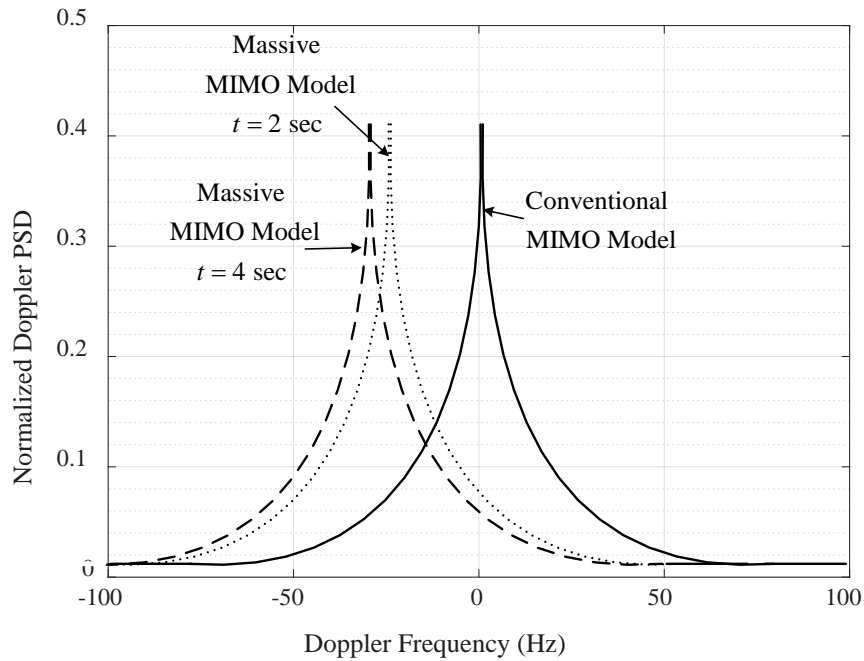
Figure 5.6: The normalized Doppler PSD at different time instants.

REFERENCES

[1] S. Payami and F. Tufvesson, "Channel measurements and analysis for very large array systems at 2.6 GHz," in *Proc. 6th Eur. Conf. Antennas Propag.*, Prague, Czech Republic, Mar. 2012, pp. 433-437.

[2] X. Gao, F. Tufvesson, O. Edfors, and F. Rusek, "Measured propagation characteristics for very-large MIMO at 2.6 GHz," in *Proc. 46th Annu. Asilomar Conf. Signals*, Syst., Comput., Pacific Grove, CA, USA, Nov. 2012, pp. 295-299.

[3] F. Bohagen, P. Orten, and G. E. Oien, "Design of capacity-optimal highrank line-of-sight MIMO channels," Univ. of Oslo, Research Rep. 352, Mar. 2007.

[4] A. Kuchar, J. -P. Rossi, and E. Bonek, "Directional macro-cell channel characterization from urban measurements," *IEEE Trans. Antennas Propag.*, vol. 48, no. 2, pp. 137–146, Feb. 2000.

[5] E. T. Michailidis and A. G. Kanatas, "Three-Dimensional HAP-MIMO Channels: Modeling and Analysis of Space-Time Correlation," *IEEE Transactions on Vehicular Technology*, vol. 59, no. 5, pp. 2232-2242, Jun. 2010.

[6] S. Wu, C. Wang, H. Haas, e. M. Aggoune, M. M. Alwakeel and B. Ai, "A Non-Stationary Wideband Channel Model for Massive MIMO Communication Systems," *IEEE Transactions on Wireless Communications*, vol. 14, no. 3, pp. 1434-1446, Mar. 2015.

[7] A. Aragón-Zavala, J. L. Cuevas-Ruíz, and J. A. Delgado-Penín, *High-Altitude Platforms for Wireless Communications*, New York, USA: John Wiley & Sons, Dec. 2008.

[8] S. Jaeckel, L. Raschkowski, K. Borner, and L. Thiele, "QuaDRiGa: A 3-D multi-cell channel model with time evolution for enabling virtual field trials," IEEE Trans. Antennas Propag., vol. 62, no. 6, pp. 3242–3256, Jun. 2014.

[9] WINNER D1.1.2 P. Kyosti, et al., "WINNER II channel models", ver 1.1, Sept. 2007. Available: https://www.ist-winner.org/WINNER2-Deliverables/D1.1.2v1.1.pdf

[10] T. Zwick, C. Fischer, and W. Wiesbeck, "A stochastic multipath channel model including path directions for indoor environments," *IEEE J. Sel. Areas Commun.*, vol. 20, no. 6, pp. 1178C1192, Aug. 2002.

[11] H. Wu, S. Jin and X. Gao, "Non-stationary multi-ring channel model for massive MIMO systems," *2015 International Conference on Wireless Communications & Signal Processing (WCSP)*, Nanjing, 2015, pp. 1-6.

[12] J. Salz and J. H. Winters, "Effect of fading correlation on adaptive arrays in digital mobile radio," *IEEE Transactions on Vehicular Technology*, vol. 43, no. 4, pp. 1049-1057, Nov. 1994.

[13] A. Abdi and M. Kaveh, "A space-time correlation model for multielement antenna systems in mobile fading channels," *IEEE Journal on Selected Areas in Communications*, vol. 20, no. 3, pp. 550-560, Apr. 2002.

[14] P. R. King, B. G. Evans, and S. Stavrou, "Physical-statistical model for the land mobile-satellite channel applied to satellite/HAP MIMO," in *Proc. 11th European Wireless Conference 2005*, vol. 1, pp. 198-204, Nicosia, Cyprus, Apr. 2005.

[15] K. I. Pedersen, P. E. Mogensen, and B. H. Fleury, "Power azimuth spectrum in outdoor environments," *Electronics Letters*, vol. 33, no. 18, pp. 1583-1584, Aug. 1997.

[16] A. Abdi, J. A. Barger, and M. Kaveh, "A parametric model for the distribution of the angle of arrival and the associated correlation function and power spectrum at the mobile station," *IEEE Transactions on Vehicular Technology*, vol. 51, no. 3, pp. 425-434, 2002.

[17] S. S. Mahmoud, Z. M. Hussain, and P. O'Shea, "Space-time model for mobile radio channel with hyperbolically distributed scatterers," *IEEE Antennas and Wireless Propagation Letters*, vol. 1, pp. 211-214.

[18] S. S. Mahmoud, Z. M. Hussain, and P. O'Shea, P., "A geometrical-based microcell mobile radio channel model," *Wireless Networks*, vol. 12, no. 5, pp. 653-664, Sep. 2006.

[19] [S. S. Mahmoud, F. S. Al-Qahtani, Z. M. Hussain, and A. Gopalakrishnan, "Spatial and temporal statistics for the geometrical-based hyperbolic macrocell channel model," *Digital Signal Processing*, vol. 18, no. 2, pp. 151-167, Mar. 2008.

[20] F. Dovis, R. Fantini, M. Mondin, and P. Savi, "Small-scale fading for high-altitude platform (HAP) propagation channels," *IEEE Journal on Selected Areas in Communications*, vol. 20, no. 3, pp. 641-647, Apr. 2002.

[21] T. S. Rappaport, and J. C. Liberti, "A geometrical-based model for line-of sight multipath radio channel," in *Proc. IEEE 46th Vehicular Technology Conference (VTC) 1996*, Atlanta, GA, USA, 844-848, April/May 1996.

[22] M.A. Vázquez-Castro, F. Perez-Fontan and S. R. Saunders, "Shadowing correlation assessment and modeling for satellite diversity in urban environments," *International Journal of Satellite Communications*, vol. 20, no. 2, March/April 2002, pp. 151-166.

[23] M. A. Vázquez-Castro, D. Belay-Zeleke, A. Curieses-Guerrero, "Availability of systems based on satellites with spatial diversity and HAPS," *Electronics Letters*, vol. 38, no. 6, pp. 286-288, Mar. 2002.

[24] C. Tzaras, B.G. Evans and S.R. *Saunders, "Physical-statistical analysis of land mobile-satellite channel," Electronics* Letters, vol. 34, no. 13, pp. 1355-1357, Jun. 1998.

[25] S. R. Saunders and B. G. Evans, "Physical model of shadowing probability for land mobile satellite propagation," *Electronics Letters*, vol. 32, no. 17, pp. 1548-1549, Aug. 1996.

[26] S. Wu, C. Wang, e. M. Aggoune, M. M. Alwakeel and Y. He, "A Non-Stationary 3-D Wideband Twin-Cluster Model for 5G Massive MIMO Channels," *IEEE Journal on Selected Areas in Communications*, vol. 32, no. 6, pp. 1207-1218, June 2014.

[27] M. Patzold, *Mobile Radio Channels*., 2nd ed., John Wiley & Sons, West Sussex, 2012.

[28] T. Zwick, C. Fischer, D. Didascalou, and W. Wiesbeck, "A stochastic spatial channel model based on wave-propagation modeling," *IEEE J. Sel. Areas Commun*., vol. 18, no. 1, pp. 6–15, Jan. 2000.

6

Conclusions

With their unique characteristics, the NTNs seem to represent an efficacious alternative infrastructure, which can revolutionize the telecommunication industry and make the 5G vision a reality. It is envisaged that the next-generation aerospace systems will be potentially capable of providing and delivering a compelling range of current and next generation mobile/fixed services. The aim of this research was to quantify the benefit of applying advanced wireless communication technologies to aerospace systems. At the beginning of this research, a literature survey suggested that limited theoretical work or measurement data were in existence that cope with this objective. Motivated by these facts, this section concludes this research.

In Chapter 2, an overview on the role of aerospace communication technologies in the future IoT ecosystem has been provided. Since ubiquitous connectivity and long-range radio coverage are required in many critical IoT applications, spaceborne and airborne systems along with advanced wireless technologies can significantly enhance the QoS and the Quality of Experience (QoE) and strongly support the evolution of IoT and IIoT. Due to the rapid advances in technology and industrial infrastructure, IoT is expected to be widely applied to industries and facilitate the automated monitoring, control, management, and maintenance. Overall, the IoT market constitutes a significant opportunity for aerospace service providers. Notwithstanding, there exist many challenges and performance barriers towards a successful IoT deployment, such as standardization, energy-efficiency, security, and privacy. Future efforts are needed to address these challenges and examine the particular characteristics of different industrial sectors.

In Chapter 3, the benefits of using multiple antenna techniques in MU relay-based satellite systems have been demonstrated. The results have shown the gain

in the BER and the achievable channel capacity by applying ZF and MMSE signal detection schemes in different propagation conditions. Nevertheless, it is important to verify this results in real-world propagation conditions. Moreover, other relaying techniques, such as DF relaying, and more sophisticated signal detection techniques, such as the non-linear ML and Tomlinson-Harashima Precoding (THP) techniques, may be exploited, in order to involve additional signal processing and improve error rate performance. In this chapter, an opportunistic MS-MD pair selection scheme for rate-adaptive MU MIMO-OSTBC aerial platform aided systems over i.n.i.d. Nakagami-m fading channels has been also presented, where the users and the relay are equipped with multiple antennas. Since the improper position of the relay substantially affects the system performance, optimal geometry-based design criteria for the placement of the relay have been developed, while the impact of the number of antennas and SD pairs, the severity of fading, and the proper/improper relay location on the system performance and design has been studied. Since the power control is important in MS-MD relay networks, the joint optimization of the power allocation and the relay location has been also realized. The results have indicated the influence of the number of SD pairs and antennas on the outage performance. These results have also pointed out that the outage performance degrades, as the relay shifts from its optimized location and especially from its optimal elevation angle. Overall, the design recommendations provide a convenient framework for the solution of the fundamental problem of the placement of aerial relay platforms, in order to guarantee the successful operation and feasibility of the proposed system in practice.

In Chapter 4, the performance of a triple-hop mixed RF/FSO/RF stratospheric communication system has been investigated. The results have depicted that the Rician factor significantly influences the system performance. These results have also underlined that the performance degrades, as the inter-HAP distance increases. However, for the worst turbulence case, this distance slightly affects the outage probability. The results have also shown that the misalignment-induced

fading has a severe effect on the system performance. Since there are no experimental data available in the literature to fully verify the theoretical results, future research efforts may be devoted to collecting measured channel data in real-world propagation conditions.

Finally, in Chapter 5, the application of the massive MIMO technology to stratospheric systems has been studied. Since the major characteristics of massive MIMO channels have not been captured by conventional MIMO channel models in the literature, a novel theoretical 3-D multi-cylinder RSGBSM model for non-stationary wideband massive MIMO stratospheric channels has been proposed. Spherical wavefronts have been assumed to characterize nearfield effects resulting in azimuth and elevation AoA and AoD shifts, received power variations, and Doppler frequency variations on the antenna array. Specifically, the non-stationary properties on both the time and array axes have been modeled by birth-death processes. The proposed channel model is able to describe not only the appearance and disappearance of clusters on the time axis, but also the cluster evolution on the array axis, which is not studied in conventional MIMO systems.

Due to the lack of channel-sounding measurement campaigns, it is important to verify the theoretical results of this post-doctoral research in real-world propagation conditions. Specifically, the satellites and the aerial platforms/vehicles could be emulated by using a helicopter, a small plane or a balloon containing multiple antennas sufficiently separated. However, access to real satellites or HAPs/MAPs/LAPs would be even more ideal.

Appendix

1. Derivation of Equations (3.30) and (3.34)

Applying the sine law to the triangle $S_1 S_k D_1$ in Fig. 3.8, it follows that

$$\frac{d_{S_1 S_k}}{\sin\left(\pi - \omega_{S_k D_1}\right)} = \frac{d_{S_k D_1}}{\sin \omega_{S_1 S_k}} = \frac{d_{S_1 D_1}}{\sin\left[\pi - \omega_{S_1 S_k} - \left(\pi - \omega_{S_k D_1}\right)\right]}. \tag{A.1}$$

Since the sources are far enough from the destinations, the inequality $\max\left\{d_{S_1 S_k}\right\} \ll d_{S_1 D_1}$ holds. Then, we can conclude that $\pi - \omega_{S_k D_1} = \arcsin\left(d_{S_1 S_k} / d_{S_1 D_1}\right) \approx d_{S_1 S_k} / d_{S_1 D_1}$ is a small angle, and $\omega_{S_k D_1} \approx \pi$. Thus, (A.1) becomes

$$\frac{d_{S_1 S_k}}{\sin\left(\pi - \omega_{S_k D_1}\right)} \approx \frac{d_{S_k D_1}}{\sin \omega_{S_1 S_k}} \approx \frac{d_{S_1 D_1}}{\sin\left(\pi - \omega_{S_1 S_k}\right)}. \tag{A.2}$$

From (A.2), we obtain $d_{S_k D_1} \approx d_{S_1 D_1}$. Hence, the triangle $S_1 S_k D_1$ can be approximated as an isosceles triangle. Since $\left(\omega_{S_k D_1} - \pi\right)$ is a small angle, we obtain

$$\omega_{S_1 S_k} \approx \frac{\pi}{2}, \ 2 \leq k \leq K \tag{A.3}$$

Using (A.3), we finally obtain (3.30). Similarly, applying the sine law to the triangle $S_1 D_1 D_k$ in Fig. 3.8, yields

$$\frac{d_{D_1 D_k}}{\sin \omega_{S_1 D_k}} = \frac{d_{S_1 D_k}}{\sin\left(\pi - \omega_{D_1 D_k}\right)} = \frac{d_{S_1 D_1}}{\sin\left[\pi - \omega_{S_1 D_k} - \left(\pi - \omega_{D_1 D_k}\right)\right]}. \tag{A.4}$$

Then, using the inequality $\max\left\{d_{D_1 D_k}\right\} \ll d_{S_1 D_1}$, we can conclude that $\omega_{S_1 D_k} = \arcsin\left(d_{D_1 D_k} / d_{S_1 D_1}\right) \approx d_{D_1 D_k} / d_{S_1 D_1}$ and $\omega_{S_1 D_k}$ is a small angle.

$$\frac{d_{D_1 D_k}}{\omega_{S_1 D_k}} \approx \frac{d_{S_1 D_k}}{\sin \omega_{D_1 D_k}} \approx \frac{d_{S_1 D_1}}{\sin \omega_{D_1 D_k}}. \tag{A.5}$$

From (A.5), we obtain

$$d_{S_1 D_k} \approx d_{S_1 D_1}. \tag{A.6}$$

Hence, the triangle $S_1 D_1 D_k$ can be approximated as an isosceles triangle. Since $\omega_{S_1 D_k}$ is a small angle, we also obtain

$$\omega_{D_1 D_k} \approx \pi / 2. \tag{A.7}$$

Using (A.5), (A.7), and the approximate relationships $\sin x \approx x$ and $\cos x \approx 1$ for small x, we finally obtain (3.34).

2. Range of Optimal Azimuth and Elevation Angles of the Relay

Due to the monotonicity property of the continuous and increasing cost function P_{out} with respect to $d_{S_k R}$ and $d_{R D_k}$, which are functions of $\omega_{S_1 R}$ and $\beta_{S_1 R}$, decreasing $d_{S_k R}$ and $d_{R D_k}$ yields a smaller cost value. The first derivative of $d_{S_k R}$ and $d_{R D_k}$ with respect to $\omega_{S_1 R}$ are obtained, respectively, as

$$\frac{\partial d_{S_k R}}{\partial \omega_{S_1 R}} = -\frac{2 d_{S_1 S_k} H_R \cos \omega_{S_1 R}}{\tan \beta_{S_1 R}}, \tag{A.8}$$

$$\frac{\partial d_{R D_k}}{\partial \omega_{S_1 R}} = \frac{2 H_R \left(d_{S_1 D_k} \sin \omega_{S_1 R} - d_{D_1 D_k} \cos \omega_{S_1 R} \right)}{\tan \beta_{S_1 R}}. \tag{A.9}$$

From (A.8) and (A.9), we observe that $d_{S_k R}$ is minimized when $\omega_{S_1 R}$ is equal to $\pi / 2$ or $3\pi / 2$, whereas $d_{R D_k}$ is minimized when $\omega_{S_1 R} = \arctan\left(d_{D_1 D_k} / d_{S_1 D_k} \right)$. As previously shown, $d_{D_1 D_k} / d_{S_1 D_k} \approx \omega_{S_1 D_k}$, and $\omega_{S_1 D_k}$ is a small angle closed to $0°$. Hence,

d_{RD_k} is minimized when ω_{S_1R} tends to $0°$. Moreover, the first derivative of d_{S_kR} and d_{RD_k} with respect to β_{S_1R} are obtained, respectively, as

$$\frac{\partial d_{S_kR}}{\partial \beta_{S_1R}} = 2H_R \frac{d_{S_1S_k} \sin\omega_{S_1R} - \dfrac{H_R}{\tan\beta_{S_1R}}}{\sin^2\beta_{S_1R}}, \tag{A.10}$$

$$\frac{\partial d_{RD_k}}{\partial \beta_{S_1R}} = 2H_R \frac{d_{S_1D_k} \cos\omega_{S_1R} + d_{D_1D_k} \sin\omega_{S_1R} - \dfrac{H_R}{\tan\beta_{S_1R}}}{\sin^2\beta_{S_1R}}. \tag{A.11}$$

From (A.10) and (A.11), we observe that d_{S_kR} and d_{RD_k} are minimized when $\beta_{S_1R} = \arctan\left[H_R / \left(d_{S_1S_k} \sin\omega_{S_1R} \right) \right]$ and $\beta_{S_1R} = \arctan\left[H_R / \left(d_{S_1D_k} \cos\omega_{S_1R} + d_{D_1D_k} \sin\omega_{S_1R} \right) \right]$, respectively. Overall, using (A.6), one concludes that the optimal location of the relay is in a propagation area segment, where the following inequalities hold:

$$0 < \omega_{S_1R,opt} < \pi / 2, \tag{A.12}$$

$$\arctan\left(H_R / \max\left\{ d_{S_1D_k} \right\} \right) < \beta_{S_1R,opt} < \pi / 2. \tag{A.13}$$